The Design, Simulation, and Pattern Synthesis of Novel Reflectarrays

Author: Xiaomin Meng
Supervisor: Maziar Nekovee

A thesis presented for the degree of
Doctor of Philosophy

UNIVERSITY
OF SUSSEX

School of Engineering and Informatics
University of Sussex
UK
01/06/2022

Statement

I, Xiaomin Meng, hereby declare that this thesis has not been and will not be submitted in whole or in part to another university for the award of any other degree.

In this thesis, some sections have results and contents directly excerpted from my own publications[52, 50, 51, 78].

Xiaomin Meng

01/06/2022

Acknowledgement

Firstly, I want to thank my supervisor, Professor Maziar Nekovee, for his continual support throughout my PhD. Under Professor Nekovee's guidance, I was able to navigate to a fascinating field of research and publish my very first papers.

I want to then express my deepest gratitude to my family members: to my father, mother and brother, and my uncles and aunt in Italy, who have always been there for me, regardless of the situation. I am honoured to be able to share my journey with them and have them along the way. Without their support, this journey would not have been possible.

I would also like to thank my collaborator, and friend, Richard Rudd, for the time spent together. I can always learn a great deal just from being with Richard, the wizard of radio communications with incredible adventure stories.

Last but not least, I am grateful to the examination committee for their valuable time and feedbacks on my thesis.

Abstract

The main focus of this thesis is on the development of both a comprehensive understanding and a thorough computational routine of the reflectarray metasurfaces designs, with focuses on a liquid crystal-based reconfigurable reflectarray metasurface and on the phase-retrieval/optimisation techniques for reflectarray-based pattern synthesis. A dielectric-based polarisation converting reflectarray metasurface is also presented, with the advantage of having a thinner profile over the traditional quartz-based half-wave plates.

In the introductory sections, a thorough review of the state-of-the-art metasurfaces is presented, with a focus on applications to high-frequency wireless communications, as the motivation of this PhD is on the development of technologies that would facilitate the wireless communication challenges for the 5G-and-beyond frequency spectrum. In this section, a review of array antennas, including phased arrays, reflectarrays, transmitarrays, as well as metasurfaces utilising Mie-resonance, plasmonic resonance, geometric phase (Pancharatnam-Berry phase) and photoconductive material is presented. The following chapter on the theoretical background ensures the understanding of the fundamental mechanisms that will be applied to the study of reflectarray metasurfaces and optimisation routines.

The high-frequency propagation associated with beyond-5G wireless communications brings many challenges to the current standards: some of the biggest problems are the much greater path loss and heavy non-line-of-sight signal attenuation. Traditionally, this has been dealt with in phased arrays. However, in the introduction part of this thesis, I show that this becomes impractical due to the requirements of enormous array sizes and expensive high-frequency phase shifters. Therefore, in our research, we have focused on reconfigurable reflectarrays as an intermediate solution to alleviate the tough propagation challenges faced by beyond-5G wireless communications. The reconfigurable reflectarray can either be designed to reflect off from a nearby mobile cell site to enhance the signal strength for non-line-of-sight areas, or it can include an integrated source to function independently, reducing the losses associated with power amplifiers and complex circuitries associated with the enormous array sizes.

This thesis aims to produce a high-frequency tailored reconfigurable reflectarray design, which combines the conceptual advantages from state-of-the-art lumped-element-based and liquid crystal-based reflectarrays. As shown in the literature review section, most recent researches on lumped-element-based reconfigurable reflectarrays are designed for the sub 40 GHz frequencies; with higher frequencies, the intrinsic losses associated with lumped-elements such as PIN diodes make them unsuitable choices. On the other hand, liquid crystals have been used as a tunable material for different radio-frequency applications; however, most state-of-the-art designs of liquid crystal-based reflectarrays do not incorporate individual biasing control for maximum beam-control.

There are also challenges faced with individually-biased reconfigurable reflectarrays. Traditionally, phased arrays can perform single beam-scanning or multiple beam-scanning with the control of multiple sub-arrays. We intend to achieve more complex beam-functionalities (such as vortex, null, and magnitude-specific beams) within the domain of manipulating one individual array. This is already possible with optimisation algorithms such as the genetic algorithm. However, traditional optimisers such as the genetic algorithm and particle swarm optimisation are far too slow to be implemented in an "online" mode, where the algorithm runs onboard the reflectarray to give low-latency solutions. The "online" optimisation mode would be very beneficial as it would reduce the channel occupation from the transmission of configuration information and thus increase channel capacity.

In this thesis, I aim to develop an individually biased liquid crystal-based reconfigurable reflectarray for >100 GHz frequencies. I also aim to develop an algorithm that is sufficiently quick to have the potential to be practically utilised as an onboard pattern synthesis optimisation method. Additionally, using the same design principles, I have designed an all-dielectric-based reflectarray metasurface that acts as a polarisation-converting quarter-wave plate, which is much thinner than traditional quartz-based quarter-wave plates.

In the Research Results and Publications chapter, a complete procedure for the design of LC-based reconfigurable and dielectric-based non-reconfigurable reflectarray metasurfaces is presented, where much of the content comes from the author's own publications[52, 78, 50, 51]. This thesis provides details on the computational tools/programs used, cross-platform routines development with CST Studio Suite, MATLAB and VBA, and the pattern synthesis algorithm, whereby a genetic algorithm is employed for the global optimisation, and an improved Gerchberg-Saxton algorithm is developed and adapted to the application of faster local optimisation for the pattern synthesis. For the all-dielectric reflectarray metasurface, the further functionality of polarisation conversion (linear to circular and circular to linear) is demonstrated on top of the beam-manipulation capabilities of the reflectarrays. The reflectarray metasurfaces can be designed to beamform, beamsteer, beamsplit/multibeam, as well as achieve novel beam profiles such as the vortex profile.

Originally, the idea was to completely focus on the liquid crystal-based study and to develop a down-scaled 28 GHz proof-of-concept, for which partial work had already begun (the simulation, optimisation and initial planning on the construction with collaborators from other departments); however, due to the pandemic and numerous other uncontrollable factors, this was later discarded and replaced by remaining on and extending upon the computational studies, to further understand and improve the pattern synthesis algorithms and the other types of phase-change metasurfaces.

List of Publications

0.1 First Author

1. Xiaomin Meng, Maziar Nekovee, Dehao Wu, Richard Rudd, "*Electronically Reconfigurable Binary Phase Liquid Crystal Reflectarray Metasurface at 108 GHz*", 2019 IEEE Globecom Workshops (GC Wkshps), 2019

2. Xiaomin Meng, Maziar Nekovee, Dehao Wu, "*Reconfigurable liquid crystal reflectarray metasurface for THz communications*", Proceedings of the IET Antenna and Propagation Conference, 2020

3. Xiaomin Meng, Maziar Nekovee and Dehao Wu, "*The Design and Analysis of Electronically Reconfigurable Liquid Crystal-Based Reflectarray Metasurface for 6G Beamforming, Beamsteering, and Beamsplitting*", IEEE ACCESS, 2021

4. Xiaomin Meng, Rupert Young, Maziar Nekovee, "*Modified Gerchberg-Saxton iterative algorithm for reflectarray metasurface multibeam pattern synthesis*". VTC2022-Spring, Helsinki, Finland. IEEE Enabling Technologies for Terahertz Communications (ETTCOM). 2022

0.2 Second Author

1. Richard Rudd, Xiaomin Meng, Victor Ocheri, Dehao Wu, M. Nekovee, "*Joint statistics of urban clutter loss and building entry loss at 3.5 GHz and 27 GHz - from measurement to modelling*", 2020 14th European Conference on Antennas and Propagation (EuCAP), 2020

2. Richard Rudd, Xiaomin Meng, "*Short range statistical basic transmission loss modelling*", UK contribution to ITU-R Working Party 3K, ITU-R Document 3K/249, 23 May 2022, Geneva

List of Figures

List of Tables

Abbreviations

AC - Alternating current
AI - Artificial intelligence
DC - Direct current
EM - Electromagnetic/electromagnetism
FSS - Frequency-selective-surface
FZP - Fresnel zone plate
GA - Genetic algorithm
GHz - Gigahertz
GS - Gerchberg-Saxton
HPBW - Half-power beamwidth
IoT - Internet of things
KPI - Key performance indicator
LC - Liquid Crystal
LOS - Line-of-sight
ML - Machine learning
MoM - Method of Moments
NLOS - Non-line-of-sight
PoC - Proof-of-concept
PSO - Particle swarm optimisation
RIS - Reconfigurable intelligent surfaces
SLL - Sidelobe level
TD - Target deviation
THz - Terahertz

Contents

Part I

Introduction

The higher generation wireless communications (such as 5G and 6G) involve the propagation of high-frequency electromagnetic (EM) waves. Two big challenges with higher frequency wireless communications are the high path-loss and non-line-of-sight (NLOS) issues: higher path-loss means that the EM waves attenuate faster, and thus, further beamforming is needed to enhance the signal propagation, whereas the NLOS means that more relays may be needed in order to establish stable connections. Traditionally, phased arrays have been employed to help tackles these challenges; with higher frequency communications, they may no longer be a sufficient solution due to the exponentially higher demand for phased array element (thus exponentially higher power needs and hence energy-efficiency issues), as well as challenges faced with high-frequency phase shifters. In fact, if we were to adopt a traditional phased array, we would roughly need to increase from 1024 elements at 28 GHz to 100,000 elements at 300 GHz to maintain a stable link of around 20 Gbps over 200 meters. This exponential increase in phased array elements proves to be a challenge both technologically and practically because, firstly, the power amplifier requirement for 100,000 element array will be extremely high; secondly, phase delay components at THz are extremely difficult and expensive to achieve; and last but not least, the losses associated with feeding 100,000 elements will make the device extremely inefficient.

Rather than directly tackling the challenges faced by phased array technologies alone, another perhaps more efficient approach would be to adopt some kind of an intermediate solution, one that alleviates the heightened pressures while the phased array technologies improve. Metasurfaces, such as transmitarrays, reflectarrays, as well as other novel concepts, may be well suited to enhance the propagation channel either by acting as relays or even as practical sub-micro-cells. These aforementioned technologies incorporate the working principles of phased arrays; however, they can be more energy-efficient, as most metasurfaces applied to wireless communication are semi-passive, meaning that they do not generate EM radiation on their own, but require an external source to feed upon. This means that the problem of high-frequency wireless communication can be split into separate problems of source and transceiver, making each easier to optimise. Recent studies[86, 71, 59, 81, 68] have already stepped into the signal propagation and channel estimation domains, and have shown that the inclusion of RISs can assist the data transmission to cell-edge users and create more power-efficient propagation architectures.

While transmitarrays benefit from feed source designs, they can be less efficient and more complex in design and manufacturing. Reflectarrays will be the focus of this PhD, as well as a study on an all-dielectric-based metasurface for polarisation conversion and beamforming. A reflectarray is essentially a semi-passive phased array: rather than requiring power to generate EM radiation from individual antenna elements, the reflectarray antenna elements are semi-passive, only radiating energy upon receiving an external impinging EM wave. Our main research has been focused on the reconfigurable liquid crystal-based (LC) binary reflectarray metasurface, which can be employed as an intermediate relay-like solution to help alleviate the challenges faced with 5G/6G phased arrays. Therefore, in this thesis, I have detailed the entire process involving the design, methodology, and results of the modelled device.

A major element in the production of the farfield results for the reflectarray metasurfaces is the process of surface phase profile retrieval. In order to realise a certain farfield profile, such as a multi-beam profile, we need to know the phase distribution on the surface of the reflectarray metasurface (e.g. what is the combination of the ONs and OFFs of each antenna element). This complex inverse problem is tackled in two ways by our studies: firstly, we have used global optimisers, such as the genetic algorithm (GA), in able to retrieve the most optimised solution; secondly, we have developed a modified Gerchberg-Saxton (GS) iterative algorithm that is suitable for performing antenna pattern synthesis. In my thesis, I have detailed the constructions of both algorithms for the application of array pattern synthesis.

Last but not least, I have also presented results on the non-reconfigurable dielectric-based polarisation-converting reflectarray metasurface. The dielectric resonator-based reflectarray metasurface has the capability of converting between circular and linear polarisations, while beamforming towards the designed reflection location. This is analogous to what a quarter-wave plate does; however, the all-dielectric-based reflectarray is much thinner than the traditional quartz-based based quarter-wave plates.

In the literature review chapter, an overview of the current landscape in EM-control metasurfaces is presented, with a specific focus on wireless telecommunication. Since for 5G and beyond wireless telecommunications, the EM wave used is in the sub-THz (and above) frequencies, this review will focus on the aforementioned technologies in the millimetre-wave regime.

Chapter 1

Research Context and Novelty

1.1 Wireless Communication Background

Since the driving motivation for this PhD originated from the challenges faced in high-frequency wireless communication, it is thus necessary to establish a contextual background.

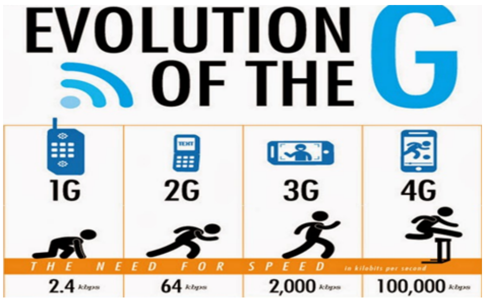

Figure 1.1: Evolution from 1G to 4G[73]

In fig. 1.1, a graphical illustration of the evolution of the mobile communication standards (from the first generation to the fourth) is depicted with details on the bandwidth progression. The first generation of mobile wireless communication was deployed in the 1980s and is now labelled as 1G for abbreviation; it had a bandwidth of 2.4 Kbps, allowing only for voice calls. As the second generation of wireless communication came out, text messaging was enabled in addition to voice calls, with a more than 30 times bandwidth of 64 Kbps. Then came the third-generation (3G), allowing basic web browsing and picture texts, with tripled bandwidth of 2000 kbps. 4G achieved five times the bandwidth of 100,000 Kbps, bringing us the previously unthinkable video calls to wide usage. The incredible jump from voice to video call on a wireless mobile communication device was achieved in the span of 20 years, and now we are already moving into the deployment of 5G, while exploring 6G ideas.

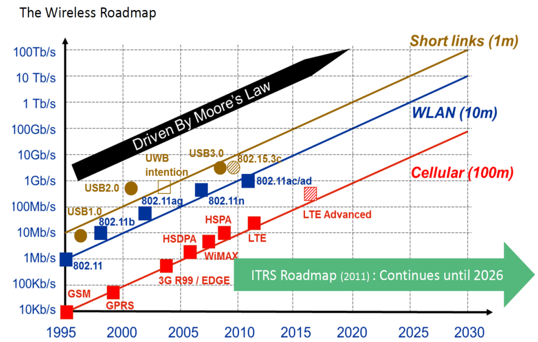

Figure 1.2: Wireless roadmap[38].

In fig. 1.2, a roadmap for the wireless communications development timeline is shown: here, different link types (cellular, WLAN, and short links) and their corresponding data transmission rate for a given year are shown. The 5th generation of mobile communication systems (5G) has been standardised by the industry and became commercially available in 2020. 5G systems will support gigabit-per-second mobile communications, which would enable massive machine-type communications for the Internet of Things (IoT) and ultra-low-latency ultra-reliable communications. The 5G spectrum usage has also been outlined by many countries, with numerous sub 10 GHz bands, 20-30 GHz bands and a few 40-70 GHz higher frequency bands. Due to the consideration of wavelength and environmental dimensions, the higher frequency bands are likely to be considered for fewer coverages but higher bandwidth hotspot usage.

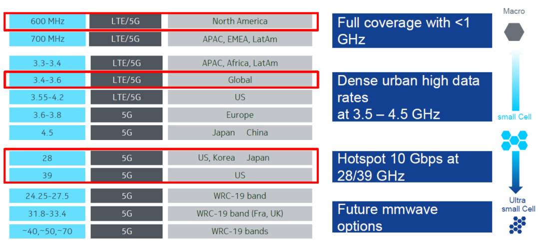

Figure 1.3: The spectrum usage of 5G.

In fig. 1.3, we can see some of the current 5G spectrum allocations: for <1 GHz bands (such as the 600 MHz band), this will provide a wide range coverage; for 3-4 GHz spectrum, this will support urban high data rates; for higher bands like the 28 GHz and the 39 GHz, these will be ultra fast (10 Gbps) short-range hotspots. From 2030 onwards, a 6th Generation

(6G) mobile communication system will be required to support Terabit per second (Tbps) data rates on mobile devices, an exponential surge in mobile traffic due to autonomous vehicles and an estimated 100 billion IoT devices. 6G will take the Internet in entirely new directions and opens the door for spectacular new applications such as brain-mobile interface and holographic teleportation.

5G communication links are expected to achieve up to 20 Gbps peak data rates between a transmitter and a mobile receiver. In contrast, the theoretical peak data rates achievable by 4G is 1 Gbps. This massive leap in communication speed is only possible because 5G systems will operate in much higher frequencies than 4G systems, in the so-called millimetre-wave frequency between 24-100 GHz, where up to 100 times more bandwidth is available.

The fundamental speed limits of wireless communication systems are set by the Shannon Capacity formula, which holds that the maximum data rates in the wireless channel increase linearly with the available bandwidth and logarithmically with signal power:

$$C = B \log_2(1 + \frac{S}{N}) \tag{1.1}$$

Where C represents the bandwidth available in Hz, $\frac{S}{N}$ is the signal-to-noise-ratio. Therefore, the only feasible way to achieve Tbps mobile communications in 6G is to move to the so-called Terahertz region of the radio spectrum, ranging from 0.1-10 THz, where another 100-time increase in the available bandwidth can be achieved. Although the noise is dependent on the bandwidth and tends to increase with higher bandwidths, with advancements in signal processing technologies and theories, one can minimise the effects of noise due to bandwidth increase. The terahertz frequency range has been intensively researched for a range of short and ultra-short-range communication applications, such as medical imaging, security, spectroscopy and on-chip communications. There have also been very recent and impressive advances in THz photonic technologies for ultra-short (less than a meter) point-to-point wireless communications. However, up to now, THz frequencies have been "terra incognito" for mobile communications.

1.2 Challenges and Motivations

As we move up into the THz frequency regime, the wavelength of EM waves becomes smaller; in fact, at the top of the newly opened spectrum, the wavelength of 3 THz EM wave is merely 0.1 mm, which really brings THz propagation towards the analogy of light propagation, where ordinary objects will create shadows or blind spots that are unreachable by EM wave source. As a result, many of the locations that were previously reachable by radio waves of lower frequencies will become new blind spots in the THz spectrum. As we have progressed into the 5G era, one of the solutions to tackle the new "shadow-locations" millimetre wave propagation is by using even more sub-cellular stations (small cells) so that the signal coverage is better. Although effective, it is nonetheless costly to popularise entire cities with at least double the number of existing cells, not to mention that at higher frequencies, even more small cells would be needed (so exponentially cost-ineffective).

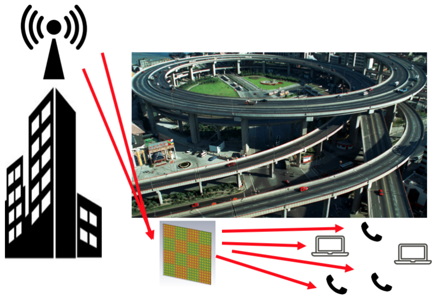

Figure 1.4: A visualisation of the possible application in further connecting users that are in NLOS locations, such as those under elevated roads or bridges.

A possible use-case scenario is illustrated in fig. 1.4: a small cell is located on the roof of a building, while the reflectarray is situated next to the bridges below the building; the reflectarray will then strengthen the signal by directionally propagating the reflected signal (from the small cell) towards user locations. Reconfigurable metasurfaces could be another remedy/solution that will help signals reach NLOS locations meanwhile immensely reducing the cost, as compared to that of building a microcell. This is because a reconfigurable metasurface, such as a reflectarray metasurface, does not require power for the generation of radio signals, which the small cells do. A reflectarray metasurface simply reflects the impinging EM waves from the cell station to the user's desired direction and manner, through the electronic configuration of unit cell status, which normally requires a relatively small amount of electrical power (as compared to a transmission antenna).

Another issue associated with THz wave propagation for wireless communication is the free space path loss, which increases with the square of frequency and distance (between transceivers), making long THz links a challenge. This means that traditional phase arrays, which are used to achieve beamforming ability, do not scale well - a 28 GHz 5G transmitter may integrate 1024 antennas to achieve a 1 Gbps data rate over 200 m (e.g. for fixed wireless access), while a 300 GHz 6G transmitter would require 100,000 antennas in order to achieve similar communication range.

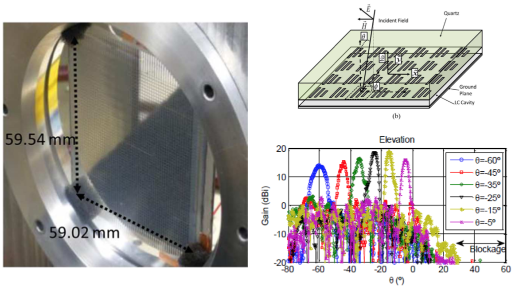

Figure 1.5: LC-based reflectarray antenna operating at F-band[62].

Reconfigurable metasurface could also be a cost-effective remedy to the free space path loss problem in THz wireless communication. A reflectarray metasurface can be programmed into the "beamforming mode"; hence, it can be deployed as a secondary beamforming device from the small/microcell, enhancing the signal strength at the receiver by further increasing the gain of signal, which will greatly relieve the gain requirements from THz small cell stations.

Another benefit of researching reconfigurable metasurfaces is that they tend to be small in size (e.g. around the order of hundred wavelengths, so less than a meter), and their quasi-passive nature (not radiating EM waves on their own, just reflecting EM waves) make them convenient for installations and even reallocations. In fig. 1.5, the researchers have developed a 60 mm x 60 mm large F-band LC-based reconfigurable reflectarray; the unit cell schematics and beam-scanning results are also shown.

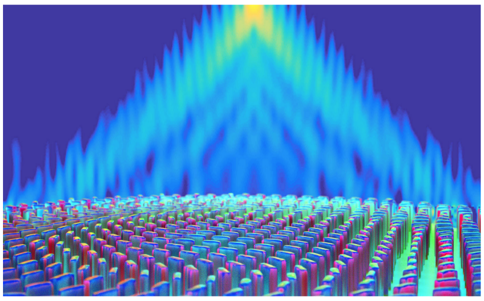

Figure 1.6: The metalens developed by SEAS at Harvard[8, 37], which operates at the full visible spectrum.

Another branch in the study of metasurfaces that will be touched on is the dielectric-based and graphene-based metasurfaces. In fig. 1.6, the team at Havard has developed a dielectric-based metasurface that is able to focus visible light through the manipulation of dielectric resonators' geometrical/dimensional properties. As discussed, the free space path loss associated with high-frequency waves is a key challenge to achieving high bandwidth and distance communication. Therefore, beamforming will be a crucial area to explore. With traditional metal antennas, their lossy nature is accentuated at millimetre frequencies, whereas dielectric resonators such as ceramics can be a much more energy-efficient solution as an antenna. Metalens with dielectric resonators also have advantages both over traditional lenses as well as over geometric phase or plasmonic-based metalenses. Plasmonic devices, though powerful near-field enhancers, have the inherent nature of lossy nature away from local field confinement. Geometric or Berry's phase metalenses, although comparatively more energy-efficient, require the use of circularly polarised EM waves, which currently can be a challenge to implement cost-effectively and prevalently. Metalenses built with dielectric resonators can be a more suitable solution to millimetre wave propagation, as it works with linearly polarised EM wave, it is not lossy at millimetre wave frequencies, and the lens size will be immensely smaller than traditional dielectric lenses (thickness can be smaller than the wavelength of interest).

There are great potentials in using dielectric-based alternatives to traditional optical devices, which often utilise crystalline dielectrics, such as stacked crystallines for devices like quarter-wave plates. These natural materials have limitations such as bulky structure, high reflection and absorption losses, as well as narrow-band operation. For a stacked crystalline quarter-wave plate, the transmission power can be limited to less than 55%[12, 48]. By engineering sub-wavelength dielectric resonators, one can achieve a purposely built metasurface tailored to exhibit specific properties while improving the thickness (through the implementation of abrupt surface phase change), efficiency (nature of dielectrics) and bandwidth. Metasurfaces that make use of plasmonic elements and excitation with circularly polarised waves have been shown to possess the ability of harmonic generation. This is another potential interest in the wireless communication field, as the THz wave generation is a commercially relatively underdeveloped field; together with the even larger power requirements than previous base station radiation powers (due to the path loss), the THz source is another challenge in the commercial landscape of wireless communication.

In summary, this PhD thesis will be focused on the study of reflectarray metasurfaces, optimisation algorithms tailored to pattern synthesis problems, as well as some preliminary studies on alternative metasurfaces for the application in 5G-and-beyond wireless communication.

1.3 Novel Contributions

The main contributions of this thesis can be listed in five sections: 1) the design and simulation of an LC-based binary reconfigurable reflectarray, 2) an in-depth scalability analysis of reconfigurable reflectarrays, 3) the implementation of an adaptive GA and the development of a modified GS iterative algorithm that is tailored to reconfigurable reflectarray phase-retrievals and pattern synthesis, 4) the development of a cross-platform routine that involves CST, VBA, and Matlab, which covers the design, semi-analytical/fullwave simulation, and phase retrieval/pattern synthesis optimisation, 5) a dielectric-based reflectarray that is designed to convert between linearly and circularly polarised EM waves and reflect towards a specifically designed direction.

At the beginning of my PhD research on reflectarrays, there were already groups working on reconfigurable reflectarrays that were based on lumped elements (such as PIN diodes or varactor diodes)[18, 80, 75, 56, 74, 24]. Only more recently did researchers start to implement LC-based reconfigurability into reflectarray designs[35, 7, 65, 36]. The earlier designs of lumped element-based reconfigurable reflectarrays have the advantage of a high degree of reflection beam control due to the individually biased antennas; however, the lumped elements (specifically diodes) suffered high parasitic losses at high frequencies. The LC-based reflectarrays, while proving to be more suitable for high-frequency EM radiation, have been designed with line-by-line addressing techniques, limiting the performance of the reflectarray to be one-dimensional and singled-beamed. The originality of this research is in combining the benefits of LC-based resonators for high-frequency EM radiation, with the benefits of individually addressed antennas for a more advanced high-frequency reconfigurable reflectarray design, at a much higher frequency (108 GHz) as compared to the current reconfigurable reflectarray devices.

Additionally, the author has conducted an in-depth analysis of the scalability of the LC-based reconfigurable reflectarray. In this analysis, parameters such as the phase degree of control (1-bit, 2-bit, continuous control), element spacing, and aperture size are varied to compare how KPIs (half-power beamwidth, sidelobe level, directivity, and tangent deviation) would change. This offers a comprehensive basis for future construction of the LC-based reconfigurable reflectarray, as it details the KPI requirements to the manufacture parameters. Furthermore, a cross-platform routine that covers the CST parametrisation, Matlab post-processing, Matlab phase optimisation, and VBA/CST full-model automation and time-domain simulation is presented: this generalised procedure can be up-downscaled to other frequencies and with other means of phase-change mechanisms.

Another novelty of this PhD research lies in the development of a pattern synthesis algorithm that greatly fastens the optimisation times for retrieving the input phases of exotic beam patterns. The author imagined an integrated product, where the reflectarray is combined with the feed source, as well as an integrated processor that can produce needed inputs "on-the-spot", without needing this information to be propagated over the channel (and hence compromising the capacity). Traditionally[80, 7], optimisation algorithms such as GA and PSO have been utilised to retrieve the reflectarray's surface phase distribution for a given desired farfield electric field pattern. These optimisation methods take a large number of iterations (where each iteration can be a large combination of multiple inputs) to converge to a satisfactory standard. Therefore, it would be impractical to solve phase problems "on-the-spot" with a sufficiently low computation time.

During my PhD research, Professor Rupert Young, who worked in the field of imaging, introduced me to the GS iterative algorithm, which was applied in the imagining field for retrieving lost phase information when transforming between the image and diffraction planes. This method has then been applied to holographic metasurfaces' phase retrievals, where researchers can produce the required surface phase distribution on the holographic metasurface given a desired hologram. We immediately spotted that this algorithm could be translated in the domain of array antenna's pattern synthesis. Following modifications to the algorithm, the author is able to develop a modified GS algorithm that is tailored to array antenna's pattern synthesis, which is significantly faster than traditional optimisers such as GA and PSO (in some cases improving from hours of optimisation time down to tens of seconds), especially for larger device dimensions.

Lastly, using the cross-platform routine developed by the author, a dielectric-based polarisation converting reflectarray is introduced. The construction and development concepts are similar to those of the LC-based reflectarray, although here, the dielectric resonators are not reconfigurable but polarisation-converting (specifically converting between spherical and linear polarisations). These dielectric reflectarrays are thinner than traditional quarter wave plates that utilise crystalline quartz[12, 48], which requires the EM wave to propagate through a thicker medium to achieve the delay/rotation of phases and thus usually have lower efficiencies. Additionally, this design offers the possibility to now be constructed to reflect towards a specific direction without the need to mechanically reposition the device.

Chapter 2

Summary

In Part-I of the thesis, there is one chapter, "Research Context and Novelty", which includes three sections: "Wireless Communication background", "Challenges and Motivations", and "Novel Contributions".

In "Wireless Communication Background", the author established the historical and contextual background for the wireless communication field, introduced the cellular communication generations and corresponding industry standards.

In "Challenges and Motivations", the author introduced the difficulties faced in high-frequency wireless communications, namely the high path-loss, non-line-of-sight, and thus challenges faced by phased arrays. Also in this section, the motivations of the PhD research are introduced, which focuses on alleviating the challenges of traditional phased arrays with the introduction of reconfigurable reflectarrays and other types of novel metasurfaces. In addition, the author has developed a faster pattern synthesis and phase retrieval algorithm that is tailored to reflectarray applications, and has the potential to function onboard the device in the "online" state.

In "Novel Contributions", the author summarised the novel aspects of this PhD work and how they contribute to the field of research, which in short are the LC-based reconfigurable reflectarray, pattern synthesis and phase retrieval algorithm, scalability analysis, and dielectric-based quarter-wave plate metasurface.

Part II

Theoretical Background

Chapter 3

Electromagnetism

3.1 Antennas

The Maxwell's equations define the EM wave propagation in space; it is not a surprise that we can also get an intuitive understanding of how antennas generate EM waves to propagate as signals in space by looking at the equations:

$$
\begin{aligned}
\nabla \cdot \vec{D} &= \rho_v \\
\nabla \times \vec{E} &= -\frac{\partial \vec{B}}{\partial t} \\
\nabla \cdot \vec{B} &= 0 \\
\nabla \times \vec{H} &= \vec{J} + \frac{\partial \vec{D}}{\partial t}
\end{aligned}
\tag{3.1}
$$

where $vecD$ is the electric displacement field, $\vec{H}$ is the magnetic displacement field, $\vec{E}$ is the electric field, $\vec{B}$ is the magnetic field, $\vec{J}$ is the current, and ρ_v is the charge density. When we supply an alternating current to a dipole antenna, by looking at the $\nabla \times \vec{H}$ from equation. 3.1, we can have some insights as to how EM waves are generated: with an alternating current through a wire, that means not only do we have magnetic field $\vec{H}$ from current $\vec{J}$, but also a change in the magnetic field, due to the varying of the displacement current $\frac{\partial \vec{D}}{\partial t}$ term (since charges are accelerating) that is not a constant. Then, looking at the $\nabla \times \vec{E}$ term, due to the varying of the magnetic field, we have a non-zero $\frac{\partial \vec{B}}{\partial t}$ term. Therefore, we get an electric field induced from the change in the magnetic field, which of course, once again induces a magnetic field, and the loop of EM generation continues indefinitely.

Therefore, one of the necessary conditions for the generation of propagating EM waves from antennas is the acceleration of charges. This could be achieved in many ways; for instance, an alternating current will cause the charges to accelerate and decelerate when the current changes direction, hence inducing EM fields; but one could also achieve the acceleration of charges geometrically by using DC current but enforcing the current to travel along non-linear paths (e.g. a circular loop). Hence the change in the direction of charges will also result in acceleration and produce EM waves.

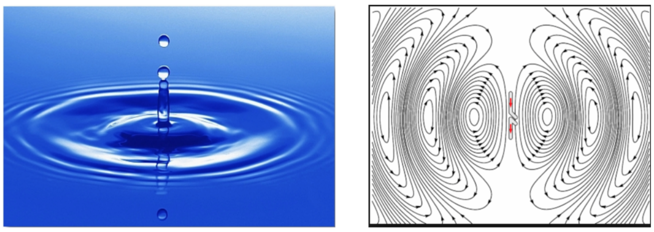

Figure 3.1: The analogies between water wave propagation and EM waves caused by dipolar disturbances in the form of water droplet and dipole antenna[5].

Not surprisingly, this can be very analogous to water waves formed when disturbed by a droplet, which is shown in fig. 3.1: the disturbance of an accelerating/decelerating droplet (which is similar to an electric dipole as droplet motion is two-dimensional) caused the propagation of disturbance in the form of mechanical waves to travel through the water medium in all directions. This is similar to how the accelerating/decelerating of electrical dipole “droplet“/charges causes disturbance of space-time medium which is propagated through the form of EM propagation in all directions.

3.1.1 Field Regions

The field regions relative to the antenna have usually been divided into three areas: a) reactive nearfield, being the closest to the antenna, b) radiating nearfield (Fresnel), and c) farfield, being the furtherest from the antenna. The classification of these field regions serves to help separate different areas of interest, as the physics involved can be quite different in these regions.

Reactive near-field is defined as distance $R < 0.62\sqrt{D^3/\lambda}$, where R is the distance, D the dimension of the antenna and λ the wavelength. Radiating nearfield is only valid for antennas for dimensions $D > \lambda$, where it is defined to be the region greater than reactive nearfield but less than $2D^2/\lambda$. In the reactive nearfield and sometimes radiating near-field, rich physics involving coupling of the resonators and plasmonics excitation/coupling may occur. Hence the analytical descriptions may become very complicated as the complexity of the system rises. Farfield is defined as distances greater than radiating nearfield.

3.1.2 Power Density and Directivity

The power density gives the direction and magnitude of energy flow of the EM waves; it is given by the Poynting vector in electromagnetism, which is the cross product between the electric field vector **E** and the magnetic field vector **H**:

$$S_{avg} = \frac{1}{2}\,\mathrm{Re}\Big\{\tilde{\mathbf{E}} \times \tilde{\mathbf{H}}^{*}\Big\} \tag{3.2}$$

with the power density, the directional pattern of the antenna's radiation is given by the normalised radiation intensity $F(\theta, \phi)$, which is defined as the ratio between power density to the maximum value of power density, S_{max}:

$$F(\theta, \phi) = \frac{S(R, \theta, \phi)}{S_{max}} \tag{3.3}$$

The directivity of any given antenna is then related to the normalised radiation intensity by

$$D = \frac{1}{\frac{1}{4\pi}\int_0^{2\pi}\int_0^{\pi} |F(\theta, \phi)|^2 \sin\theta d\theta d\phi dx} \tag{3.4}$$

This is simply the maximum directivity (1) over the averaged directivity or power radiated over all directions. It is important to note that directivity is usually expressed in decibels, which refers to the ratio of antenna directivity to that of an omni-directional ideal dipole antenna (directivity of 1). Hence, an omnidirectional radiating antenna has a directivity of 0 dB. Some common antennas and their usual directivities are shown in the table below:

Antenna	Directivity	Directivity (dB)
Short Dipole	1.5	1.76
1/2	1.64	2.15
Patch	3.2-6.3	5-8
Horn	10-100	10-20
Dish	10-10000	10-40

Table 3.1: Antenna types and corresponding directivities.

Therefore, a shorter pulse of propagating charges will generate a broader spectrum of propagating EM frequencies, while a more continuous time-harmonic current will generate a narrower and more precise frequency of propagating EM waves. This can be seen from the mathematical relation between the current distribution and the farfield pattern: the farfield (or directivity) of the antenna can be thought of as the Fourier transform of the current distribution on the antenna, hence localisation in one results in broadness in the either, and vice versa.

In table. 3.1, a list of common antennas and their directivity values have been listed. We see that the short dipole antenna has the lowest directivity of 1.76 dB, due to the rather omnidirectional radiation pattern; whereas the dish antenna has the greatest directivity of 10-40 dB, depending on the aperture, due to their highly directional focusing capabilities. Therefore, dish antennas are often used for longer distance radio communications as compared to short dipole antennas.

3.1.3 Antenna Efficiency

The efficiency of an antenna quantifies the ratio between input feed power and the output radiation power; in other words, it shows how much of the power used in exciting the antenna is transferred into EM radiation, and how much is "wasted" in the process, either through material absorption, or reflection from impedance mismatch, or other means of wastage. The radiation efficiency of an antenna is defined as the ratio of radiated power $P_{radiated}$ and input power P_{input}:

$$\varepsilon_R = \frac{P_{radiated}}{P_{input}} \tag{3.5}$$

In the decibel units, the ratio is with respect to a perfectly efficient antenna (100% efficiency). Hence a 10% efficiency corresponds to -10dB, and 50% corresponds to -3dB. If we put into consideration the loss associated with impedance mismatch ($0 < M_L < 1$), then the total efficiency of antenna ε_T is defined as:

$$\varepsilon_T = M_L \cdot \varepsilon_R \tag{3.6}$$

3.1.4 Antenna Gain

The antenna gain is defined as the "power transmitted in the direction of maximum radiation to that of an isotropic source". Often antenna gain is used over the directivity in experimental studies/industries, as the gain takes into consideration of losses, whereas directivity does not. The formula for antenna gain is the product of antenna efficiency ε_R with antenna directivity D:

$$G = \varepsilon_R D \tag{3.7}$$

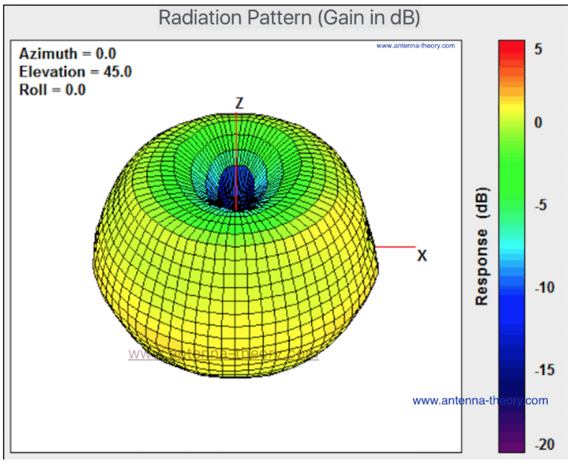

Figure 3.2: Antenna gain in dB[6].

In fig. 3.2, we have the radiation pattern in dB of a short dipole antenna, with the dipole aligned in the z-direction. We can see that the radiation pattern is symmetrical in the z-direction, with a maximum value of around 5 dB. We also notice how omnidirectional the radiation pattern is, due to the dipolar nature of the radiator.

3.1.5 Effective Aperture

The effective aperture is a concept that comes up we think of antennas as receivers rather than transmitters. Suppose a plane wave is incident on an antenna, then the effective aperture is a measure of how well the antenna can deliver the energy of the plane wave to a load. It is thus defined by the ratio between plane wave power density $S_{incident}$ and the intercepted power P_{int} that is delivered to a matched load:

$$A_e = \frac{P_{int}}{S_{incident}} \tag{3.8}$$

It is also related to the gain by:

$$A_e = \frac{\lambda^2}{4\pi} G \tag{3.9}$$

3.1.6 Friis Transmission Formula

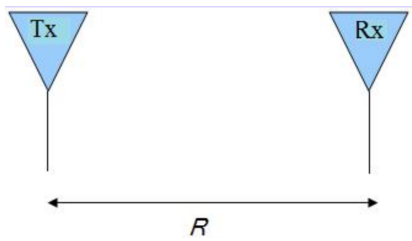

Figure 3.3: The Friis transmission formula applied to transmit and receive antennas.

The Friis Transmission formula is used when calculating the transmission power associated with a two-antenna system, under frequency f, separated by distance d and where G_T, G_R, P_T and P_R are the transmit antenna gain, receive antenna gain, transmit power and received power:

$$P_R = \frac{P_T G_T G_R c^2}{(4\pi df)^2} \tag{3.10}$$

When logarithmically expressed, the equation becomes:

$$P_R = P_T + G_T + G_R + 20\log_{10}\left(\frac{c}{4\pi df}\right) \tag{3.11}$$

A graphical representation of the Friis equation's formulation is shown in fig. 3.3.

3.1.7 Beamwidth

Beamwidth is a concept used to quantify the directivity level of the antenna. An antenna farfield, apart from the main maximum directivity, which is known as the main lobe, usually also exhibits minor/side directivities, known as side lobes.

The quantify the main lobe beamwidth, we could either use the half-power-beamwidth (HPBW), which is the angle enclosed by 50% reduction in the farfield power, or the null to null beamwidth, which is the angle enclosed by the zeros of the main lobe. To quantify side lobes, the sidelobe level (SLL) is used, which simply takes the maximum value of the side lobe.

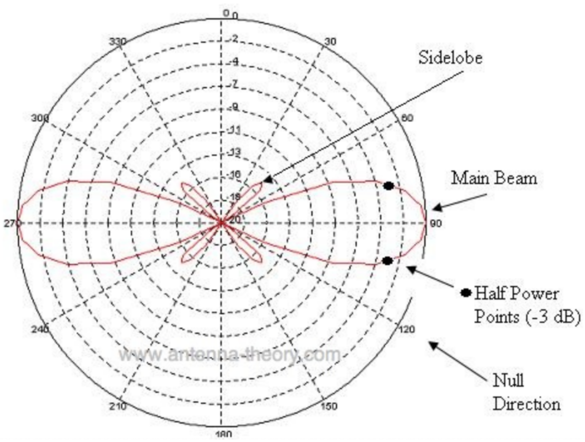

Figure 3.4: Beamwidth illustrated[6].

In fig. 3.4, there is an illustration of the definitions of half-power beamwidth, mainlobe, and sidelobe, on a polar plot of directivity.

3.1.8 Farfield of Hertzian Dipole

A Hertzian dipole is also known as a short dipole due to the fact that its linear conducting “arms” must not exceed $\lambda/50$. Let us use the Hertzian dipole defined in fig. 3.5, where Q is the observation point, R is the distance to the observation point from the coordinate centre, R’ is the distance from the infinitesimal segment of the dipole to the observation point, θ and ϕ are the angles extended by R with respect to the coordinate centre.

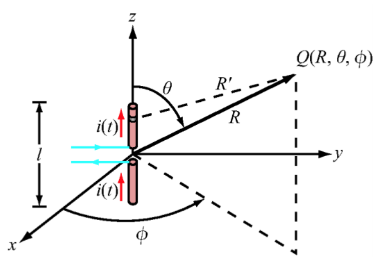

Figure 3.5: Hertzian Dipole[72].

Assume that the current driving this antenna is $i(t) = I_0 \cos \omega t = \mathrm{Re}\{I_0 e^{i\omega t}\}$, we can find out the expression for vector potential:

$$\tilde{\mathbf{A}}(\mathbf{R}) = \frac{\mu_0}{4\pi} \int_{v'} \frac{\tilde{\mathbf{J}} e^{-ikR'}}{R'} dv' = \frac{\mu_0}{4\pi} \frac{e^{-ikR}}{R} \int_{-l/2}^{l/2} \hat{\mathbf{z}} I_0 dz = \hat{\mathbf{z}} \frac{\mu_0}{4\pi} I_0 l (\frac{e^{-ikR}}{R}) \tag{3.12}$$

where R is the distance from the origin to observation point Q, R' is the distance from the infinitesimal section of the dipole to the observation point Q, μ_0 is the vacuum permeability, ε_0 is the vacuum permittivity, $\mathbf{J}$ is the current vector, v' and dv' are the volume and volume integral, ω is the angular frequency of the EM wave, I_0 is the amplitude of the current, l is the length of the dipole wire, θ and ϕ are the elevation and azimuth angles. We may then proceed to express the vector potential in terms of spherical coordinates, which yields:

$$\tilde{A}_R = \frac{\mu_0 I_0 l}{4\pi} \cos\theta (\frac{e^{-ikR}}{R}) \tag{3.13}$$

$$\tilde{A}_\theta = -\frac{\mu_0 I_0 l}{4\pi} \sin\theta (\frac{e^{-ikR}}{R}) \tag{3.14}$$

$$\tilde{A}_\phi = 0 \tag{3.15}$$

with which we can apply equations $\tilde{\mathbf{H}} = \frac{1}{\mu_0}\nabla \times \tilde{\mathbf{A}}$ and $\tilde{\mathbf{E}} = \frac{1}{i\omega\varepsilon_0}\nabla \times \tilde{\mathbf{H}}$, to arrive at the magnetic and electric field expressions of:

$$\tilde{H}_\phi = \frac{I_0 l k^2}{4\pi} e^{-ikR} \left[\frac{i}{kR} + \frac{1}{(kR)^2}\right] \sin\theta \tag{3.16}$$

$$\tilde{E}_R = \frac{2 I_0 l k^2}{4\pi} \sqrt{\mu_0/\varepsilon_0} e^{-ikR} \left[\frac{1}{(kR)^2} - \frac{i}{(kR)^3}\right] \cos\theta \tag{3.17}$$

$$\tilde{E}_\theta = \frac{I_0 l k^2}{4\pi} \sqrt{\mu_0/\varepsilon_0} e^{-ikR} \left[\frac{i}{KR} + \frac{1}{(kR)^2} - \frac{i}{(kR)^3}\right] \sin\theta \tag{3.18}$$

When taking the farfield approximation, we assume $R \gg \lambda$, therefore we can neglect the terms with $1/R^2$ and $1/R^3$, resulting in simplified farfield expressions for the Hertzian Dipole:

$$\tilde{E}_\theta = \frac{i I_0 l k \sqrt{\mu_0 \varepsilon_0}}{4\pi} \left(\frac{e^{-ikR}}{R}\right) \sin\theta \tag{3.19}$$

$$\tilde{H}_\phi = \frac{\tilde{E}_\theta}{\sqrt{\mu_0 \varepsilon_0}} \tag{3.20}$$

and the corresponding field looks like:

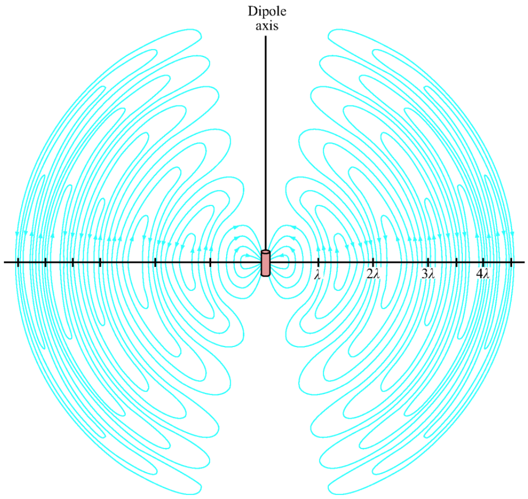

Figure 3.6: Hertzian Dipole farfield plot[72].

Applying the Poynting vector calculations, we get that the power density $S = S_0 \sin^2 \theta$, and its max value $S_{max} = S_0$, therefore the normalised radiation intensity:

$$F(\theta, \phi) = \frac{S}{S_{max}} = \sin^2 \theta \tag{3.21}$$

If we were to plot the normalised radiation intensity, then we would get (in polar form) the plot displayed in fig. 3.6. Here, we notice how each current oscillation would produce a "blob" of EM disturbance propagating outwards from the dipole.

3.1.9 Phased Arrays

Phased arrays date back to as early as 1905 when Nobel laureate Karl Ferdinand Braun showed the improved transmission of radio signals in specified directions. Ever since, phased arrays have been greatly researched and developed, first by the military for radar communications during the first and second world wars and then by commercial companies focusing more on civilian wireless communications applications.

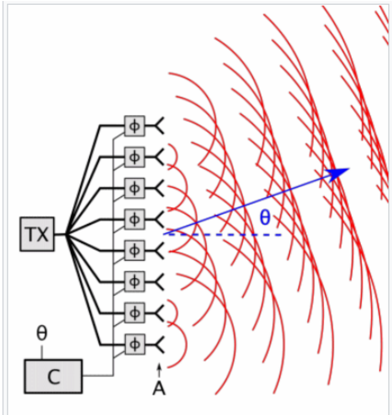

Figure 3.7: Phased array antenna will send EM signals from each antenna in a way that will focus EM waves precisely to give constructive interference at the desired receiver location.

The working principle of phased arrays is relatively straightforward and illustrated in fig. 3.7: multiple antennas are arranged in arrays, where each antenna element is designed to generate radio waves at a specific time, so that the overall radio wave signal strength at the intended receiver location is maximised. The reason that radio wave signal strength can be augmented from such a device is due to the fact that EM waves generated from the antennas at different times have different phases, and as a result, waves with different phases can be designed to constructively interfere with each other.

3.1.9.1 Array Factor and Space Factor

For a linear phased array in the z-direction (illustrated in fig. 3.8), with d spacing and N elements, the distance R_i from ith element to farfield observation point Q is approximately $R_0 - id\cos\theta$, since the distance can be approximated as parallel to each other when Q is far away.

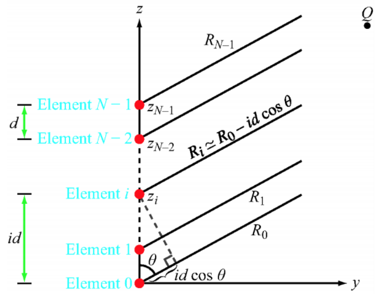

Figure 3.8: Distances from unit antenna elements to farfield observation point[72].

Assuming that the phased array is made of identical unit antennas, then the corresponding antenna power density (which gives the farfield pattern) is given by a summation of the electric field (squared) from all the individual antenna elements to observation point Q:

$$\begin{aligned} S(R,\theta,\phi) &= S_e(R,\theta,\phi)\left|\sum_{j=0}^{N-1} A_j e^{ijkd\cos\theta}\right|^2 \\ &= S_e(R,\theta,\phi)F_a(\theta) \end{aligned} \tag{3.22}$$

where the array factor is $F_a(\theta)$ and the $S_e(R,\theta,\phi)$ is the power density radiated from the unit antenna element. The array factor is a function dependent on the location of the unit antenna element and their corresponding feeding coefficients A_j, while independent of the type of antenna or other intrinsic radiation properties. The intrinsic radiation properties are embedded in S_e; it is left out of the summation because we have assumed that all antenna unit elements are the same, hence do not differ in type and radiation properties. The antenna feeding coefficient is a complex quantity, quantifying both the magnitude and phase adjustments that are provided to each unit antenna element in the phased array.

The array factor applies to the discrete distribution of sources; however, as the number of antenna elements increases, we approach the continuous limit, where an integral can be substituted for the summation in the array factor - the continuous limit with the integration of the array factor is known as the space factor and is given by:

$$SF(\theta) = \int_{-l/2}^{l/2} I_n(z')e^{i(kz'\cos\theta + \phi_n(z'))}dz' \tag{3.23}$$

3.1.9.2 Uniform Phase/Excitation of N-element Array

$$F(\theta) = |\sum_{j=0}^{N-1} a_i e^{i\phi_j} e^{ijkd\cos\theta}|^2 \tag{3.24}$$

For a uniform phase distribution, the $e^{i\phi_j}$ in the radiation intensity $F(\theta)$ becomes a constant and factored out of the summation as $|e^{i\phi_0}|^2$, which is equal to 1. Thus,

$$F(\theta) = |\sum_{j=0}^{N-1} e^{ijkd\cos\theta}|^2 = |\sum_{j=0}^{N-1} e^{ij\gamma}|^2 \tag{3.25}$$

where $\gamma = kd\cos\theta$. From a series of algebraic manipulations, it can be shown that:

$$F(\theta) = \frac{\sin^2 N\gamma/2}{\sin^2 \gamma/2} \tag{3.26}$$

If we were to plot this function for a six-element array (N=6) and spacing of half wavelengths ($d = \lambda/2$) then we would get fig. 3.9:

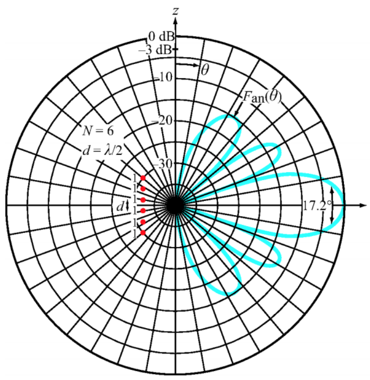

Figure 3.9: Uniform phase distribution pattern function of six-element array, where spacing is half wavelength[72].

An important point to note here is that the main lobe is in the boresight direction, perpendicular to the structure, also confirming with Huygens' principle: if we think of each antenna element as a source of spherical wave generation, then when we add up a uniform phase plane of spherical waves, we get a plane wave propagating at the boresight direction.

3.2 Scattering Theories

3.2.1 Huygens' Principle

Huygens' principle states that each point on a wavefront can be considered as an individual source of a propagating spherical wave, and the sum of these spherical waves in turn produces another wavefront. In fig. 3.10, we illustrate diffraction and refraction viewed with Huygens' principle. In the case of diffraction, we can see that by producing a spherical wave at each point of the opening, the edge elements contribute to the diffractive effect. In the case of refraction, we see that due to the time difference between arriving EM radiation, the spherical waves radiate outward at different times and contribute to a refracted wavefront.

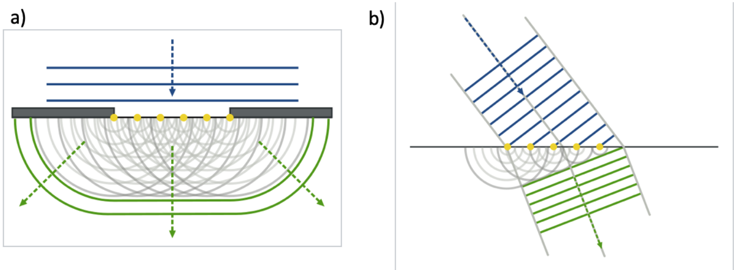

Figure 3.10: a) and b) diffraction and refraction viewed with Huygens' principle[16].

This is an important principle in arrayed antenna radiation propagation; in arrayed antenna, each element antenna is an actual single source of spherical wave (assuming a dipole antenna), and thus with Huygens' principle, one can construct the antennas in an appropriate manner such that the outgoing waves form a wavefront in the desired manner (e.g. beamsteering towards a specific direction).

3.2.2 Dielectric Resonator

Traditionally dielectric resonators, which are usually made from dielectrics with $\varepsilon_r > 20$, have been used in microwave circuits as oscillators or filters, mainly because of their low loss or high Q-factor characteristics, with some having a Q-factor of 10,000. Although the idea of a dielectric resonator antenna was long proposed, it was not until more recently did it gain significant interest. This is due to the increasing interest in the higher frequency spectrum, such as THz/millimetre wave application, and the fact that traditional metallic resonators become rather lossy at these frequencies hence limiting efficiencies, whereas dielectric resonators' source of loss is much smaller (in fact only due to the imperfect material compositions). It is this low loss quality that has grasped the author's attention, as in THz wireless communication, one of the main challenges in establishing stable long-distance links is the high free space path loss, which means either high power THz source or high gain antennas are needed; dielectric resonator antennas can be a solution to alleviate the THz power requirements from the reduced loss in comparison to metallic antennas.

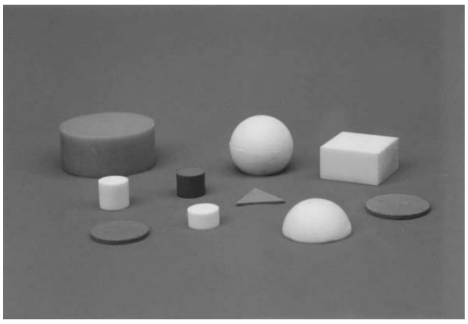

Figure 3.11: Different types and geometries of dielectric resonator antennas[39].

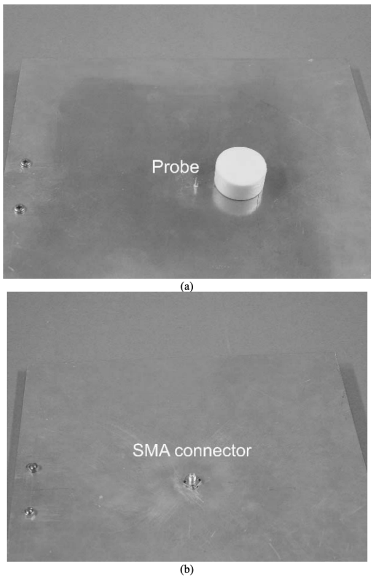

Figure 3.12: a) the dielectric resonator antenna and the probe which is used to excite it. The probe will be inserted inside the antenna b) the back side of the ground plane is the connector for the coaxial probe[39].

In fig. 3.11, we show some of the different types and geometries of dielectric resonator antennas. The most common geometries are the rectangular and cylindrical resonators. The cylindrical dielectric resonators are advantageous in terms of ease of production and ability to excite multiple modes. The rectangular dielectric resonators are advantageous in terms of design flexibility and low cross-polarisation levels. In fig. 3.12, we show a typical excitation method for the dielectric resonator antennas: the coaxial feed. This includes a coaxial line feeding through the bottom of the ground plate, with a central signal pin that runs to the inside of the dielectric resonator antenna on the other side of the plate (the radiation plane).

Other advantages of the dielectric resonator antenna include their smaller size, lower cost (e.g. ceramic is often used) of production, similar feeding mechanism as the traditional patch antenna and usually a wider impedance bandwidth than the patch antennas (around 10% for $\varepsilon_r = 10$). The wavelength of the EM wave within a dielectric resonator is smaller than that of in free space by a factor of $1/\sqrt{\varepsilon_r}$; thus, by using a dielectric resonator with higher permittivity values, we can significantly reduce the already subwavelength size antennas.

The scattering fields of the dielectric resonators can be solved in a similar fashion to the derivation of Mie theory scattering fields, with slightly adjusted boundary conditions, which is shown in the following sections. For a cylindrical dielectric resonator antenna, the wave functions of the transverse electric $Phi_{TE_{npm}}$ and the transverse magnetic $Phi_{TM_{npm}}$ modes are expressed as:

$$\Phi_{TE_{npm}} = J_n(\frac{X_{np}}{a}\rho)\begin{bmatrix}\sin n\phi \\ \cos n\phi\end{bmatrix}\sin\frac{(2m+1)\pi z}{2d} \tag{3.27}$$

$$\Phi_{TM_{npm}} = J_n(\frac{X'_{np}}{a}\rho)\begin{bmatrix}\sin n\phi \\ \cos n\phi\end{bmatrix}\cos\frac{(2m+1)\pi z}{2d} \tag{3.28}$$

where J_n is the Bessel function of first kind, and $J_n(X_{np}) = 0, J'_n(X'_{np}) = 0, n = 1, 2, 3..., p = 1, 2, 3, ..., m = 1, 2, 3, ...$ From the dispersion equation $k_{rho}^2 + k_z^2 = \omega^2\mu\varepsilon$, the resonant frequency can be given as:

$$f_{npm} = \frac{1}{2\pi a\sqrt{\mu\varepsilon}}\sqrt{\begin{pmatrix}(X_{np})^2 \\ (X'_{np})^2\end{pmatrix} + [\frac{\pi a}{2d}(2m+1)]^2} \tag{3.29}$$

3.2.3 Jones Calculus and Beam Manipulation

In fig. 3.13, we demonstrate the procedures of a circular polarisation conversion: firstly, unpolarised light is first passed through a linear polariser to get linearly polarised light; secondly, a quarter-wave plate is introduced in order to delay the orthogonal components of the electric fields by ninety degrees, which then creates a circularly polarised wave.

In order to better describe polarised light and its interactions with optical devices, Jones began using the vector representation of light, while describing optical elements with Jones matrices; the resulting light from the interaction between light and the optical elements can be then described by the mathematical operations between the Jones vector and Jones matrices. Jones calculus[14] is applied to fully polarised EM waves.

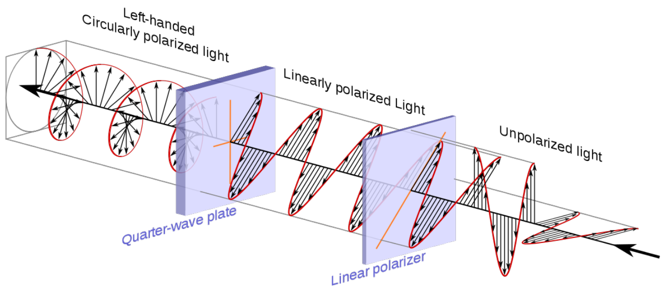

Figure 3.13: An unpolarised light travelling through a linear polariser, followed by a quarter-wave plate, which turns the final output light into a circularly polarised light[17]. The depicted amplitudes are those of the electric field.

A fully polarised EM wave that is propagating in the z-direction in free space can be described by its x, y and z electric components, with ϕ being the phase term, k the wave vector, ω the angular frequency, z the spatial axis, and t for time:

$$\begin{bmatrix} E_x(t) \\ E_y(t) \\ 0 \end{bmatrix} = \begin{bmatrix} E_{0x}e^{i\phi x} \\ E_{0y}e^{\phi y}i \\ 0 \end{bmatrix} e^{i(kz-\omega t)} \tag{3.30}$$

where the Jones vector describes the amplitude and phase information about the x and y-component of the electric field:

$$\begin{bmatrix} E_{0x}e^{i\phi x} \\ E_{0y}e^{\phi y}i \end{bmatrix} \tag{3.31}$$

Therefore, a x-direction linearly polarised light has a Jones vector representation of $\begin{pmatrix} 1 \\ 0 \end{pmatrix}$, a left-hand circularly polarised light: $\begin{pmatrix} 1 \\ i \end{pmatrix}$. Similarly, some common optical devices can be described with the Jones matrices, for example, a linear polariser in the x-direction has the representation of: $\begin{pmatrix} 1 & 0 \\ 0 & 0 \end{pmatrix}$, while a left-hand circular polariser can be described as: $\begin{pmatrix} 1 & -i \\ i & 1 \end{pmatrix}$, and a quarter-wave-plate with fast axis vertical: $\begin{pmatrix} e^{\frac{i\pi}{4}} & 0 \\ 0 & -ie^{\frac{i\pi}{4}} \end{pmatrix}$.

The Jones matrix for a birefringent dielectric unit cell can be expressed as:

$$\mathbf{J} = \begin{bmatrix} J_{xx} & J_{xy} \\ J_{yx} & J_{yy} \end{bmatrix} \tag{3.32}$$

and the input/output electric field can be established by $\mathbf{E^{out}} = \mathbf{JE^{in}}$. The Jones matrix can be further decomposed into its eigenvectors and eigenvalues, and for unit cells with rotational symmetries, such a a rectangular sub-wavelength dielectric resonator, the Jones matrix becomes:

$$\mathbf{J} = \mathbf{R}(\theta) \begin{bmatrix} S_x & 0 \\ 0 & S_y \end{bmatrix} \mathbf{R}(-\theta); \mathbf{R}(\theta) = \begin{bmatrix} \cos\theta & \sin\theta \\ -\sin\theta & \cos\theta \end{bmatrix} \tag{3.33}$$

Equation. 3.33 proves statement one: if the scattering parameter S_x, S_y and the rotation angle θ can be achieved (through the rotation operator $\mathbf{R}$), then the corresponding unitary and symmetric Jones matrix can be achieved[3]. This is an important premise to statement two: a metasurface that can achieve a unitary and symmetric Jones matrix at the individual unit cells is capable of complete phase/polarisation control[29].

In order to prove statement two: given the symmetric property, we have: $S_{xy} = S_{yx}$. The unitary condition states: $S_{xx}S_{xy}^* + S_{yx}^*S_{yy} = 0$. Expanding the electric field expressions ($\mathbf{E^{out}} = \mathbf{JE^{in}}$) and utilising the unitary condition of $|S_{xx}|^2 + |S_{xy}|^2 = 1$, we can arrive at the expression of input and output electric fields:

$$\begin{bmatrix} E_x^{out*} & E_y^{out*} \\ E_x^{in} & E_y^{in} \end{bmatrix} \begin{bmatrix} S_{xx} \\ S_{yx} \end{bmatrix} = \begin{bmatrix} E_x^{in*} \\ E_x^{out} \end{bmatrix} \tag{3.34}$$

Therefore, for any given electric field inputs and outputs, we can always find the scattering parameters S_{xx}, S_{yx} from Eq. 3.34, and S_{xy}, S_{yy} from the unitary and symmetry conditions:

$$S_{xy} = S_{yx} \tag{3.35}$$

$$S_{yy} = -exp(2i\angle S_{yx})S_{xx}^* \tag{3.36}$$

where $\angle$ is the angle. From the above, we can realise the control of the polarisation of EM waves and achieve devices with functionalities such as polarisation conversions or filters. In order to further manipulate the EM waves, we need a further degree of freedom: phase control. Polarisation control already includes the control of phase and amplitude, but we will need to precisely control this.

For a circularly polarised input EM wave $\mathbf{E^{in}} = \begin{bmatrix} 1 \\ \pm i \end{bmatrix}$, we can express the resulting output electric field by doing $\mathbf{JE^{in}}$, which results in:

$$\mathbf{E^{out}} = \mathbf{JE^{in}} = \frac{S_x + S_y}{2}\begin{bmatrix}1\\ \pm i\end{bmatrix} + \frac{S_x - S_y}{2}\exp(\mp i2\theta)\begin{bmatrix}1\\ \mp i\end{bmatrix} \tag{3.37}$$

This shows that the output EM wave consists of waves with two chiralities (the left and right terms have opposite chirality). The difference is that the right term now possesses an additional phase term of 2θ. This is the geometric phase (also known as the Pancharatnam-Berry phase) that is resulted from the rotation of the unit cells. Now, if one were to filter out the left term (with a half-wave plate, for example), the resulting wave would only consist of the right term, which has the additional phase term: this means that we can control the phase of the wave by solely adjusting the rotation angle of the unit cells.

3.2.4 Generalised Snell's Law

The generalised Snell Law is derived from applying Fermat's principle. Referring to fig. 3.14, taking light refracting off a surface with infinitesimal path difference, then their phase difference should approach 0:

$$[k_0 n_i \sin\theta_i dx + (\Phi + d\Phi)] - [k_0 n_t \sin\theta_t dx + \Phi] = 0 \tag{3.38}$$

where k_0 is the free space wave vector, n_i is the incident refractive index, n_t is the transmitted refractive index, θ_i the incident angle, θ_t the transmitted angle, and Φ and $d\Phi$ are the phase difference across the dx spatial difference. This leads to the generalised law:

$$\sin\theta_t n_t - \sin\theta_i n_i = \frac{\lambda_0}{2\pi}\frac{d\Phi}{dx} \tag{3.39}$$

The implication of the generalised Snell's Law is that one can achieve an arbitrary direction of refraction (θ_t, angle of transmitted light) through the design of a phase gradient along the interface. This fact is used by many planar metasurfaces to achieve diverse beam functionalities. It is important to note that if the phase gradient is 0, then we will have the conventional Snell's Law.

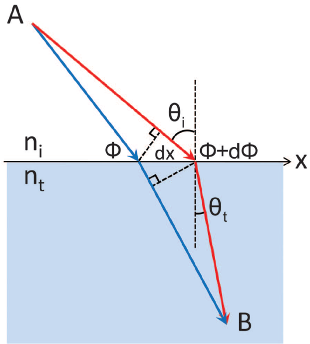

Figure 3.14: Schematics for generalised Snell's Law's derivation[83]. The abrupt phase change is introduced along the interface over the incremental distance dx for the incremental amount of $d\Phi$.

Chapter 4

Optimisation Techniques

4.1 Genetic Algorithm

GA is an optimisation method inspired by evolution; it searches for minimas/maximas, whether constrained/unconstrained global/local. The genetics in this algorithm refers specifically to the natural selection rule, which the algorithm aims to imitate.

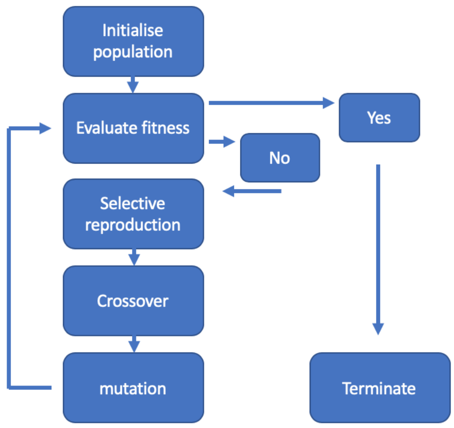

Figure 4.1: A typical cycle of the GA routine

In short, a GA optimisation process will generate an initial population of inputs (analogous to the first population of humans, usually randomised), from which it will carry out numerous reproductive operations that will randomly combine and mix the population, and then it will assess the best output (analogous to the best fitness of survival), and the few outputs that have the highest fitness values (known as the elites) will be retained and used as part of the input for the next iteration. This whole cycle will be repeated until the criteria of output are reached. A graphical explanation of the GA procedure is shown in fig. 4.1.

4.1.1 Initial Population and Fitness

Let us think of a population in terms of a simplified mathematical representation of DNA, where it is a one-dimensional array of numerical chromosomic values, and their fitness is given by some mathematical function that takes the inputs of each chromosomic value.

Table 4.1: The initial population of chromosomes and their corresponding values for their fitness.

Chromosme	Gene Values	Fiteness
ch 1	(2, 6, 1, 2, 9, 4, 7)	5
ch 2	(7, 1, 3, 6, 1, 9, 2)	21
ch 3	(2, 5, 4, 7, 1, 7, 1)	-15
ch 4	(8, 1, 2, 6, 8, 7, 2)	-23

In the example, table. 4.1, we have initialised with four chromosomic values and calculated their fitness according to a certain function that takes these values as inputs. When the initial population has been generated and their fitness values calculated, we then arrange these chromosomes according to their fitness. We can see that ch2 has the best fitness while ch4 has the worst.

4.1.2 Selective Reproduction, Crossover, Inversion and Mutation

Selective reproduction is rather straightforward: it merely chooses the least fit data set and throws it out of the pool. In our previous example in table. 4.1, we saw that ch4 gave the worst fitness value, and as a selective reproduction procedure, we can throw away this data.

A single point crossover, as shown in table. 4.2, draws a line at a specific chromosome location and swaps the remaining values between, in this case, the best and second-best fit chromosomes.

Table 4.2: Single-point crossover.

Single-point Crossover (1st-2nd)	
child 1	(7, 1, 3, 2, 9, 4, 7)
child 2	(2, 6, 1, 6, 1, 9, 2)

The double-point crossover, shown in table. 4.3, is straight forwards once we know the single-point crossover; here, we draw two lines and swap the values between, in this case, second and third-best-fit chromosomes.

Table 4.3: Double-point crossover.

Two-point Crossover (2nd-3rd)	
Child 3	(7, 1, 4, 7, 1, 9, 2)
Child 4	(2, 5, 3, 6, 1, 7, 1)

Uniform crossover chooses random locations of chromosomes to be swapped. In table. 4.4's example, we have used the first and third best fit chromosomes, and the swapping has been highlighted by dashed boxes.

Table 4.4: Uniform crossover.

Uniform Crossover (1st-3rd)	
child 5	(2, 6, 4, 7, 9, 7, 7)
child 6	(2, 5, 1, 2, 1, 4, 1)

Mutation, as the name suggests, is simply a completely randomised single chromosomic value random change. In table. 4.5, this is done by randomly choosing two points in the chromosome data set and changing their value randomly.

Table 4.5: Mutation.

Mutation (1st)	
child 7	(2, 6, 4, 2, 9, 1, 7)

The inversion is basically a complete reordering of the chromosome in the reverse chronological order. For instance, as depicted in table. 4.6, the inverted sequence of child-1 is shown in child-8.

Table 4.6: Inversion.

Inversion	
Child 1	7, 1, 3, 2, 9, 4, 7
Child 8	7, 4, 9, 2, 3, 1, 7

The important thing to note about mutation is that it is crucial to find the global maximum or minimum. Without mutation, a GA may converge rather quickly to settle down around a local min/max, while the mutation element is what really allows the algorithm to explore the entire space through true global randomisation, so as to make sure that all spaces are searched.

After one cycle has evolved, we notice now we have eight offsprings/children chromosomes, from which we will perform the above algorithm repeatedly until convergence or criteria are met.

4.1.3 Adaptive GA

As described above, the GA algorithm performs numerous mathematical operations, such as the different types of crossovers, mutations and inversions. It is therefore possible to assess whether each operation would enhance the convergence at a specific stage/situation of the evolution. For instance, at the beginning stages of the population evolution, we have a large starting population, and the search for global points has just begun. At this stage, it can be beneficial to incorporate large changes, to explore wider ranges of grounds in order to get a taste of the landscape. Therefore, one could artificially increase the rates of "bigger" operations, such as crossovers and inversions, which involve the modification of large sections of the chromosomes. Towards the later stages of evolution, when the global search has stabilised in a few areas, we can then "encourage" minor modification while disincentivising larger operations. This is achieved through increasing the rate of operations such as mutation, where small amounts of the chromosomes are changed each time.

In the implementation process, one can adjust the rate of each operation by specifying the possibility of the operation at a specific stage of the evolution. For instance, a larger crossover possibility at the beginning stages and a larger mutation possibility at the later stages. The possibilities of operation can be a function of different assessment criteria: for example, the most straightforward, although not the most efficient way to assess the evolution stage is to specify a generation/iteration number and then conditioning the possibility values on the generation/iteration number. Another way to determine the evolution situation would be to assess the convergence rate: when the convergence rate/slope is high (meaning the cost function is steeply decreasing), then assign a high crossover possibility, while a high mutation possibility is assigned when the convergence rate is flatter.

4.2 Gerchberg-Saxton

The GS algorithm was introduced by R. W. Gerchberg and W. O. Saxton in 1972[25]. The proposed algorithm provided an iterative method that would allow one to retrieve the EM wave's phase information, given that the EM wave's intensities at the imaging and diffraction planes are known.

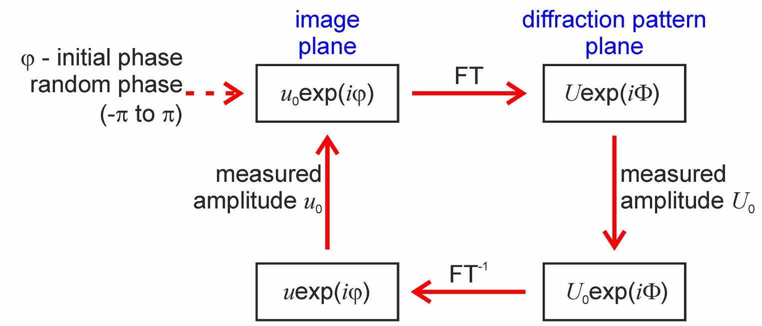

Figure 4.2: An illustrated working order of the GS algorithm[15].

The procedures of the GS algorithm are illustrated in fig. 4.2. The algorithm requires two sets of inputs: the intensity at the image plane and the intensity at the diffraction plane. However, in many cases, if the phase information is known at one of the planes, the intensity information can be retrieved by the Fourier transform. The algorithm begins with a random distribution of phases, which will be used as the initial guess for the solution. The guess phase is then combined with the known image intensities and formed as the input to a Fourier transform that brings the product to the diffraction plane. At the newly arrived diffraction plane, one then extracts only the phase information that is generated from the Fourier transform, and then combines this extracted phase with the known diffraction plane intensity. Next, the inverse Fourier transform is performed for the diffraction plane intensity and phase to get back to the image plane, where again, only the phase information is retained. This iteration then continues until the stopping criterion is reached. In the paper[25], there is a detailed proof of why the algorithm reduces the errors as the iterations progress.

Chapter 5

Summary

In Part-II of the thesis, the theoretical background that is required to carry out the research is introduced. There are two chapters in this part: "Electromagnetism" and "Optimisation Techniques".

In "Electromagnetism", there are two sections: "Antennas" and "Scattering Theories". The section on antenna theories is fundamental to understanding and characterising the performance of reflectarrays and metasurfaces in general. These range from EM propagation theories (Maxwell's equations) to specific antenna characterisation parameters (directivity, beamwidth, etcetera). This section includes content about phased arrays and their working principles; this is crucial to understanding reflectarrays, as the two are very similar in terms of the fundamental physical mechanisms, with differences in the method of excitation. The section on scattering theories lay the basis for understanding abrupt phase change and reconfigurability of the reflectarray; it also introduced concepts that will be crucial in understanding the polarisation-converting reflectarray designs.

In the chapter on "Optimisation Techniques", the GA and the GS algorithms are introduced in two separate sections, "Genetic Algorithm", and "Gerchberg-Saxton". These are the two algorithms that the author has implemented for reflectarray phase retrieval and pattern synthesis. The outline and procedure for the GA are described, as well as for the modification to an adaptive version of the GA. An introduction to the original GS algorithm utilising the Fourier transform pairs is presented in this chapter.

Part III

Literature Review

Chapter 6

Review of the State-of-the-Arts

6.1 Phased Arrays

A phased array antenna is an array or collection of distributed antennas, organised and operated in a fashion that allows the overall radiated field to be controlled to achieve desirable outcomes (beamforming, beamsteering). Among the array of antennas, a phase delay is progressively introduced, allowing for the fields to constructively or destructively interfere at the desired farfield location. The working principle of the phased array is based on Huygens' principle, which is detailed in chapter-III.

Most traditional phased arrays use analogue phase shifters to achieve desired farfield pattern[84, 2, 23]. The way it works is that transceivers use one analogue-to-digital and digital-to-analogue converter to convert the transmitted/received signal. For transmission, the digital signal gets converted into one analogue signal that will propagate to all the individual antenna elements on the phased array; however, having the signal delayed in some of the elements through the control of phase shifters that are attached to each antenna element.

Though its simplicity in device design, analogue beamforming can be technically challenging and expensive when it comes to higher frequencies, such as the THz regime, due to the difficulties associated with achieving high-frequency phase shifters. Therefore, alternative means of achieving phase shift effects are usually adopted with higher frequency phase shifters.

In digital beamforming[70, 26, 82], the phase shift is not controlled by phase shifter components that are installed physically, as in the case with analogue beamforming, but rather implemented through the digital circuity. In comparison to analogue beamforming, although digital beamforming solves the issues with high-frequency phase shifters, it is however very power-consuming due to the high demands from its processors. Thus, for high-frequency applications that require a large number of antenna elements, this can be costly and impractical.

In hybrid beamforming[21, 22, 60], as the name suggests, analogue and digital beamforming are combined. Hybrid beamforming consists of physical phase shifter components, just as in analogue beamforming; however, the individual antenna elements are arranged into subgroups, so that only one digital-to-analogue converter is needed for each subgroup. The digital precoder at the transmission part then performs the calculation needed for each subgroup, rather than for all the antennas in the case of digital beamforming. Thus hybrid beamforming has the advantage of consuming less power than digital beamformers and costing less than traditional analogue beamformers.

In Naser Ojaroudiparchin et al.'s paper[58], a phased array for 5G mobile terminals has been proposed and tested. Specifically, the paper introduced the Vivaldi antenna as the model for each individual antenna. Vivaldi antennas have long been studied and utilised in diverse fields; they have the advantages of being broadband, convenient and low cost to manufacture and impedance match.

The designed Vivaldi phased array antenna can achieve 12 dB gain at 28 GHz and has an S11 of less than 10 dB in the operational frequency range of 27.4 GHz - 28.6 GHz, which gives more than 1 GHz of bandwidth. For the scanning range from 0 to 40 degrees, the phased array can maintain the 12 dB gain.

In one paper[9], it is shown that a 5G downlink base station needs 256 antenna elements to establish a 200-meter link with 800 MHz bandwidth, in order to overcome the 156 dB path loss. Since free space path loss is inversely proportional to frequency squared, for 6G systems, similar link budgets would reach antenna counts on the scale of 100,000, thus creating many practical challenges. The purpose of this PhD is to study the means by which wireless communication at high-frequency regimes can be alleviated, either through direct substitution of newer technologies that can offer better performance, or through a combination of intermediate solutions, such as relays that can alleviate the requirements on phased arrays.

6.2 Reflectarrays

Similar to a phased array antenna, the reflectarray antenna is also composed of an array of antennas; however, in a phased array, each antenna element is actively fed with power and delay to produce radiation at specific phases, whereas in a reflectarray, the antenna elements are usually passive (also knows as parasitic) or semi-passive (in the case of reconfigurable reflectarray).

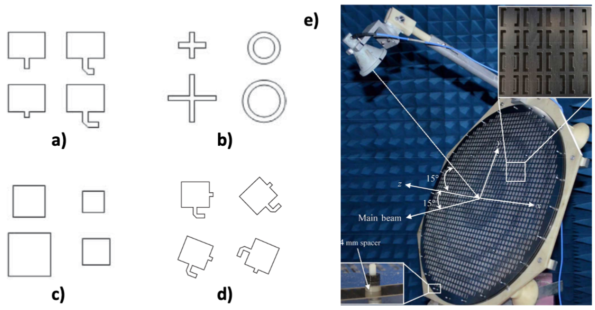

Figure 6.1: a)-d): Means by which a reflectarray can acquire phase shift in individual elements: a) patch antennas with variable feedline lengths b) and c) variable size element antennas d) orientational difference for circularly polarised incident light[34], e) A high-gain (33.9 dBi), passive, all-metal reflectarray operating at 12.5 GHz[19].

There are a few ways that a reflectarray antenna can achieve phase shift in an individual antenna element; these are shown in fig. 6.1. The main principle is to utilise the variation in antenna (or feedline) dimensions to cause a drive or drag in the excitation current or difference scattering impedance, which results in a shift in the resonance frequency of the antenna; this resonance shift then corresponds to a variation in the phase response of the reflected EM wave, hence achieving the desired beam functionalities, such as beam-steering/beamforming.

Mechanical devices[54, 40] utilize micro-electrical-mechanical systems (MEMEs) to physically vary the dimensions and hence the electrical properties of the devices. Mechanical micromotors can be tailored to achieve high performance and accuracy, but these devices often suffer from high costs (owing to the manufacturing of MEMEs) and relatively low reliability when compared to electrically controlled metasurfaces.

6.2.1 PIN diode-based

Reconfigurability is usually not associated with reflectarray until more recent years, as the dimensions in traditional reflectarrays are usually fixed. This is overcome with the introduction of PIN diodes[18, 80, 75]. PIN diodes act as a switch that connects two otherwise separated electric circuits. Upon completion of the circuit (when the PIN diode is in the ON mode), the two circuits become connected, and the patch antenna becomes electrically larger. When the circuit is disconnected (PIN diode in the OFF mode), then the effective electrical circuit becomes smaller, as the two metallic parts of the patch antenna are not connected. This difference in the effective electrical properties of the patch antenna, which is controlled by the operational status of the PIN diode, gives rise to a reconfigurable response of the reflected EM waves.

The recently proposed and developed metasurfaces[75, 80] consist of a periodic arrangement of millimetre-scale copper plate antennas with PIN diodes. Each PIN diode is fed individually by a DC current, which can either be forward or reverse-biased, resulting in either an open circuit or closed circuit. The open circuit (forward-biased) and closed circuit (reverse-biased) are equivalent to two different dimensions of antennas, which, as discussed above, result in different phases in the transmitted EM wave.

For certain symmetric and trivial patterns of ON and OFF, such as that of checkerboard set-up, the reflectarray metasurface will split the incident beam into four outgoing ones, each pointing roughly 90 degrees (in azimuth) away from another. A 2-beam splitting is simulated by the strip pattern of ON and OFFs, proving the beam-splitting functionality of the device in simulation.

Going further in-depth, another paper[80] proposed a very similar reconfigurable metasurface using the PIN diode principle and patch antennas; however, in this case, the authors have gone further by using a machine learning algorithm (adaptive GA) to arrive at the combinations of ON and OFF's to achieve specific beam functionality. The farfield results in this paper were obtained by having a point source that is 20 degrees off the centre axis perpendicular to the metasurface. It is important to note that trivial functionalities such as multibeam have a nontrivial pattern of ON and OFF combinations. This is due to the nature of a complex inverse problem between the farfield and the nearfield, which will be further analysed in chapter-IV.

The researchers in [75, 80] have all used a binary state (1-bit) control device; this has the best simplicity and achieves sufficient performance. Nonetheless, a greater degree of control freedom can always improve the performance of the metasurface. A detailed analysis of this scalability issue is presented in chapter-IV. In [30], the researchers have designed a 2-bit device, having two diodes connecting to a patch antenna, giving a greater degree of freedom on the control of the effective electrical dimensions, and hence on the phase/amplitude response of the device.

In a more recent paper published in 2021[87], a double-layer PIN diode-based reflectarray for Ku-band operation is proposed. The unit cell consists of two resonant layers, substrates, and a ground plane. The middle resonant layer is a slotted square patch, and the top resonant layer is a regular patch antenna. The PIN diode is connected through two biasing lines; the two states of the PIN diode give rise to two different resonant characteristics, which in this case are two different reflection phases. Additionally, the unit cell here includes a radial stub to filter the DC from the RF signal. This proposed dual-layer design has the advantage of a greater bandwidth (22% of 1 dB gain and 25% of maximum aperture efficiency). Additionally, this unit cell design achieves the required 180° reflection phase difference between the ON and the OFF states of the PIN diode.

A recent paper published in 2021 from Chongqing University[76] also introduced a two-layer design that consists of a Jerusalem cross-ring layer and a Malta cross layer. The Jerusalem cross-ring is connected with four PIN diodes; these diodes operate in two collective modes, which enable the excitation to give rise to two polarisations. There are two other diodes in the Malta cross, which creates a current-reversal effect in the ON and OFF states, giving rise to a 180° reflection phase difference. This device has demonstrated the ability to not only be reconfigurable in terms of beam-scanning angles, but also in terms of polarisation control.

6.2.2 Liquid Crystal-based

Using LC is another way to achieve DC bias-controlled reconfigurability[35, 7, 65, 36]. LCs that are in the nematic phase, which consist of thread-like molecules, possess an anisotropic dielectric property. The anisotropy comes from the molecular realignments to an applied bias voltage, causing a permittivity variation $\Delta\varepsilon_r$ between the ON and OFF states. Similar to how diodes change the antenna resonance frequency via varying the effective electrical dimensions, LC changes the resonance frequency via a variation in the substrate permittivity, hence resulting in a drive or lag in the antenna response, giving rise to the phase difference in the reflected signal.

In W. Hu et al.'s paper[28], a 10 GHz, 12x12 element monopulse reconfigurable reflectarray is developed. The device is split into two halves, with 6x12 passive antenna elements and 6x12 voltage-controlled elements. All the antennas have been designed with variable sizes, in a way that the required phase variation range from DC bias can be lowered to 90 degrees (rather than the minimum of 180 degrees, in a binary device). The device is working only in two DC bias modes: sum mode and difference mode. The intention of this device is for radar tracking. While this device is structurally simple and practical for manufacturing, it is limited to only two modes of operation, and thus making it unsuitable for other wireless communication applications other than radar detection. In the following sources, devices with a greater degree of control freedom are shown.

LC unit elements can be more suitable for high-frequency applications, as compared to diodes, which usually exhibit higher losses at high-frequencies due to their intrinsic parasitic losses. One of the earlier papers published in 2011[7] showed a design, fabrication and testing of a 16 by 16 element LC reconfigurable reflectarray operating at 77 GHz. In this paper, the unit cell antenna is chosen to be a “3-finger” type connected patch antenna, as they found that compared to the square patch antenna, this new topology would give rise to a higher phase difference between the ON and OFF states (563 degrees as compared to 277 degrees in case of the square patch).

In terms of the pattern synthesis, the paper has indicated that Particle Swarm Optimisation (PSO) is used without enclosing details of the optimisation details. However, the simulated farfield patterns were closely matched to those measured. This reflectarray showed the ability for a max scanning angle of ± 20 degrees.

In papers published later by a different group[65, 62, 63, 64], a very similar element antenna design of “3-finger” patch is studied at the operational frequency of 100 GHz, and a subsequent LC-based reflectarray is developed for SATCOM applications, claiming electrical performances of 19.6 dBi gain, 60 degrees scan range and side lobe levels of less than -13 dB. However, one of the problems is the low efficiency, which is around 20%, and similarly to the study in [7], the beamsteering demonstrated is only one-dimensional. This is due to the nature of the electrical wiring/addressing technique: the LC antenna elements were wired with a line-by-line addressing technique, which is common in LCD displays. This technique, however, forbids the control of a specific unit cell, as the concept of the threshold voltage is invalid when the LC is responding to any voltage change with a reflection phase change.

In the studies by Palomino et al.[65, 62, 63, 64], the researchers have developed an accurate model that takes into account the inhomogeneity and anisotropy that are present in LC molecules. This is crucial as it provides a much better picture of the frequency and voltage response of LC, which will enable more accurate theoretical models that use LC as a substrate base for resonant analysis.

More recently, LC-based technologies have started to become visible in commercial applications. Companies such as Alcan Systems and Kymeta have begun utilising LC-based components in their phased arrays[49]. A joint collaboration between the Technical University of Darmstadt and Alcan Systems has brought forward some of the most modern applications of LC-based components in phased arrays[33], which were in the areas of SATCOM and 5G millimetre-wave systems. In their papers[33, 49], two main types of LC-based shifters were introduced: firstly, a waveguide phase shifter that is capable of $5.1°/s$ to $45.4°/s$ phase change rates (depending on the applied voltages); secondly, a planar delay-line phase shifter that is capable of achieving beam scanning ranges of $-60°$ to $60°$ within 10 ms.

For the waveguide phase shifter, a rectangular waveguide is filled with LC, and the top and bottom of the waveguide are inserted with biasing electrodes. The electrodes induce biasing voltage, which can control the permittivity of the LC. In this way, since the LC substrate’s permittivity can be tuned, the effective electrical length of the waveguide can thus also be tuned accordingly. As a result, one can achieve phase control just by controlling the voltage bias. This method has a lower phase change response time since the thickness of the waveguide is around $50\mu m$.

For the planar phase shifter, a tunable coupled line filled with LC is implemented. The coupled line consists of periodically stacked microstrip lines with overlapping areas filled by LC. The overlapping area function as an LC-based varactor, where the capacitance can be controlled via voltage bias: therefore, the microstrip line's phase can be controlled by varying the voltage bias. This technology has the benefit of low latency control, as the spacing between the top and bottom microstrip lines are less than 5μm, so quick switch rates of less than 35 ms can be obtained.

In our research, we have decided to combine the advantage of a fully reconfigurable (DC-biasing each individual antenna element) set-up, with the practicality of a two-state/binary DC control. In this way, we can obtain a high degree of freedom with the achievable beam functionalities while preserving the practicality of a simpler biasing circuit.

6.3 Transmitarrays

Transmitarrays[69, 42, 43], as the name suggests, function in the transmit mode. Rather than having a ground plane that functions as a mirror reflecting the incoming radiation, transmit arrays allow the radiation to pass through with as little attenuation as possible while modifying the optical responses accordingly (phase/amplitude). Their primary advantage over the reflectarrays is that the feed source does not block the emission; in reflectarrays, feed sources will always be blocking some part of the reflected re-emission, even in an offset feed source set-up. This could greatly simplify the design of transmitarrays with integrated feed sources and improve the overall farfield radiation performance. The disadvantages of transmitarrays tend to be the aperture efficiency and layering requirements. Transmitarrays tend to have lower efficiencies per resonance layer, when it comes to optical manipulation. Without the ground plane, a transmitarray often needs multiple resonant layers to achieve the required phase/amplitude manipulation. This often makes the design and fabrication more complicated (and costly) when compared to the reflectarray counterparts that are operating at the same frequency, and the efficiency is often reduced due to the multi-layer nature.

In a 2017 paper by Joao R. Reis et al.[67], a reconfigurable transmitarray operating at 5.2 GHz has been shown to be capable of azimuth steering of 28 degrees and elevation steering of 26 degrees, with 1 degree of angular resolution. The prototype of the device is demonstrated on a 5x5 element structure. The unit cell is inspired by a frequency-selective-surface (FSS) design[56, 74, 24]; it is essentially a metal ring with an inner cut-out patch that is connected to the ring via two varactor diodes. The varactor diodes act as capacitors when reverse-biased, thus changing the electrical size and properties of the unit cell, as compared to when forward-biased.

The stacked copper ring unit cell proposed in the paper[67] is made of five layers, and with one layer, it is only able to achieve a maximum of 80 degrees transmission phase difference when maximally biased, whereas with five layers, the device is capable of a maximum of almost 480 degrees transmission phase difference. At the frequency of 5.35 GHz, it is also where the transmission amplitude is at its maximum.

In Antonio Clemente et al.'s paper[13], a 1-bit reconfigurable transmitarray operating in the X-band is proposed and tested. The two binary states offer a phase change of 180 degrees for the transmitted wave. The device can achieve a gain of 5 dBi at 9.75 GHz and has a 14.7% 3-dB bandwidth. The unit cell is shown in fig. [13] a): it consists of a passive U-shaped patch at the bottom and an active O-shaped diode-connected patch at the top. The diodes at the top patch are oriented in opposite directions; thus, one diode will always be in short under bias, making an effective and analogous U-shape that is either in phase or out of phase with respect to the passive U-shaped patch at the bottom. The diode configuration thus determines whether the transmitted wave is 0 or 180 degrees out of phase with respect to the incoming radiation.

A research group at the institute of CSIC in China has recently designed a terahertz transmitarray that operates at 340 GHz[41]. In their research, they have designed a dual-layer LC enclosure set-up, with multiple resonators. Each of the two LC layers can be individually voltage biased, to achieve a permittivity variation, which then gives rise to a resonant characteristic variation of the resonators; this results in the control of the transmitted wave's phase. This design has shown impressive performances: a transmission value of greater than 80%, and a beam-steering range of $\pm 40°$. Often, reconfigurable transmitarrays suffer from low transmission efficiencies, due to the multi-layer resonant design that is required to achieve sufficient phase change: this design, however, demonstrated sufficient phase control for 1-bit reconfigurability (180°) and high transmission coefficient. Although this paper is purely theoretical and fully based on simulations, so it is still to be verified whether in practice such high performances can be obtained.

A group from the University of Grenoble Alpes in France has recently published their design, simulation analysis, and proof-of-concept construction of a Ka-band transmitarray[47]. Their design proved to have a 60° beam-steering range and a low broadside axial ratio of lower than 1 dB. It is also able to achieve almost 26 dBi gain at broadside angle. However, as with transmitarrays in general, the aperture efficiency is only 19.2%. In this design, the 180° reflection phase delay needed for beam-steering is achieved by a current swapping effect on the bottom resonator that is connected to a pair of PIN diodes. The circular polarisation control comes from the PIN diode-connected resonator at the top. For the top resonator, a 90° delay line is connected via a PIN diode pair: the ON and OFF states of the PIN diodes will control the reflection phase to be 0° or 90° for the specific electric field component, hence achieving control on the circular polarisation.

6.4 Metasurfaces

While the term metasurface can broadly incorporate the aforementioned devices, such as the transmitarray and reflectarrays, as sub-wavelength engineering (the sub-wavelength unit cells) is required to achieve macroscopic effects (e.g., wavefront manipulation), this section will present some newer technologies that succeed the concepts of array antennas.

6.4.1 Non-Geometric Phase

6.4.1.1 All Dielectric

Traditional lenses are designed such that waves would gradually accumulate phase and amplitude over a distance that is much greater than the wavelength. Metalens/metamirror is a type of metasurface that focuses on introducing abrupt phase/amplitude variation to the incident EM radiation, at a distance on the scale of wavelength, either by the geometric phase (otherwise known as the Pancharatnam-Berry phase) or resonant phase retardation[55, 77, 85, 4, 27]. Much focus has been put on the geometric phase control of EM waves; however, it requires that the incident wave be circularly polarised, and hence often is commercially difficult and impractical to achieve. Although the full 2π phase difference, which is essential to the full control of the wavefront, is achieved with the introduction of the geometric phase, it is nonetheless rather energy-inefficient.

One paper introduced a computational study on an all-dielectric metamirror for application in THz transmission[44]. It showed the ability to control the amplitude and phase of the linearly polarised incident light and exhibited a few designed beam patterns, such as the vortex and the Bessel beam.

It is given by Mie theory that the scattered field may be expressed in terms of the superposition of one or more fundamental modes, namely electric and magnetic modes (dipole modes for the strongest influence). With traditional metallic antennas, the magnetic dipole mode is usually not excited or very poorly excited, whereas, in the paper's case, there is a strong presence of magnetic dipole mode. In [44], the author has shown that the presence of a high normalised scattering cross-section is an indication of the strong coupling between the dielectric resonator and the incident wave, where we can observe two electric peaks that correspond to the electric and magnetic dipole modes. The magnetic mode is also shown in [44], where a central magnetic field is accompanied by a circular electric field; the electric dipole mode is shown next to the magnetic one.

The electric and magnetic modes are of importance because the full 2π phase shift is achieved only when one can bring together these dipole resonances at the proximity frequencies, which is achieved through designing the geometries of the resonator and periodicity. When only one mode is excited, radiation from the resonator is out of phase with the incident field, creating destructive interferences and reflection peaks. When an EM wave is reflected off of a perfect electric conductor, the boundary conditions give rise to a π phase shift in the reflected wave. By tuning the metasurface so that the magnetic dipole mode is also in resonance, the π phase shift from the electric dipole mode can be compensated and hence a perfectly in-phase wave in the transmission/reflection mode can be achieved. This is of more interest to THz sensing, as when only one mode is excited, the out-of-phase nature creates destructive interference at the surface, whereas when both modes are excited, the fields are enhanced at the surface.

By designing the geometries of the resonators, the author is able to show that full $360°$ phase variation is possible. This is shown in [44], demonstrating the phase and amplitude responses when the spatial dimensions of the resonators are varied. As a result, many beam functionalities, such as the Bessel beam, can be achieved through the proper design of an overall structure according to the specific phase profile. The author claimed that, to the best of their knowledge, this is the first all-dielectric metasurface operating in the reflection mode and indicated a reflection efficiency of more than 0.9.

6.4.1.2 Plasmonic

A common way to achieve abrupt phase difference is through resonant phase retardation effects, in this case[83] a plasmonic resonance. Given that the incident wave is polarised 45 degrees with respect to both $\hat{s}$ and $\hat{a}$, both the symmetric and antisymmetric modes will be excited. Because of the dual-modal property of this plasmonic antenna, the paper's author is able to manipulate amplitude and phase change through adjustments in the antenna geometry (h and δ) that go from one mode to the other mode, which proved that a full 2π phase control is possible. The relation between the unit cell rod's spatial parameters (h for rod length, and Δ for the enclosed angle between the two rods) and reflection phase/amplitude is shown in [83].

Through the proper design and arrangements of the antenna elements, different metasurfaces were fabricated with gold plasmonic antennas on a silicon wafer, and diverse beam functionalities such as Gaussian beam, vortex beam and Bessel beam were achieved in experiments. In fig. **??** b), one can observe the achievable reflection and refraction angles of the device when compared to an ordinarily reflecting/refracting material.

6.4.2 Geometric Phase

The term "geometric phase" comes from the theory of classical and quantum mechanics; it is the phase that is acquired through the course of a cycle. Specifically to metasurfaces, this can be the case with circularly polarised light passing through birefringent materials; an additional phase difference will arise from any rotational operations, due to the different effective refractive indices that cause the orthogonal components of light to move at different speeds. Many modern metasurfaces utilise this to achieve novel wave manipulations[46, 10, 45].

The group at Harvard has recently shown that with silicon nano fins, they could achieve achromatic focusing ability in the visible light spectrum[11]. The achromatism perhaps is not the most exciting element to the wireless communication field, given that the paper suggests the relative group delay and group delay dispersion (contributors to achromatism) on the order of femtoseconds and low latency requirements of most modern/near-future applications would be satisfied with millisecond delay, it is nonetheless crucial to the imaging field. What is of more interest to the wireless communication field would be the way the relative phase profile is formed with silicon nano fins, resulting in a flat lens with a thickness of less than half of the wavelength.

Firstly, to be able to achieve a focusing effect from a planar surface, one must have the following phase profile:

$$\phi(r, \omega) = -\frac{\omega}{c}(\sqrt{r^2 + F^2} - F) \tag{6.1}$$

where F, r, c, ω are the focal length, radial coordinate, speed of light and angular frequency.

It is important to know that the geometric phase associated with the angular orientation of the unit structure can be expressed in Jones matrix form:

$$\frac{t_L + t_S}{2}\begin{bmatrix}1\\i\end{bmatrix} + \frac{t_L + t_S}{2}e^{i2\alpha}\begin{bmatrix}1\\-i\end{bmatrix} \tag{6.2}$$

where the t_L, t_S and α are the complex transmission coefficient (when the polarisation of the incident wave is along the long and short axis of the nano fin) and angle of orientation. Notably, when the orientation of changed, an induced phase shift term $e^{i2\alpha}$ is directly caused. This phase shift, coupled with the short and long-axis from the double resonator unit cell design, allows light to acquire different phase values given the different resonant frequencies and therefore permits one to freely design the phase of the reflected/transmitted light, via the adjustment of the unit cell rotation angle.

Although, for the optical purpose of the above paper, the metalens is designed for short-distance focal length ($63\mu m$), it nonetheless remains the freedom of the inventor to choose suitable phase profiles with corresponding focal lengths and design the metalens accordingly.

6.4.3 Photoconductivity and Reconfigurable Fresnel Zone Plate Antennas

Photosensitive semiconductors can be used in optically-driven reconfigurable antennas. Certain semiconductors, when excited by light of the right energy, will enable the excitation of electron-hole pairs, hence changing the material properties such as the conductivity and permittivity, which are related quantities: $\varepsilon = \varepsilon_r \varepsilon_0 + j\frac{\sigma}{\omega}$. Rather than focusing on resonators, lenses are made with photosensitive materials and consequently photo-driven to achieve a similar effect to that of Fresnel zone plates (FZP), which rely more on diffraction and interference, rather than refraction and reflection as with the traditional lensing.

Traditionally, FZPs have been manufactured by mechanical means to shape the concentric circles, which inevitably limits the flexibility of each FZP, meaning that the physical structure of each FZP is unable to be freely or easily changed. With photosensitive material, one can essentially freely choose the pattern of FZP by photo-inducing the photosensitive material in that specific pattern, hence increasing the carrier density there, which is related directly to the material's refractive index and coefficient of extinction through $\tilde{\eta} = n + i\kappa$, and therefore losses/blockages associated with propagating waves. In short, one can shine lights on appropriate photosensitive material in the pattern of FZP and achieve the same effect as that of physically constructing an FZP through mechanical means of blockages.

In terms of efficiency, it has been shown that a relatively low level of optical power can induce a significant change in the high-resistive Silicon's photoconductivity, which makes Si-based photoconductive switches a prevalent choice for optically driven devices such as optical phase shifters for antenna arrays.

Another benefit of using optically driven elements in an antenna array system is the reduction in radiation interference. The conventional antenna arrays will use electronically controlled phase shifters for each antenna element, which will inevitably contribute to the unwanted radiation from the current supplied. On the other hand, an optically driven phase shifter will be intrinsically separated from the radiation field of the antenna array, thereby reducing unwanted interference.

Chapter 7

Summary

In Part-III, the author presented an overview of the state-of-the-art researches in reflectarray and metasurfaces. There is one chapter, "Review of the State-of-the-Arts", and there are four sections within this chapter: "Phased Arrays", "Reflectarrays", "Transmitarrays", and "Metasurfaces".

In "Phased Arrays", "Transmitarrays", and "Metasurfaces", the author introduced some of the modern researches and developments in these technologies. Hybrid, digital, and analogue phased arrays are introduced in theses sections. Two state-of-the-art transmit arrays that utilise PIN diodes to achieve reconfigurability are shown here. Metasurfaces that utilise geometric phase mechanism, plasmonic excitation and Mie resonance, as well as photoconductive materials are introduced here.

In "Reflectarrays", the author has dedicated the majority of the content. This section is split into two sub-sections: "PIN diode-based" and "LC-based". The author has compiled numerous state-of-the-art researches from varied groups who have researched and prototyped lumped element-based and LC-based reflectarrays. These reflectarrays are usually operational in the sub-100 GHz bands and not individually biased. The author has listed both the advantages and challenges faced by these state-of-the-art devices.

Part IV

Research Results and Publications

Chapter 8

Liquid Crystal Reconfigurable Reflectarray

In this chapter, a lot of the contents come from my own publications[52, 50, 51, 78]. In order to avoid citations appearing everywhere and hindering the readers' experience, I will put the citations here for the entire chapter.

The principle idea of a reconfigurable reflectarray metasurface is to be able to control the amplitude and/or phase of the reflected wave. In the case of an LC-based reflectarray metasurface, the LC material is the underlying tunable material, which has its properties altered through applied voltage. The variation of the LC properties then results in a variation of the reflected EM wave's phase/amplitude, which will achieve the desired EM result in the farfield, if configured properly.

8.1 Liquid Crystal

LCs that are in the nematic phase, which consist of thread-like molecules, possess an anisotropic dielectric property. The anisotropy comes from the molecular realignments to an applied bias voltage, causing a permittivity variation $\Delta\varepsilon_r$ between ON and OFF states. It is the $\Delta\varepsilon_r$ that causes a resonance variation between the ON and OFF states of our unit cell, which is analogous to a drive or lag in the antenna response, giving rise to the phase difference in the reflected signal. This reconfigurable property is illustrated in fig. 8.1.

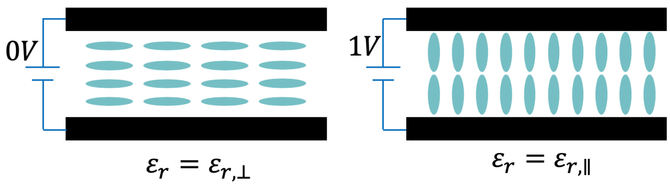

Figure 8.1: Molecular alignment of the LC in nematic state. When under applied voltage, they exhibit dielectric response on the molecular level, which modifies the parallel/perpendicular component of the permittivity compared to not under an electric field.

8.1.1 Liquid Crystal Inhomogeneity, Anisotropy and Effective Permittivity

In this subsection, we refer to the work of Palomino et al.[65, 62] and adapt their result of the effective LC permittivity under the application of biasing voltage. LC molecules exhibit innate inhomogeneity and anisotropy (in their electric permittivity tensor) due to the unique symmetries and distribution of the molecules. The precise modelling of how inhomogeneity and anisotropy will allow a more accurate prediction of the LC electric permittivity values under applied biasing voltages.

Because of the inhomogeneity and anisotropy nature of LC, and the effects of forces torsional forces (between the LC and the metal plates and among LC molecules themselves), the angular orientation of LC molecules under an applied biasing voltage is non-linear, as shown in the work of Palomino et al. in fig. 8.2.

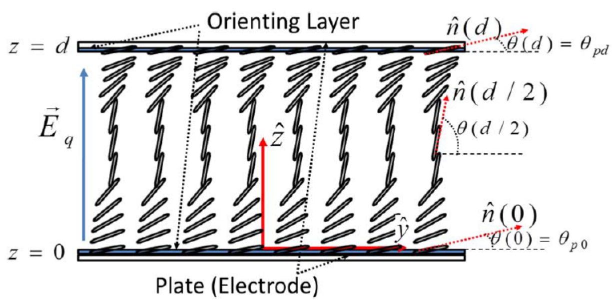

Figure 8.2: The angular orientation of the LC molecules under a biasing voltage applied between the top and bottom plates[65].

In fig. 8.3, Palomino et al. have shown the effect of LC molecular orientation (θ) on the reflection phase. The θ_a and θ_{eff} are two methods of obtaining the tilt angle (average tilt angle at a given voltage, and the tilt angle from an effective stratified medium). There is a significant difference between the reflection phases from different molecular tilt angles, and given the torsional alignments of the LC molecules, this effect will be factored into the theoretical modelling of the LC permittivity.

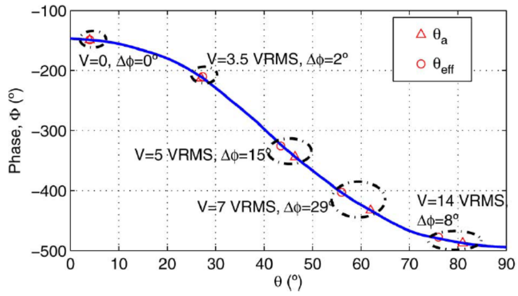

Figure 8.3: The relation between LC molecular tilt angle θ and reflection phase[65].

As a result of the precise modelling of the LC molecules under applied voltages, Palomino et al. were able to demonstrate very accurate results (as compared to measured values) on their reflection phase under different biasing voltages, which is shown in fig. 8.4. For our research, we will adapt the results Palomino et al. obtained on the effective permittivity given applied voltages at 108 GHz.

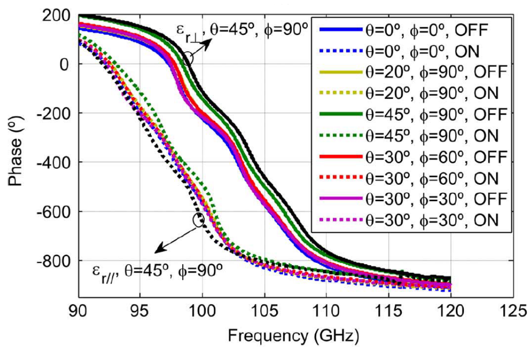

Figure 8.4: The reflection phase and frequency, given different biasing voltages[62].

The exact values of the effective permittivities under the ON (ε_{ON}) and OFF (ε_{ON}) states of the biasing voltage are listed in table. 8.1.

ε_{ON}	ε_{OFF}	$\tan\delta_{ON}$	$\tan\delta_{OFF}$
3.1	2.53	0.012	0.018

Table 8.1: LC ON/OFF permittivities.

8.2 Problem Setup and Formulations

8.2.1 LC Permittivity

The design of patch antenna dimensions is dependent on the permittivity of the substrate, which in our case is the LC. Numerous sources[20, 79, 53, 1] have provided this data in the sub-THz regime and a few in THz (summarised in table. 8.2), from which we noticed the independence of ε_r to frequency (19-165 GHz band) of the type GT3-23001. In addition, the operating temperature of gt3-23001 LC[66] is as wide as -20 to 100 °C, making it ideal for outdoor applications. Hence we have selected to adapt the GT3-23001 LC, which is commercially available from Merk.

LC type	Frequency (GHz)	$\varepsilon_{r,\perp}$	$\varepsilon_{r,\parallel}$	ref
GT3-23001	19	2.46	3.28	[79]
BL006	35	2.62	3.04	[53]
BL006 Mixture	35	2.3	3.1	[1]
5CB	20	2.2	2.7	[1]
BL037	140-165	2.65	3.25	[20]
GT3-23001	140-165	2.47	3.25	[20]

Table 8.2: LC models and corresponding permittivities.

8.2.2 Unit Cell

The EM simulation carried out in this work uses CST software, which solves the Maxwell's equations with the Finite Integral Technique (FIT) and Finite Difference Time Domain (FDTD) method; specifically, we have used the Transient and Frequency Domain solvers for our problem.

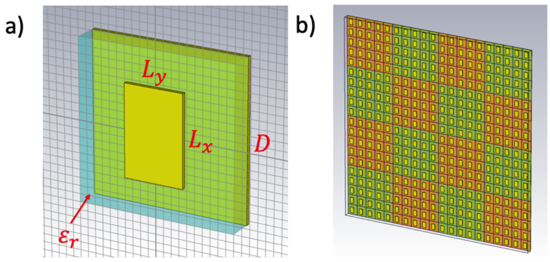

Figure 8.5: a) Unit cell of the LC patch antenna. Periodicity $D = 2mm$, patch dimensions $L_x = 1.134mm$ and $L_y = 0.747mm$, substrate permittivity modelled as $\varepsilon_r = 2$ in OFF state, $\varepsilon_r = 4$ in ON state b) supercell with ON (red) and OFF (green) in checkerboard configuration

In setting up our problem, we have designed the dimensions of our patch antenna (refer to fig. 8.5 for W and L) according to:

$$W = \frac{c}{\sqrt{\frac{\varepsilon_r+1}{2}}}; \quad L = L_{eff} - 2\Delta L \tag{8.1}$$

where the effective permittivity ε_r, effective lengths L_{eff}, and extension length ΔL are given by:

$$\varepsilon_{eff} = \frac{\varepsilon+1}{2} + \frac{\varepsilon-1}{2}\sqrt{1+12\frac{h}{W}}; \tag{8.2}$$

$$L_{eff} = \frac{c}{2f_0\sqrt{\varepsilon_{eff}}}; \tag{8.3}$$

$$\Delta L = 0.412h\frac{(\varepsilon_{eff}+0.3)(\frac{W}{h}+0.264)}{(\varepsilon_{eff}-0.258)(\frac{W}{h}+0.8)}; \tag{8.4}$$

The preliminary design formula will give us the unit cell depicted in fig. 8.5, where a) represents the unit cell schematics, and b) is a full device illustration, with the red-coloured unit cells representing the OFF configuration, while the green unit cells represent the ON configuration.

With the extrapolated value of biased LC, we have performed CST simulations in the frequency domain on a single unit cell structure (single patch antenna with substrate and ground plane), with applied periodic boundary conditions to simulate supercell environment. From these simulations, we can retrieve two important properties: 1) the phase difference and 2) the amplitude difference between the reflected EM wave on the unit cell when LC is in the ON state versus the OFF state.

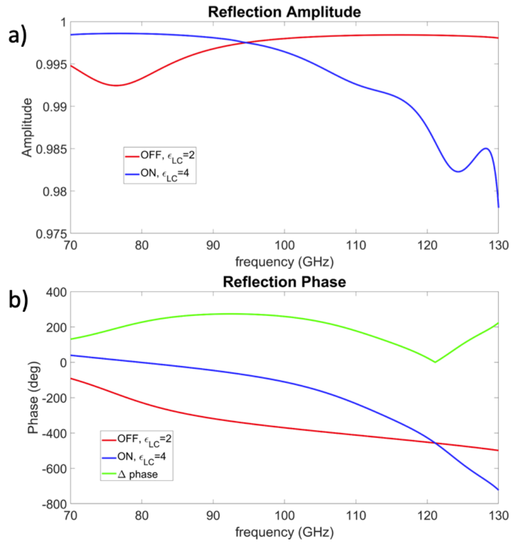

Figure 8.6: a) Ideal operating frequency at 94.6 GHz, where the reflected amplitude of ON and OFF elements are equal b)At 94.6 GHz, the equal reflection frequency for both ON/OFF states, the phase difference is at a maximum of roughly 200 degrees

The results are shown in figure. 8.6: our device achieves maximum phase difference of the reflected 94.6 GHz EM wave between the ON and OFF states of LC, and the amplitude of the reflected wave is also the same at this frequency.

In further updates, we have adopted a more accurate unit cell design that includes the voltage biasing lines and the spacers that will enclose the LC to each individual unit cell, as presented in fig. 8.7. This updated design is optimised for 108 GHz application.

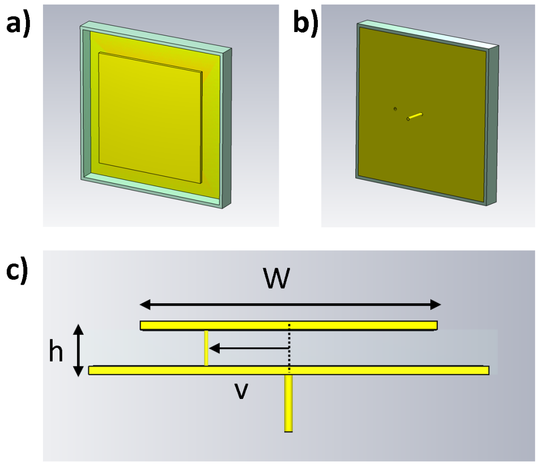

Figure 8.7: The schematics for the updated unit cell structure. LC is sandwiched between the top patch antenna and the bottom ground plane. The light green are spacers to enclose the LC in each individual unit cell. The detailed dimensions are: v=0.18mm, W=0.714mm, h=0.087mm, and the periodicity is 1mm.

Similarly here, the preliminary dimensions of the unit cell can be calculated from the fundamental antenna design formulas, given the operational frequency and periodicity (which should be sub-wavelength in order to prevent the formulation of grating lobes, but not too close as to optimise beamwidth). It is found that half-wavelength spacings are optimal in terms of having a good quality of beamwidth as well as steerability.

With the fundamental patch antenna design formulas, known operational frequency of 108 GHz, and periodicity of approximately half a wavelength, we arrive at the preliminary dimensions of the unit cell structure. The half-wavelength element spacing is chosen for an optimal compromise between the beamwidth and steerability (and avoidance of grating lobes).

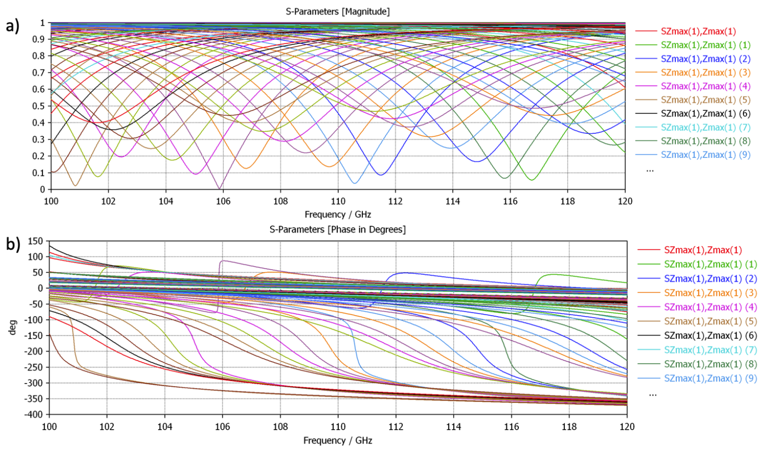

Figure 8.8: a) The unit cell reflection amplitude and b) the reflection phase retrieved from full-wave simulations.

The next step involves unit cell optimisation in frequency domain solvers, such as Studio Suite, or the more traditional method of moments (MoM). With these solvers, we can enforce periodic boundary conditions and include coupling effects, which are often significant in subwavelength-spacing resonators. The S-parameters in reconfigurable reflectarrays are defined differently when compared to traditional antenna arrays, as reflectarrays are not fed in the traditional way, but rather through a feed horn that is usually situated on top of the reflecting surface; thus, S11 here refers to the proportion of EM reflection/radiation reflecting away from the plane of the patch antenna and towards the feed source in free space.

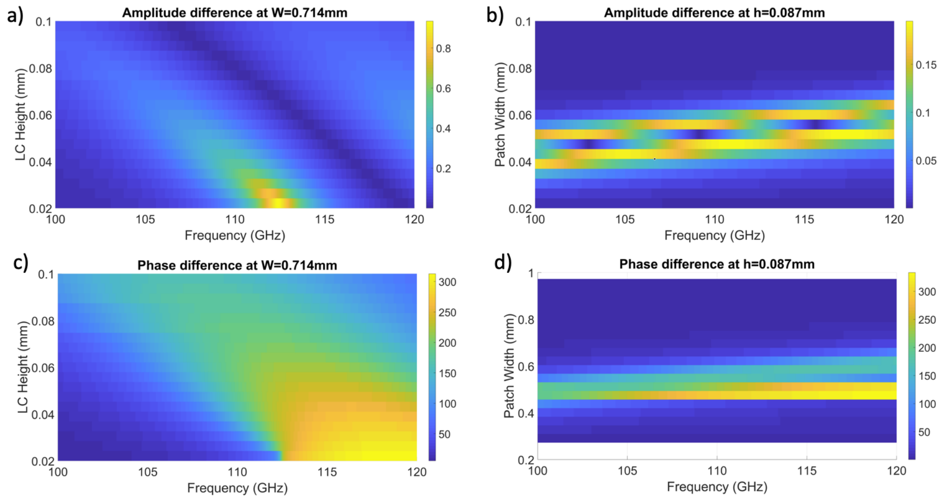

Figure 8.9: The optimisation of LC substrate height h, according to reflection phase and amplitudes in parameter space, for 2 given patch antenna widths, 0.714mm and 0.087mm. a) and c) the amplitude difference between the ON and OFF states, b) and d) the phase difference between the ON and OFF states.

The frequency-domain solver allows us to retrieve the optical responses for a given unit cell dimensions. We performed parameter sweeps for variables such as substrate height and patch length/width, with results presented in fig. 8.8.

With the results from fig. 8.8, we then exported them for post-processing to a platform such as Matlab and ran a routine in order to retrieve the optimal parameters. The routine essentially decreases the parameter space dimensions and looks for satisfactory entries in the sub-spaces. In fig. 8.9 a), the dimensional variation and optical responses are shown: we have retrieved optimal parameters given the target reflection phase of 180 degrees and amplitude difference of <0.2. Specifically, for the patch antenna width of 0.714 mm while varying the height, the routine searches for satisfactory entries with a varying LC substrate height. The search is based on the requirement that the reflection phase difference between the ON and OFF states to be close to 180 degrees, and the amplitude difference shall be minimal, while sufficiently high. Fig. 8.9 b) shows a parameter sweep with a fixed width but a varying height.

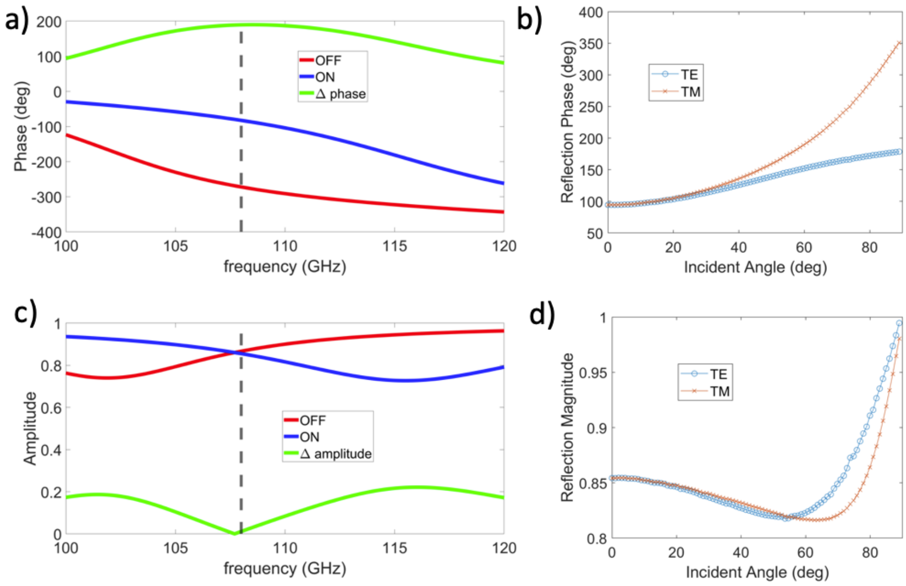

Figure 8.10: a) and c) The reflection phase and amplitude versus frequency characteristics from the unit cell, simulated with Floquet periodic conditions. b) and d) The reflection phase and amplitude versus incident angle characteristics from the unit cell, simulated with Floquet periodic conditions.

We perform a parameter sweep over structural parameters (height h and width W) and store the S11 amplitude and phase results for analysis. We can then post-process the data and retrieve optimal structural parameters, given the desired conditions, which are as follows: a reflection phase difference between the ON and OFF states of 180°; second, a maximal reflection amplitude of both states; and third, a minimal reflection amplitude difference between the two states.

In fig. 8.10 a) and c), we demonstrate that the phase difference between the ON and OFF states of the new unit cell, simulated under periodic boundary conditions, is 189° at the operational frequency of 108 GHz. The magnitude of the reflection is 0.855 for the ON state and 0.857 for the OFF state. Note that the unit cell characteristics are practically identical to our earlier works[52, 50], as the integration of the biasing line and FR-4 spacers were designed to minimise any interference with high-frequency resonances. Nonetheless, the reflection amplitudes of the ON and OFF states at 108 GHz are slightly different; thus, the difference is included in the theoretical farfield model.

In fig. 8.10 b) and d), we demonstrate the reflection phase and amplitude of the structure for oblique incident angles for both the TE and TM modes. We can see that for the reflection phase, both the TE and TM

Algorithm 1: Matlab script to optimise unit cell dimensions

Data: S11p - S11 phase; S11a - S11 amplitude; hu, hl - LC height lower/upper bound; Wl, Wu - patch antenna width lower/upper bound; pl, pu - phase difference lower/upper bound; al, au, adm - amplitude lower/upper bound and amplitude difference margin

Result: h, W - Unit cell height and width optimised for close to 180 degrees phase difference, and maximal reflection amplitude (minimal difference) of both states

initialise pu, pl, au, al;

for $h{=}hl \to hu$ **do**

  for $W{=}Wl \to Wu$ **do**

    S11P{h,W}=S11p$_{on}${h,W}-S11p$_{off}${h,W};

    S11A{h,W}=S11a$_{on}${h,W}-S11a$_{off}${h,W};

  end

end

Result ← Find (S11a ≥ al) and (S11a ≤ au) and (S11A ≤ adm) and (S11P ≥ pl) and (S11P ≤ pu);

Result = Sort Result;

h, W ← Result

---

polarisations remain relatively unchanged from 0° to 40° incidence angle, after which the reflection phase becomes significantly different (more than 20° different from the normal incidence phase), affecting the performance of the structure. Both the TE and TM modes have similar phase values until the angle of incidence reaches approximately 40°. This implies that the device can possibly be programmed to operate for both polarisations up to an incidence of 40° without compromising the pattern synthesis capabilities.

The magnitudes of the reflections for both polarisations remained identical until approximately 55° incidence. Because we adopted a phase-only pattern synthesis process, the amplitude variations did not significantly affect the accuracy of the peak locations but the overall gain values. However, after 55° incidence, there begins to exhibit a significant difference in the amplitude value of the two polarisations, which will also affect the accuracy of the pattern synthesis. Thus, we can suggest that the device is capable of operating from -40° to 40° (azimuth and horizontal) for both TE and TM polarisations, as shown in fig. 8.18.

In algorithm-1, we show the pseudo-code for the unit cell's dimensional optimisation procedure. The input of this code is the S11 reflection phase and amplitude for the ON and the OFF states, given the varying unit cell height and width; this data is retrieved from the parameter sweep in CST's full-wave simulation. After importing these data in Matlab, we search for the satisfactory S11 reflection phase and amplitude values, given the search criteria of 1) S11 phase difference between the ON and the OFF states shall be close to 180 degrees, and 2), the S11 amplitude difference between the ON and OFF states shall be close to null. The search will then return the optimal values accordingly.

8.2.3 Theoretical Farfield

For an extensive view, understanding and derivation of the farfield equations, please refer to chapter 4.1. In this section, we will directly make use of the farfield equation.

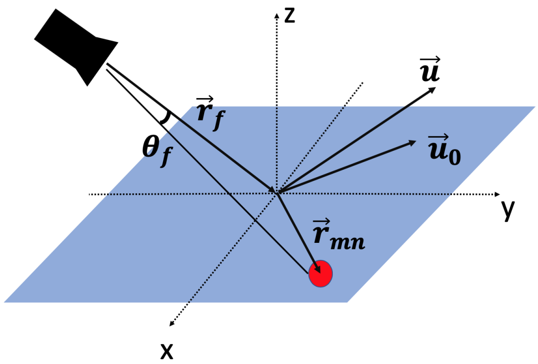

Figure 8.11: Conventions used for the farfield radiation pattern calculations.

The antenna farfield radiation pattern[31], $E(\theta, \phi)$, is essentially a summation of EM radiation from the feed source to individual antenna elements and finally to the farfield region (where there are only dependencies on θ and ϕ). With reference to fig. 8.11, we can derive the farfield radiation pattern. The feed source radiation pattern is modelled as cosine to the power of q. The exponential term is the spherical wave radiation from each individual antenna element, which can have a unique amplitude (Γ_{mn}) and phase terms ($e^{i\phi_{mn}}$). In (1), we have the farfield radiation pattern, $E(\theta, \phi)$:

$$E(\theta, \phi) = \sum_{m=1}^{M} \sum_{n=1}^{N} \cos^q \theta \frac{\cos^q \theta_f}{|\vec{r}_{mn} - \vec{r}_f|} \cdot e^{-ik(|\vec{r}_{mn} - \vec{r}_f| - \vec{r}_{mn} \cdot \hat{u})} \Gamma_{mn} \cdot e^{i\phi_{mn}}, \tag{8.5}$$

where ϕ_{mn} is the configuration matrix of the ON/OFF state, which is multiplied by the phase difference between the ON and OFF states, ϕ_Δ:

$$\phi_{mn} = \begin{bmatrix} 1/0 & 1/0 & \dots & 1/0 \\ 1/0 & 1/0 & \dots & 1/0 \\ \vdots & \vdots & \ddots & \vdots \\ 1/0 & 1/0 & \dots & 1/0 \end{bmatrix} \cdot \phi_{\Delta}. \tag{8.6}$$

This antenna radiation pattern approximation is used for basic farfield calculations; however, for multibeam optimization with the GA algorithm, we adopted a more accurate semi-analytical model, which could include more intricate EM details such as coupling, edge and surface effects:

$$E(\theta,\phi) = \sum_{m=1}^{M}\sum_{n=1}^{N} \frac{A(\theta,\phi)}{|\vec{r}_{mn} - \vec{r}_f|} \cdot e^{-ik(|\vec{r}_{mn}-\vec{r}_f|-\vec{r}_{mn}\cdot\hat{u})}\Gamma_{mn} \cdot e^{i\phi_{mn}}. \tag{8.7}$$

Instead of approximating the unit cell antenna radiation pattern as cosine to the power of q, we performed a full-wave simulation of the unit cell radiation pattern under periodic conditions (with infinitely many unit cells as the repeating periodic boundary condition), as shown in Fig. 8.12. We then replaced the cosine unit cell radiation pattern approximation with the full-wave derived farfield radiation pattern, $A(\theta,\phi)$. In this way, we have a more reliable farfield prediction, which is especially needed when synthesising a higher number of multibeams where noises/SLLs are higher.

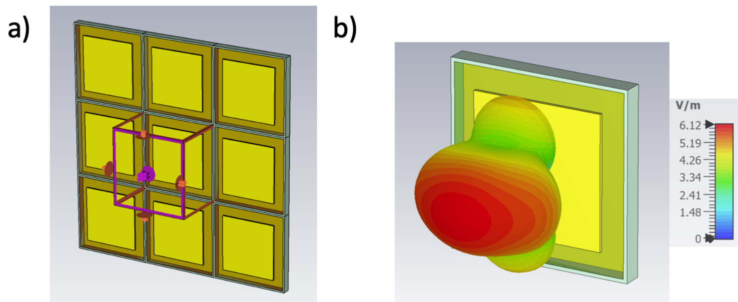

Figure 8.12: Unit cell radiation pattern ($A(\theta,\phi)$) retrieved from infinite periodic conditions (only showing the nearest eight unit cells). a) The purple box is the simulation box, where the radiation pattern shown in b), is recorded for the unit cell.

8.2.4 Directivity

The directivity of the metasurface is calculated as follows:

$$D(\theta, \phi) = \frac{U(\theta, \phi)}{\frac{1}{4\pi}\int_0^{2\pi}\int_0^{\pi/2} U(\theta, \phi)\sin\theta d\theta d\phi}, \tag{8.8}$$

where $U(\theta, \phi) = |E(\theta, \phi)|^2$ is the radiation intensity, which is divided by the total radiation power. The integration in θ is limited to $\pi/2$ because of the nature of reflectarray operations, where only the upper semi-sphere where EM waves are reflected is of interest.

8.2.5 Phase Distribution

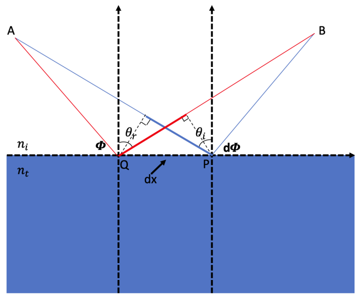

Figure 8.13: The generalised Snell's law for the case of reflection.

The configuration of the ON/OFF states of the unit cells results in a specific distribution of reflection phases (specifically, a 180° reflection phase difference between the ON and OFF states). The reflection phase distribution across the device's surface ultimately determines the behaviour of the reflected waves according to Huygens' principle. A fundamental theoretical concept in synthesising simple phase distributions is the Generalised Snell's Law (GSL)[83].

In fig. 8.13, a graphical representation of an EM wave travelling from point A to point B via two infinitesimally spaced reflection points Q and P is shown. The path difference between Q and P also includes a phase difference of $d\Phi$. GSL is derived from Fermat's principle, whereupon momentum conservation, we arrive at the continuity of the phase condition at the reflection boundary, and when an extra phase profile Φ is introduced, this momentum conservation leads to generalised Snell's Law for reflection:

$$\sin\theta_r - \sin\theta_i = \frac{\lambda_0}{2\pi n_i}\frac{d\Phi}{dx}, \tag{8.9}$$

where n_i is the refractive index, and the sub-indices represent either incident or reflection. From the generalised Snell's law, we can see how an arbitrary reflection phase (also known as anomalous reflection, when $\theta_i \neq \theta_r$) can be achieved when a phase gradient $\frac{d\Phi}{dx}$ can be artificially engineered.

A simple derivation can be observed from fig. 8.13, where we have two light paths that trace from point A to point B, which are infinitesimally close to each other; thus, their phase difference should approach zero. With this in mind, we can derive an expression for the path differences (highlighted by bold red and bold blue) and equal that to zero:

$$[k_0 n_i \sin\theta_i dx + (\Phi + d\Phi)] - [k_0 n_i \sin\theta_r dx + \Phi] = 0 \tag{8.10}$$

After some re-arrangements of eq. 8.10, we can then arrive at the generalised Snell's law for the case of reflection. Notice that if the phase profile $\Phi(x)$ is constant, then we would retrieve the traditional Snell's law. With a linear phase gradient, we can achieve anomalous reflection.

It is relatively straightforward to see how beamsteering, namely anomalous reflection, can be achieved through the introduction of a constant phase gradient; in 2D array theory, it is well known that the continuous phase change required for beamsteering applications is as follows:

$$\begin{aligned}\Phi_r(x_i, y_i) = &- k_0 \sin\theta_i(\cos\phi_i x_i + \sin\phi_i y_i) - \\ &k_0 \sin_b(\cos\phi_b x_i + \sin\phi_b y_i),\end{aligned} \tag{8.11}$$

where the indices b represent the beam-steered, i for incidence, and x_i and y_i for the coordinates of each of the unit cell antennas. For more complex beam profiles, such as multi-directional multibeams, the solution can be retrieved through numerical optimisation methods, which in our case is the GA.

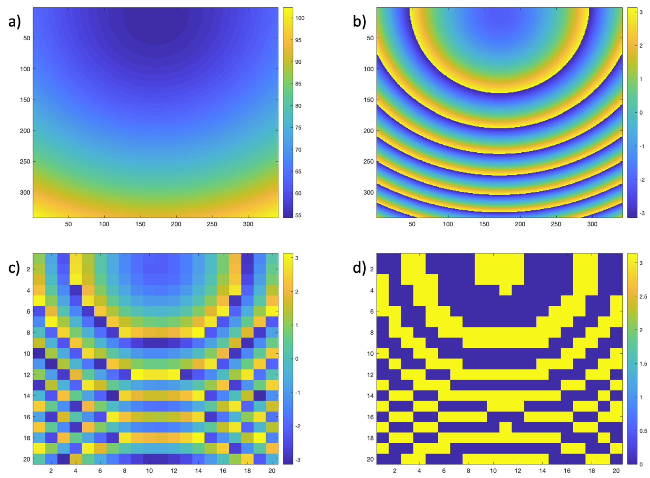

Figure 8.14: The required surface reflection phase distribution in order to achieve a beamsteering of $\theta = 30°$ and $\phi = 90°$, from a point-like feed source that is situated 10λ above the centre of the surface. a) smooth phase gradient b) wrapped phase gradient c) quantised (into 20x20 elements) phase gradient and d) binary version of the quantised phase gradient. The units are in gradient.

In fig. 8.14, we demonstrate the process of obtaining the appropriate surface phase distribution, from eq. 8.11, for an intended beamsteering of $\theta = 30°$ and $\phi = 90°$, with a feed horn that is approximated as a dipole source with omnidirectional radiation pattern, which is located ten wavelengths above the centre of the reflectarray metasurface. The reflectarray has a total of 20 x 20 antenna elements that operate in binary states (either ON or OFF). The process begins with eq. 8.11, which leads us to a continuous phase distribution; after wrapping this into the meaningful range of 0 to 2π, we then quantise the distribution into the dimensions of the controllable surface (20 x 20). Finally, since our reflectarray will only be capable of binary states that either create no phase difference or 180 degrees reflection phase difference, we also need to account for this binary effect. The final phase distribution that the surface will need to achieve in order for the intended beamsteering to take place is demonstrated in fig. 8.14 d).

8.2.6 Feed Horn

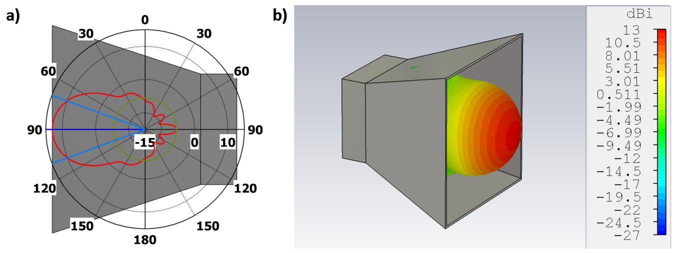

Figure 8.15: The feed source horn antenna. (a) Farfield directivity in the polar plot at $\phi = 0°$ with the red line, dark blue line for the main lobe direction, light blue for the 3 dB beamwidth (40.1°), and green circle for the SLL, (b) 3D radiation pattern and corresponding directivity in dBi.

The feed horn has a dipole embedded inside, which radiates omnidirectionally, while the horn cover serves as a guide to focus the EM energy toward the intended surface. We designed the horn to maximise the gain achieved and radiation coverage to the surface. The design and optimisation of the feed horn are important; otherwise, the assumptions made in theoretical models would mismatch the full-wave simulation conditions and result in inaccurate farfields.

In Fig. 8.15 part (a), we can see that the 3 dB beamwidth is 40°; this is designed according to the horn aperture and distance to the reflectarray surface, in order to maximise coverage and, at the same time, provide relatively uniform strength of radiation across, an assumption made in the theoretical modelling of the excitation source.

8.3 Numerical Simulations

Using the transient solver in CST, we have simulated a 20 by 20 metasurface reflection EM radiation pattern, given various combinations of ON and OFF states of the LC unit cell. Here we present a few classical combinations, such as the parallel stripes and the checkerboard. These results correspond well with our expectations and also with results from other references, which have studied reconfigurable metasurface using PIN Diode unit cells in lower frequencies.

In fig. 8.16, we have three rows of figures: in the first row (for a), b) and c)), we have the reflection phase configuration on the surface of the reconfigurable reflectarray; in the second row, we have the theoretical farfield pattern corresponding to the reflection phase profile shown in the first row; in the third row, we have the full-wave simulation results retrieved from CST. The input source is a plane wave. The idea here is to verify that the device is performing as expected, as the reflection phase configurations and their corresponding farfield profiles are well-known.

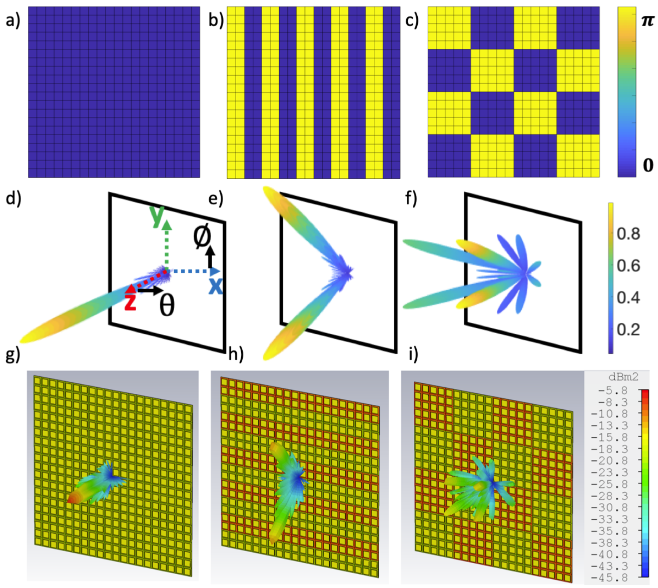

Figure 8.16: For a linearly polarised, normally incident EM wave, a), b) and c) are the phase modifications resulting from reflecting off of the 20x20 antenna elements, d), e) and f) are the corresponding farfields results visualised from using the farfield equation, g), h) and i) are the corresponding farfields results visualised from using the full-wave simulation method.

In this section, we demonstrate the farfield radiation patterns for both the beam scanning and multibeam scenarios. For these results, we used the feedhorn antenna described in the section above at a distance of 10λ above the device. This specific distance is chosen as we intend to simulate an integrated feed horn, where excitation is near the reflectarray surface.

In Fig. 8.17, we show the general agreement between the theoretical normalised farfield electric field and the full-wave normalised farfield electric field. The ON/OFF states are shown as green/red unit cells in the figure. These farfield radiation patterns were also checked with those in other studies[61, 32, 57], where the same configurations of ON/OFF are used.

In Fig. 8.18, we show a collection of the full-wave beam-scanning simulation results, for $\phi = 135°$ and θ scanning from $0°$ to $57°$. At angles greater than $40°$, such as at $\theta = 57°$, not only is the beamwidth greatly increased (and the beam profile became asymmetrical to the peak), but also the directivity significantly decreased. However, from $\theta = 0°$ to $\theta = 40°$, the directivities are almost identical, with a minor increase in the beamwidth as the scanning angle increases.

In Fig. 8.19 a), we show the theoretical and full-wave farfield radiation pattern when the configuration is set to steer the beam to $\theta = 15°, \phi = 135°$. By using (8.11), we can determine the phase distribution required to

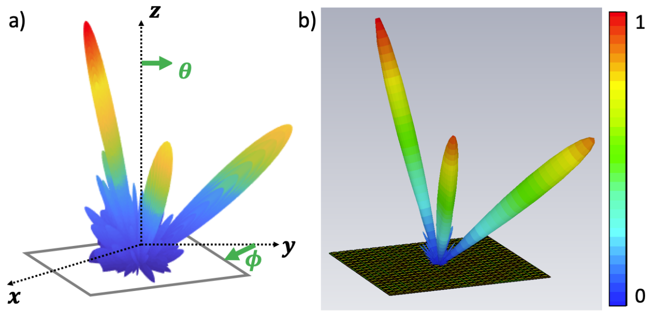

Figure 8.17: (a) Theoretical and (b) full-wave normalized farfield electric field.

achieve a certain beamsteering angle, which can then be used to construct the configurations of the ON and OFF states. Similarly, in Fig. 8.19 b), the case for $\theta = 30°, \phi = 315°$ is shown.

In Fig. 8.19 c), we demonstrate the theoretical and full-wave radiation patterns of a GA-optimized three-beam configuration. In the top plot of Fig. 8.19 c), we show the theoretical farfield radiation pattern plot, excited by an ideal dipole horn feeder that is located at 10λ above the device surface. The three beams are GA-optimized for steering at $(\theta = 15°, \phi = 45°)$, $(\theta = 45°, \phi = 165°)$, and $(\theta = 50°, \phi = 225°)$. In the bottom plot of Fig. 8.19 c), we present the full-wave simulation plot for the same configuration that gives the 3-beam split. In this plot, we see that each of the three steered main lobes has a directivity of at least 14 dBi, which shows promising performance in terms of the beam-forming capabilities of our device, given that the horn antenna has a directivity of 13 dBi.

Similarly, in Fig. 8.19 d), we demonstrate the GA-optimized four-beam split, where the four beams are optimized at the angles of $(\theta = 15°, \phi = 45°), (\theta = 20°, \phi = 135°), (\theta = 25°, \phi = 165°)$ and $(\theta = 30°, \phi = 225°)$. Although the main peaks are correct in terms of position, it is noticeable that the noise and SLL are more significant here, likely because of the limitations of the device's dimensions: the lower the number of unit cells, the lower the resolution of the multibeams.

In table. 8.3, we listed the KPIs that are derived from semi-analytical calculations and full-wave simulations. Although the beamwidths of the semi-analytical model are consistent with those of the full-wave simulations, the semi-analytical main lobes (and consequently sidelobes) are approximately 4 dBi stronger than those of the full-wave simulations. We believe that the inconsistencies in weaker radiation regions, and the overestimation in mainlobe/sidelobe strengths can be attributed to the absence of considerations in the theoretical model of the: 1) coupling effects between the individual antennas, which become significant in the subwavelength regime,

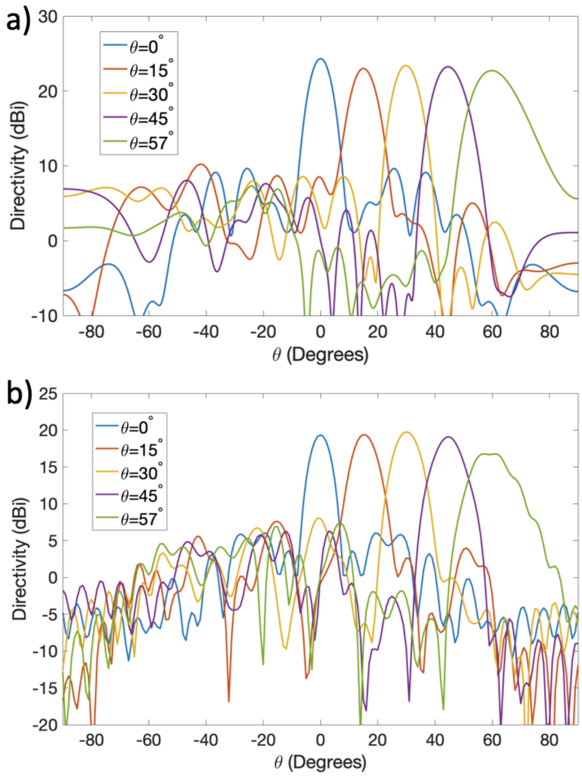

Figure 8.18: a) Semi-analytical and b) full-wave simulation of the radiation patterns for $\phi = 135°$.

and often manifest as resonant features, as observed in the full-wave plots, in terms of the oscillatory blue lines versus the smooth blue lines in theoretical plots; 2) material losses and surface effects, such as surface waves, which can lead to secondary radiation manifesting in the weaker radiation regions and decreasing the main-lobe intensity. However, it is important to note that the decibel-scale plot disproportionately magnifies any numerical effects and errors.

We would also like to point out that, likely due to the step-size and accuracy settings in the full-wave simulations, the lowest farfield radiation intensities recorded in full-wave simulations are much higher in comparison to the lowest radiation intensities in the theoretical farfield plot (-21 dBi in full-wave versus -46 dBi in theoretical, for beamsteering). To clarify the theoretical farfield contour plots in the areas of interest (mainlobe and sidelobes), we extended the range of lower intensity values for the lower colour range (lower intensity values are inside the blue colour range) while maintaining the higher intensities in a colour range that is consistent with colour mapping of full-wave plots.

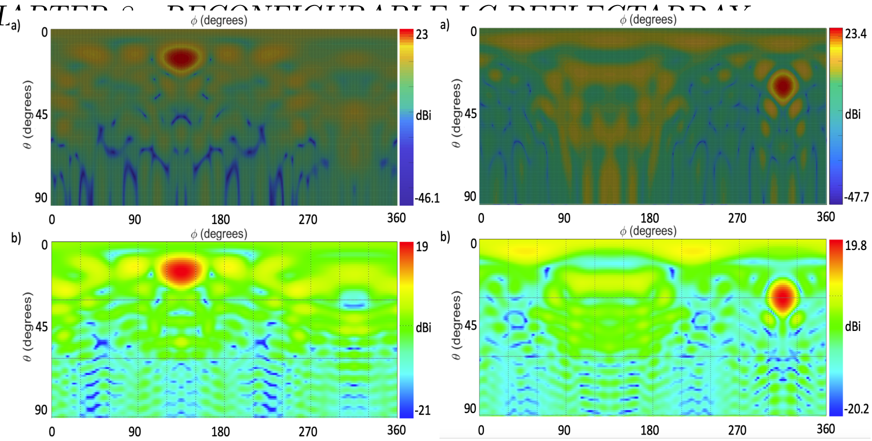

(a) (b)

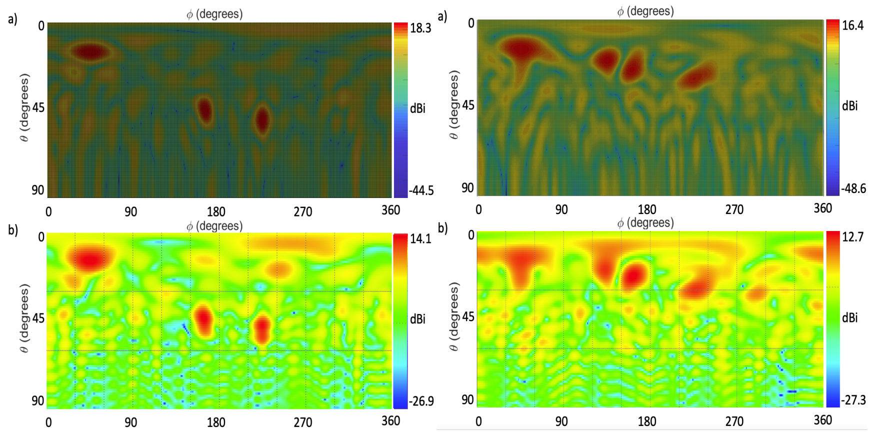

(c) (d)

Figure 8.19: a) 2D Farfield directivity plot of beamsteering towards $\theta = 15°, \phi = 135°$, b) beamsteering towards $\theta = 30°, \phi = 315°$, c) GA optimized 3 beam split, and d) GA optimized 4 beam split. In each subplot, the above plot is the semi-analytical plot and the below plot is the full-wave simulation plot.

Table 8.3: KPIs for different scan angles.

	$\boldsymbol{\phi = 135°}$				$\boldsymbol{\phi = 90°}$			
	$\boldsymbol{\theta = 0°}$	$\boldsymbol{\theta = 15°}$	$\boldsymbol{\theta = 30°}$	$\boldsymbol{\theta = 45°}$	$\boldsymbol{\theta = 0°}$	$\boldsymbol{\theta = 15°}$	$\boldsymbol{\theta = 30°}$	$\boldsymbol{\theta = 45°}$
Directivity_T (dBi)	24.3	23.0	23.4	23.2	24.3	23.3	23.7	23.1
Directivity_F (dBi)	19.4	19.4	19.8	19.1	19.4	19.8	19.7	18.9
SLL_T (dBi)	-14.7	-12.8	-14.8	-15.2	-14.7	-10.4	-12.8	-13.0
SLL_F (dBi)	-13.3	-11.8	-11.7	-12.8	-13.3	-12.0	-11.5	-10.5
Beamwidth_T (°)	7.0	8.2	8.4	10.2	7.0	7.3	8.14	10.0
Beamwidth_F (°)	7.1	8.6	9.3	10.0	7.1	7.7	8.9	9.5

8.4 Super Cell Structure

When performing the EM simulation with CST on the entire reflectarray, it is rather tricky to set up the entire model (e.g. a 50 by 50 array with a unique coding configuration), but thankfully VBA scripting is allowed in CST, and in combination with Matlab has significantly facilitated the construction of different statuses of the reflectarray for simulations. In algorithm-2, a pseudo-code is presented to explain this process.

Algorithm 2: VBA script to initialise structure in CST according to configuration

```
Data: FILE - configuration of ON/OFF, 20 by 20 matrix
Result: Full device model updated according to ON/OFF
        configuration and ready for full-wave simulation
Initialise 20 by 20 structure with permittivity ε undefined;
while not end of line do
    A ← read current line;
    B ← split(A) with delimiter;
    for counter1, counter2 do
        Matrix(counter1,counter2)=B(counter1,counter2);
        update counters;
    end
end
for i=1:20 do
    for j=1:20 do
        if Matrix(i,j)==1 then
            ε_{i,j}=2.46; tan δ = 0.02;
        else
            ε_{i,j}=3.28; tan δ = 0.015;
        end
    end
end
```

In CST, there is a specific in-built function called array task, which allows the user to construct a superlattice version of the model based on the unit cell design. However, this operation does not include any freedom in redefining the unit cell structure (except for excitation strength variations, which are irrelevant to us since these patch antennas are passive). This is a problem as in our reflectarray LC case, the ON and OFF states of the unit cell status corresponded to a different model of the substrate, which means that according to the ON/OFF, we needed to modify the unit cell properties. Therefore, we had to use VBA scripts to automate a sequence to be able to do this procedure efficiently. The specific CST page with the

VBA script input panel is shown in fig. 8.20.

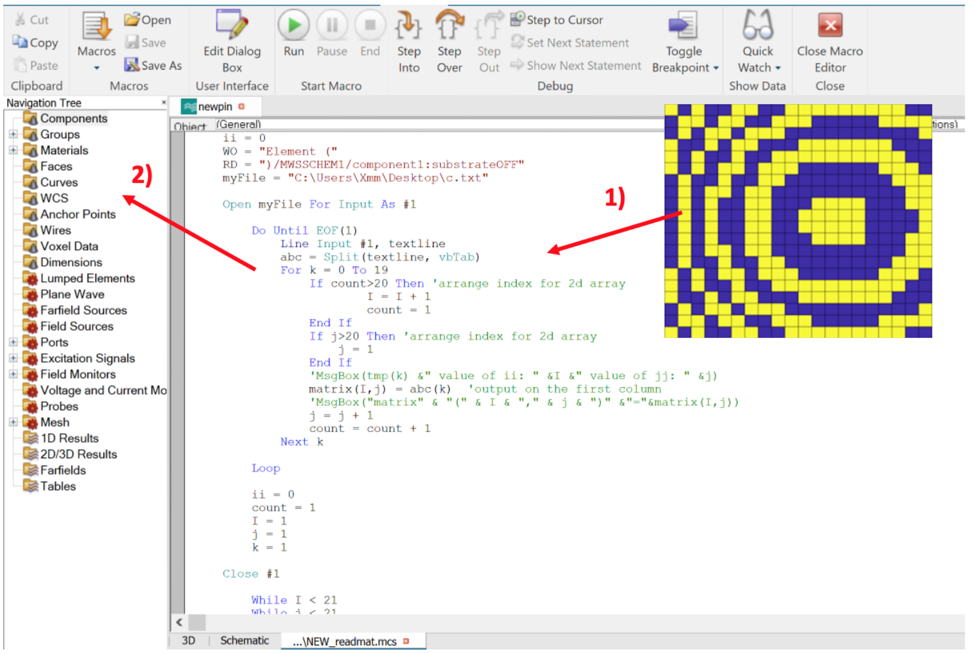

Figure 8.20: The ON/OFF configuration that leads to a beam steering pattern when illuminated by an off-axis point source, the CST VBA editor interface and an excerpt of the supercell model automation code.1) Reading the ON/OFF matrix, 2) performing permittivity changes accordingly.

Chapter 9

Scalability Analysis

Ideally, the reflectarray would have optimum directivity if it can achieve continuous control of the reflected phases ($0° - 360°$) from each antenna element, similar to the operation of a traditional phased array. However, achieving a full 360° and continuous control often comes at the cost of increased power consumption, cost, and design complexity. Thus, it is of interest to understand the relation between directivity and phase quantisation error, which can result from the continuousness of the reflected phase or the degree of spacing from the subwavelength elements.

In Fig. 9.1 a), in a 20×20 elements reflectarray, the continuous control over phase produces a directivity of 31.09 dB, while the binary phase control produces 26.17 dB, which is approximately 5 dB difference. This significant gain advantage of the continuous phase control device could be of interest to certain applications. However, practically, it will come at the cost of higher power consumption (from the variable voltage controls), lower energy-efficiency, and greater complexity in the design, which will ultimately lead to a more expensive device for manufacturing.

In Fig. 9.1 b), given the same aperture of the reflectarray, the directivity of $\lambda/2$ unit cells is 26.17 dB, while the directivity for $\lambda/8$unit cells is 28.5 dB, approximately 2 dB difference. This shows that by increasing the number of elements while retaining the overall structure size, having more and smaller radiating elements enhances the intensity of the reflected field. Nonetheless, there are certain effects as a result of increasing element density. First, the bandwidth of the full device tends to decrease. Second, when the radiating elements are electrically very small, surface waves or even localised surface plasmons may result at such a scale, thus reducing the radiation efficiency.

Fig. 9.1 c) shows the directivity of binary phase reflectarrays with three different aperture sizes. 20×20 elements has a directivity of 31.09 dB, 40 by 40 elements gives 36.91 dB and 80 by 80 elements gives 42.65 dB. The aperture of the device is directly related to the gain, so the only underlying consideration here is the application intention and budget available for the

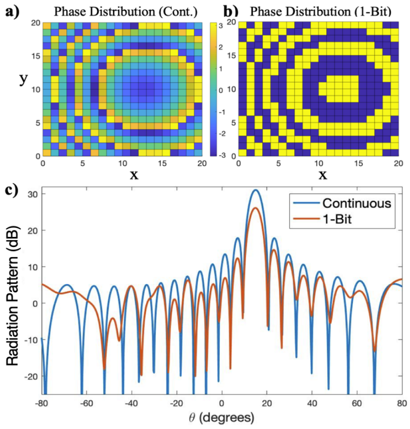

(a)

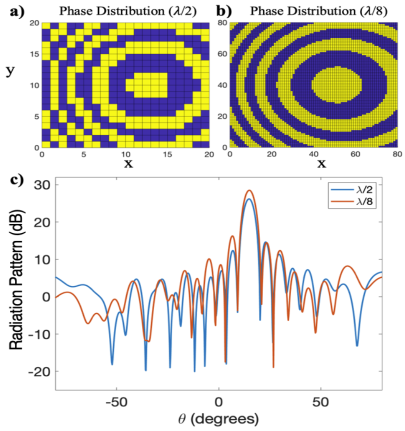

(b)

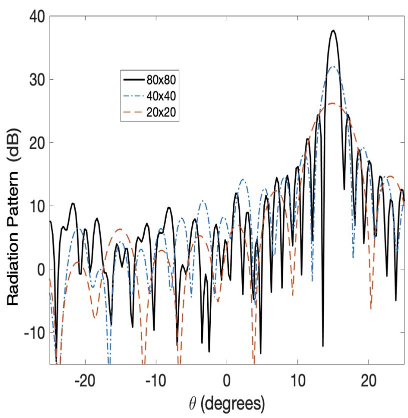

(c)

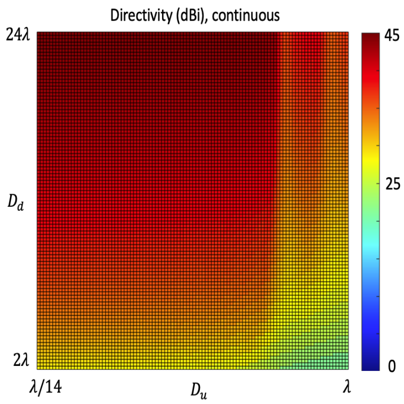

(d)

Figure 9.1: a) Phase profile and directivity for $\theta = 15°$ beamsteering from a f/d=0.5 (5λ above) central feed source. The corresponding phase distribution for a 20×20 reflectarray with a continuous degree of change in the reflected phase (from $0° - 360°$) and binary degree ($0°$ or $180°$) of change in the reflected phase, b) 20×20, $\lambda/2$ elements, (b) 80×80, $\lambda/8$ elements, and (c) directivity comparison c) The directivity comparison between three different aperture sizes: 20×20, 40×40 and 80×80 d) directivity plot, D_u for unit cell dimension and D_d for device dimension.

appropriate aperture.

In Fig. 9.1 d), we show the directivities of 100x100 different devices, each with a different unit cell dimension, D_u, and an overall device dimension, D_d. The range of unit cell dimension goes from $\lambda/14$ to λ, while the range of aperture/overall device dimension goes from 2λ to 24λ. In each unit cell antenna, we have allowed a continuous degree of reflection phase control

(0° to 360°). In general, the device would achieve the highest gain (44.45 dBi) with the largest device dimension and the smallest unit cell speaking, which results in the highest density and quantity of antenna elements. The lowest directivity (21.28 dBi) is resulted when we have a small aperture size (D_d) and large spacing between the unit elements. We can see that at around $D_u = 0.6\lambda$, the increase of directivity due to the decrease in unit cell dimension stops. At this point, for most aperture/overall device sizes, it is not beneficial to have smaller spacings between the unit cells. Thus, this lays a good reference point for the minimum unit cell spacing that will achieve maximum directivity, while saving the troubles of creating even smaller unit cells.

Table 9.1: Summary of the KPIs for different dimensions of the reflectarray when using binary phase unit cells.

Device Dimensions	**2x2**	**4x4**	**8x8**	**16x16**	**32x32**	**64x64**
Beamwidth ($^\circ$)	60.1	32.5	16.8	8.5	4.3	2.1
Directivity (dB)	10.4	15	20.4	26.2	32.1	38.1

In table. 9.1, we notice that the 3 dB beamwidth is halved every time the device area is doubled, whereas the main-lobe gain increases by approximately 5 dB following each device area doubling.

In Figure. 9.2, we present the directivity, target deviation (TD), HPBW and SLL plots, contrasting a 1-bit (reflection phase of 0° or 180°) and 2-bit (0°, 90°, 180° and 270° reflection phases) control devices.

For the directivities of 1-bit and 2-bit devices, similar statements (as to those of the continuous-control device) can be made, although with slight differences in the details. For the 1-bit device, we can notice that there is a significantly greater area of lower directivity for aperture sizes less than around 6λ, whereas for the 2-bit and continuous-phase cases, only for aperture sizes less than around 3λ contribute to a significantly lower directivity. This is primarily due to the quantisation error effect: with fewer bits to describe the farfield, the overall farfield "image" will have less "resolution". Thus, more element numbers will be needed to enhance the directivity. As a comparison, the highest directivity value for the continuous-phase control device, is 45 dBi, for 2-bit, it is 44 dBi, and for 1-bit, it is 42 dBi. Also noticeably different in the 1-bit case is the boundary between decreasing elements spacing and enhancing directivity: this boundary is less linear and appears to cut-off at $\lambda/2$, where any smaller spacing would stop enhancing the directivity strength.

The TD is a measure of the accuracy of our farfield. It is defined as: $T_d = \sqrt{(\theta_a - \theta_d)^2 + (\phi_a - \phi_d)^2}$, where the sub-indices a and d represent actual and desired components of the focused beam; it is essentially a measure of the difference between the actual steered beam angle and the desired steered

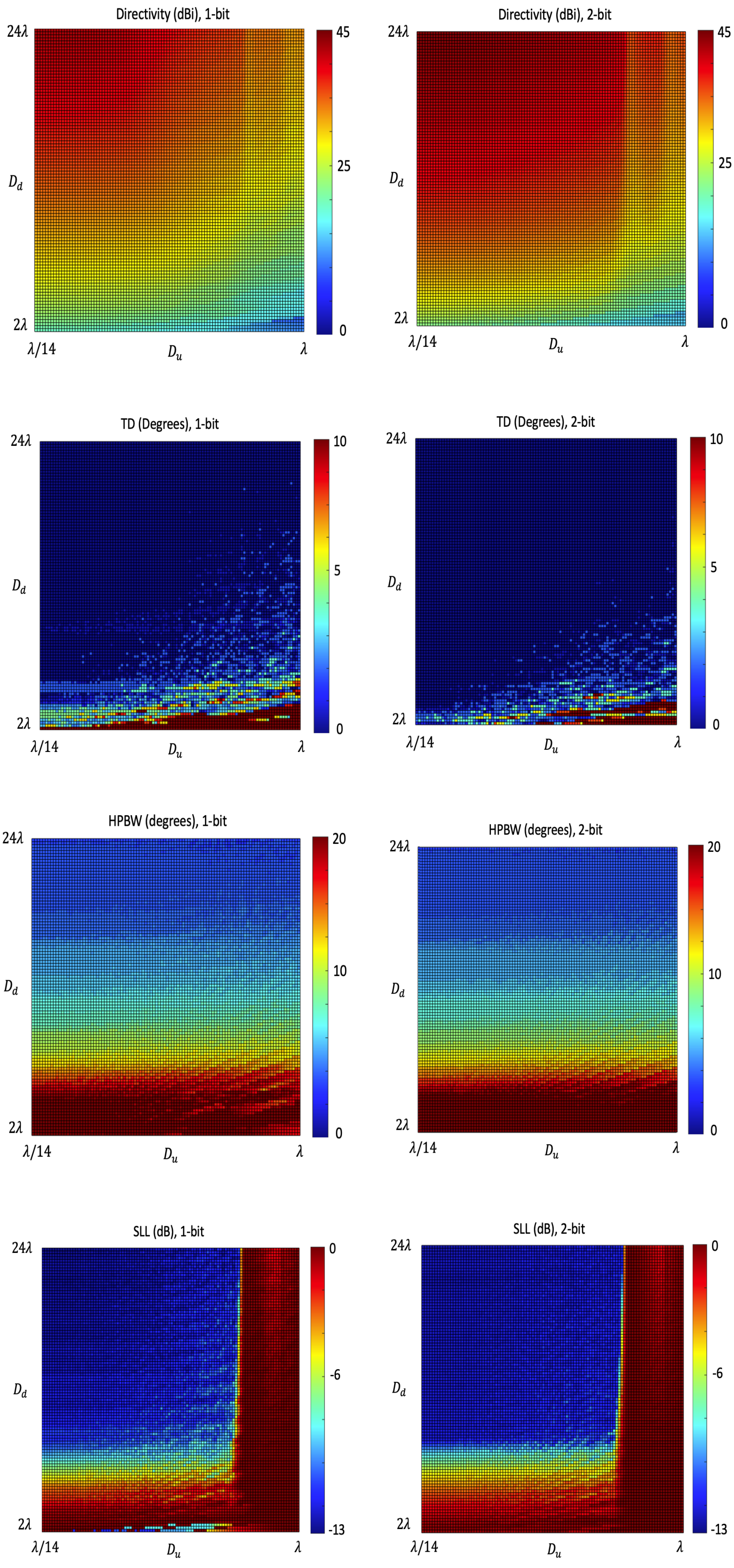

Figure 9.2: 1-bit versus 2-bit comparisons.

beam angle. For the TD calculations presented in Fig. 9.2, we have used $\theta_d = 15°$ and $\phi_d = 20°$. Overall, we observe that for each aperture size, having smaller element spacing will reduce the TD. This is as expected, as with smaller element spacing, we would essentially have a higher resolution of the steered beam. The TD is at its greatest when the aperture is small, and the element spacings are large, where quantisation errors are most significant.

For the HPBW, we notice that it seems to primarily depend on the overall device size, at least for the range of values that we have tested. Given the same element spacing D_u, with a bigger aperture D_d, we will have more elements and thus a narrower beam. However, as we increase the number of elements by decreasing element spacing while maintaining device aperture, we will not lower the HPBW as the elements have a higher density, and thus contributing to a relatively wider profile. For any device, we would want to minimise the HPBW, which will enhance the directivity and resolution of the farfield profile.

The SLL plots show that for both the 1-bit and 2-bit devices, the region of high SLL is where the device dimensions are small (regardless of unit cell dimensions), and where both the device dimensions are unit cell dimensions are high. In the first scenario, where the device dimension is small, this greatly limits the number of reflecting antennas on the device, thus contributing to lower resolution and higher SLL. In the second scenario, having a large device with large element spacings also creates problems with resolutions, as the antennas are too far apart to interfere collectively and constructively at a single position, leading to high sidelobe peaks away from the main lobe. The difference between the 1-bit and 2-bit SLL can be seen in the blue region where there is a desirable level of SLL: in this region, the 2-bit SLL performs better than the 1-bit device with a lower average SLL, which is contributed by the greater degree of reflection phase freedom. SLL can be not only a source of interference, but also an indication of energy inefficiency (radiation energy lost to unwanted directions), and thus should be minimised accordingly to acceptable levels.

In Fig. 9.3, we present two plots that compare varying unit cell sizes and varying device dimensions/apertures. For both plots, the target beam-steering angle is at $\theta = 15°$ and $\phi = 20°$. The unit cells are in a binary configuration (only 0° or 180° reflection phase). For Fig. 9.3 a), the device size/aperture is fixed at a constant size of $d_d = 15\lambda$, while the unit cell sizes vary between $d_u = 1/4\lambda$, $d_u = 1/2\lambda$ and $d_u = 3/4\lambda$. For Fig. 9.3 b), the unit cell size is kept at a constant of $d_u = \lambda/2$, while the device dimension/aperture varies between $d_d = 4\lambda$, $d_d = 12\lambda$ and $d_d = 20\lambda$. A general observation that we can make is that the SLL seem to improve with lowering the unit cell sizes, while the HPBW seem to improve with larger device dimension/aperture. The increase in aperture benefits not only the HPBW, but also the SLL, as there are more radiating unit cells when the aperture increases (given the constant unit cell size), which will enhance

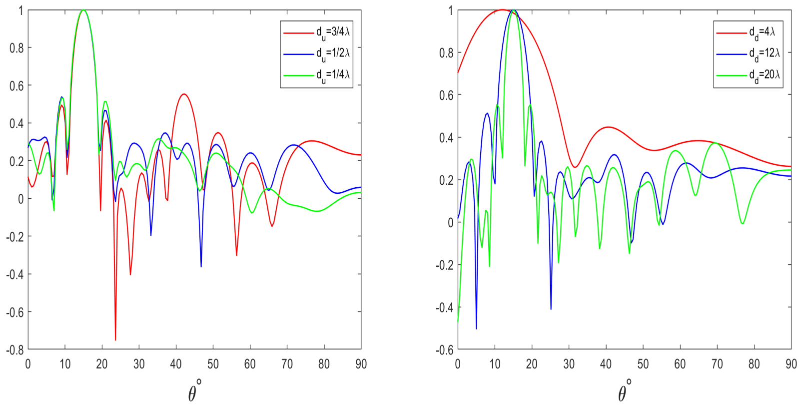

(a) (b)

Figure 9.3: The normalised directivity comparisons for a 1-bit surface: a) a constant device size of $d_d = 15\lambda$ with varying unit cell sizes b) a constant unit ... e of stee

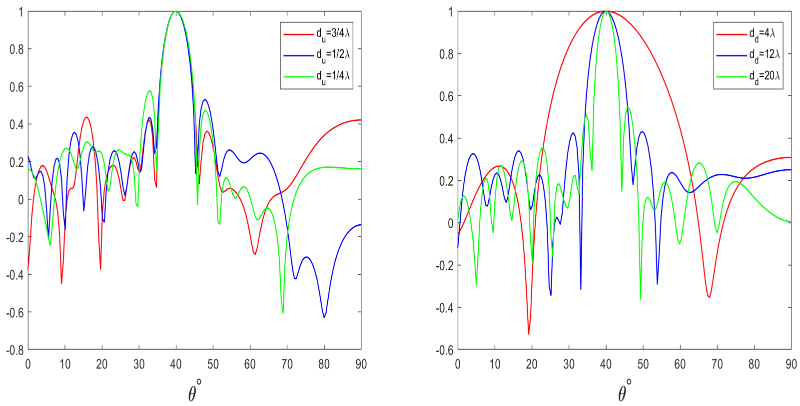

(a) (b)

Figure 9.4: 1-bit normalised directivity comparisons, with steering angle at $\theta = 40°$ and $\phi = 20°$.

the resolution. However, for a constant aperture size, when the unit cell dimension decreases, the HPBW remains the same, while only the SLL seem to be improving. In this way, we can characterise the "resolution" or spatial localisation of the farfield beams to have two attributes: that of spatial confinement (how narrow the beam is), and that of spatial contrast (how low the SLL is). From these analyses, it shows that the spatial confinement (HPBW) improves when the effective area of reflection (aperture) increases, while maintaining the same density of unit cells. The spatial contrast (SLL) improves when the density of the unit cell increases. These observations can be useful in the design of reconfigurable intelligent surfaces (RIS) with specific KPI targets in mind. In Fig. 9.3 b), the case of $d_d = 4\lambda$, the slight offset of the peak from $\theta = 15°$ is due to the lack of unit elements, which results in poorer accuracy of the peak location.

In Fig. 9.4, we present a similar set of two normalised directivity comparison plots, with a more extreme steering elevation angle of $\theta = 40°$ (azimuth angle is the same as before, $\phi = 20°$). With the greater elevation steering angle, the phase gradient that the unit elements must possess becomes steeper, as the radius of the phase gradient shortens. Thus, the quantisation error becomes greater in this 1-bit configuration, leading to reduced performance in both the HPBW and SLL, as well as the overall strength of directivity, which is not presented in the plots.

Chapter 10

Phase Retrieval

An EM wave contains both the information about its amplitude and phase. In many applications, knowing the amplitude of the EM wave suffices, such as the imagining of a picture, we only need to know, or desire, the intensity of light, but the phase is irrelevant to our viewing of the picture. In certain applications, such as transmission electron microscopy, x-ray crystallography, and in our case, finding the phase distribution of each of the reflectarray antenna elements, we also need to know the phase information. The amplitude of the EM wave can be easily obtained, such as through the measurement of the field intensity, while retrieving the phase information from measurements is not always straightforward. This problem of the missing phase information is known as the "phase problem".

$$G(k) = |G(k)|e^{i\phi(k)} = \int_{-\infty}^{\infty} g(x)e^{-2\pi ik\cdot x}dx \tag{10.1}$$

In eq. 10.1, $G(k)$ is a complex signal, which is composed of an amplitude term, $|G(k)|$, and a phase term, $\phi(k)$. The x and k are the multidimensional spatial- and frequency-domain general coordinates. We see that, given a function of $f(x)$, which can be a function of the electric field strength, we can arrive at its reciprocal representation in frequency-domain; however, after the transform (integration), we leave out the information on phase, $\phi(k)$.

As seen above, the phase problem is not only present in measurement methods, but also in the analytical domains. In our problem, we intend to retrieve the optimal phase distribution of an MxN size reflectarray from intensity calculations of the farfield. The farfield and nearfield (where the phase distribution lies) can be related by a transform pair, which can be in vector form, described in eq. 10.7 and fig. 10.4, or scalar form, described in eq. 10.8 and fig. 10.5.

10.1 Genetic Algorithm

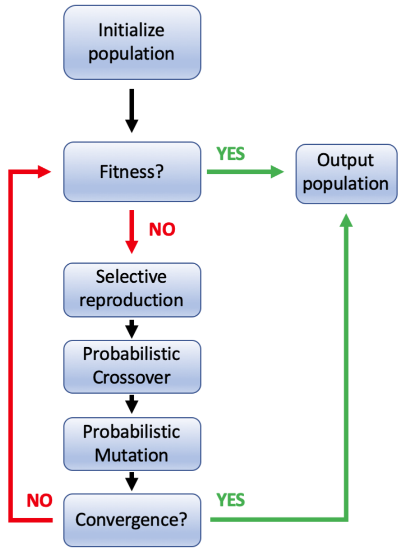

Figure 10.1: GA algorithm flowchart

In order to solve the inverse problem described in (8.5), where we have an intended farfield radiation profile $E(\theta, \phi)$ and are looking for the input 20×20 configuration matrix ϕ_{mn}. This problem can be addressed using GA, which is an optimisation algorithm motivated by biological evolutionary processes.

As shown in Fig. 10.1, we start the GA optimisation algorithm with an initial population (where the population is the matrix of ON/OFF configurations); this can either be randomly generated or, in our case, loaded from a library of pre-stored known configurations, to fasten the optimisation. The cost function, otherwise known as the fitness function, determines the quality of our optimised configuration, which is simply the difference between the intended farfield radiation profile and the optimised profile:

$$cost = |E - E_{target}|^2, \tag{10.2}$$

where E_{target} is the desired electric field and E the current outcome.

As described in the previous section, the theoretical farfield is calculated with a given configuration matrix that represents the ON and OFF states of the individual unit cell antennas. The ON and OFF configurations govern the radiation pattern of the reconfigurable reflectarray. Thus, we seek to solve the inverse problem in (8.5), where we have a desired and known radiation pattern (a multibeam steering, for instance) but are looking for a non-trivial input matrix.

Together with the GA toolbox offered by MATLAB, we also developed our own custom probabilistic crossover and mutation functions to better tailor to the optimisation problem that we have. The general GA routine is shown in Fig. 10.1.

As described in the previous section, the cost function determines the optimisation subject. For simplicity, we defined it as the difference between the desired outcome and the current outcome, as shown in (10.2). In the case of multibeam optimization, the fundamental cost function can be expressed as (10.3), where the E_{pk}s are the locations of the electric field peaks, and Es are the intended locations of the electric field peaks. So if the peaks are far away, then the square of the location difference will be large, whereas if the peaks are located as desired, then the square of the difference will be zero. With this general form of the cost function, we can also perform rudimentary SLL reductions.

$$cost = |E_1 - E_{pk1}|^k + |E_2 - E_{pk2}|^k + |E_3 - E_{pk3}|^k + ... \tag{10.3}$$

It is important to note that the cost function (also known as the fitness function) has the strongest and most direct impact on the effectiveness of the GA optimisation (or any optimisation), and we always prioritise the adjustment of the cost function over that of the GA operators. This method of optimisation is computationally costly, as can be seen from Fig.**??**, where convergence is reached after more than a hundred generations. Therefore, this approach is more suitable when used offline to generate a codebook, which can then be stored in the proposed device. We are working on a GS iterative method that can potentially be efficient enough to be deployed for online optimisations.

For the full cost function, one must add the individual weights for each cost for the GA to work optimally. The weights affect the prioritisation in optimisation, which is especially important for multi-objective optimisations. A generalised form for the complete cost function is expressed as follows:

$$C(Z) = \sum_{k}^{K} H(|Z_A| - |Z_B|) W_k \cdot (Z_A - Z_B)^{\eta} \tag{10.4}$$

where C is the cost function with input optimisation parameter Z; Z_A and Z_B can be either the desired and current value, or the current and desired value, depending on the type of parameters being optimised; $k = 0, 1, ..., K$ are the indices attached to the set of all current values; η is any natural number; H is the Heaviside step function that provides a sort of "stopping criterion"; W_k are the individual weights for each optimisation iteration. The cost function is set to be minimised towards zero.

For example, for a positive-valued parameter that is seeking optimisation values greater than the desired value (the magnitudes of the farfield electric field peaks, for instance), the cost function then becomes:

$$C(\phi_{mn}) = \sum_{k=1}^{K} H(|E_{dk}| - |E_k|)W_k \cdot (E_{dk} - E_k)^\eta \tag{10.5}$$

where ϕ_{mn} is the binary configuration matrix of the metasurface; E_{dk} is the desired electric field strength for the k^{th} electric field peak, E_k is the electric field strength of the k^{th} peak, given the input matrix ϕ_{mn}. If the current electric field peak strength is below the level desired, then a certain cost value will be assigned; if the current electric field peak strength is higher than the desired value, it will automatically be assigned a zero by the Heaviside step function.

In the case of a positive-valued parameter that is seeking optimisation values lower than the desired value (the location of the peaks, for instance), the cost function becomes:

$$C(\phi_{mn}) = \sum_{k=1}^{K} H(|E_k^{dp} - E_k^p| - R)W_k \cdot (|E^{dp} - E_k^p| - R)^\eta \tag{10.6}$$

where $|E_k^{dp}$ is the desired location of the k^{th} peak; E_k^p is the location of the k^{th} peak; R is the maximum acceptable radius/distance between the desired location and the current peak location. In this example, if the distance between the desired electric field peak location and current electric field peak location is greater than the acceptable distance R, then a cost value will be assigned; if the value is equal to, or less than R, then the cost will be zero.

The determination of the individual weights is the most time-consuming and challenging process, as often only trial and error or educated guesses methods are available. Through experience, we established a matured optimisation cost function weighting method with an improved convergence rate from adaptive crossover and mutation operations.

In fig. 10.2, we have the comparison between two GA evolutions: an adaptive GA with progression probability freedom and a non-adaptive GA with constant progression probabilities. The specific optimisation that is being performed is a four-beam, location-specific, phase-only pattern synthesis. The adaptive GA has a probability of mutation that is directly proportional to the rate of convergence. We can notice a roughly 20-generation advantage with the adaptive GA, although the relative advantage of the adaptive GA can vary depending on the starting population and the specific optimisation problem.

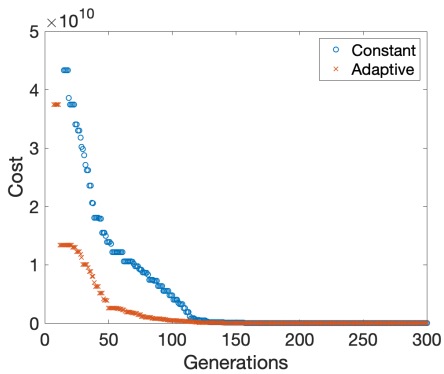

Figure 10.2: The 4-beam optimization convergence rates for the adaptive and non-adaptive GA algorithm. The adaptive GA converges (to an acceptable cost) roughly twenty generations faster, and the improvement is especially noticeable when an effective initial population is given.

10.2 Gerchberg-Saxton

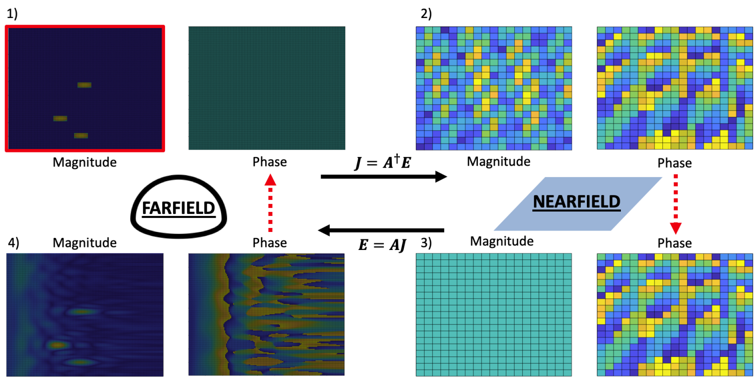

Figure 10.3: Illustration of the iterative processes of the GS algorithm.

In Fig. 10.3, we demonstrate the general steps through an iteration of the GS algorithm applied to reflectarray phase retrieval. With this algorithm, we intend to retrieve the phase profile of the nearfield (where the individual antenna elements lie on), given an intended farfield profile. In each step, we distinguish between the real (magnitude) and imaginary (phase) parts of the farfield/nearfield. In the first step, we generate the desired farfield electric field magnitude profile that we intend to achieve, and then associate that with a zero/constant phase profile. In the second step, we transform the farfield E into nearfield/surface current J via the integral relation, and in doing so, we arrive at a complex J that has both magnitude and phase terms. In the third step, we obtain the phase part of the nearfield J, which is what we intend to retrieve, and then reset the magnitude part of J to be zero. This is due to the fact that we know our reflectarray surface is a phase-only synthesis, meaning that only the phase is being manipulated to achieve the intended farfield profile, while the magnitude is being kept constant. In the fourth step, we transform the new nearfield J back into the farfield region, using the newly retrieved phase distribution. The final step is to retain only the phase term of the updated farfield and combine that with the intended farfield before another iteration of calculation begins.

10.2.1 Angle to Plane

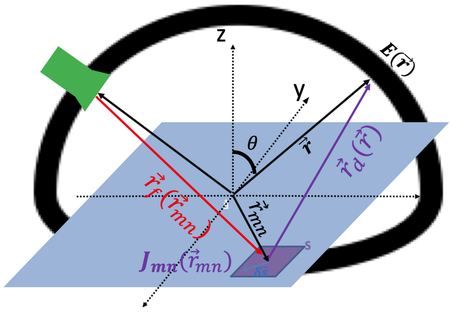

Figure 10.4: Vector formation of the farfield-nearfield transform pair.

$$\begin{aligned} E(\vec{r}) &= \sum_{m=1}^{20}\sum_{n=1}^{20}\int_S \frac{e^{-ik(\vec{r}_f)}e^{ik(\vec{r}-(\vec{r}_{mn}+\delta\vec{s}))}}{4\pi(\vec{r}-(\vec{r}_{mn}-\delta\vec{s})-\vec{r}_f)} J(\vec{r}_{mn})\,\delta\vec{s}\,\mathrm{d}(\delta\vec{s}) \\ J(\vec{r}_{mn}) &= \sum_{\theta=0}^{\pi/2}\sum_{\phi=0}^{2\pi}\int_S \frac{e^{ik(\vec{r}_f)}e^{-ik(\vec{r}-(\vec{r}_{mn}+\delta\vec{s}))}}{4\pi(\vec{r}-(\vec{r}_{mn}-\delta\vec{s})-\vec{r}_f)} E(\vec{r})\,\delta\vec{s}\,\mathrm{d}(\delta\vec{s}) \end{aligned} \tag{10.7}$$

Our vector formulation of the farfield-nearfield transform pair, described by eq. 10.7 and illustrated in fig. 10.4, is essentially derived from a Huygen-Fresnel integral, with the diffraction and image plane replaced by the farfield (E) and nearfield (J) in our case. We can see that the integral equation is essentially an element-by-element summation (the indices m, n represent the element row and column number) of the EM propagation in vector form. The EM propagation initiates from the feed source to the reflectarray surface element, with the propagation vector of $\vec{r}_f$, and then to the observation point, with vector $\vec{r}_d$. The vector $r_{\vec{mn}}$ describes the position of the mn^{th} element. The integral $\int_S$ covers the summation over the surface of the individual reflectarray element. The resulting farfield electric field is illustrated as the black circle around the coordinates; it is a circle in this case, but for many vector formulation applications, such as metasurface pattern synthesis of holograms, the observation field will be a flat plane.

To be precise, the farfield E is actually related to the surface current J, in our case. This is due to the integral relation between the antenna farfield and surface current: the radiation pattern, or farfield, is known as the Fourier transform of the surface current. It is important to note that the vector transform pair is calculating the farfield electric field strength at a precise point in the observational space. Hence, it is useful for applications such as holographic pattern synthesis, where the exact location of the field intensity in space is needed to be known. In our case, where we are attempting similar methods for antenna pattern synthesis, where we care not about the field intensity in a precise point in space, as the farfield approximation means we only need to ensure the direction of radiation (we will be optimising for $E(\theta, \phi)$, without r, or approximating r as infinity).

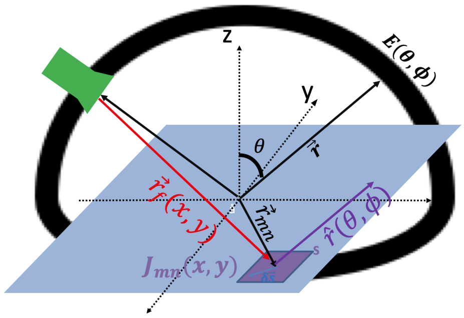

Figure 10.5: Scalar formation of the farfield-nearfield transform pair.

$$\begin{aligned} E(\theta, \phi) &= \sum_{m=1}^{20}\sum_{n=1}^{20}\int_S \frac{e^{-ik|\vec{r}_f|}e^{ik(\hat{r}\cdot(\vec{r}_{mn}+\delta\vec{s}))}}{4\pi(\hat{r}\cdot(\vec{r}_{mn}-\delta\vec{s})-|\vec{r}_f|)} J(x,y)\,\delta\vec{s}\,\mathrm{d}(\delta\vec{s}) \\ J(x,y) &= \sum_{\theta=0}^{\pi/2}\sum_{\phi=0}^{2\pi}\int_S \frac{e^{ik|\vec{r}_f|}e^{-ik(\hat{r}\cdot(\vec{r}_{mn}+\delta\vec{s}))}}{4\pi(\hat{r}\cdot(\vec{r}_{mn}-\delta\vec{s})-|\vec{r}_f|)} E(\theta,\phi)\,\delta\vec{s}\,\mathrm{d}(\delta\vec{s}) \end{aligned} \tag{10.8}$$

The scalar formulation, described by eq. 10.8 and illustrated in fig. 10.5, is what we will be employing in our application. This formulation is based on the premise that the observation point is infinitely far away, and the observation farfield electric field becomes $E(\theta, \phi)$, which is only angle-dependent. Resulting from the farfield approximation, the individual vectors from the array element to the observation point ($\vec{r}_d$ in fig. 10.4) will become parallel to the vector from the coordinate centre to the observation point ($\vec{r}$).

Now the observation point is infinitely far away, in order to describe the resulting phase difference arising from the path difference among difference array elements, we can simply analyse the phase shift due to a coordinate shift: by doing $\vec{r}_{mn} \cdot \hat{r}$, we arrive at this phase shift due to coordinate shift, along the observation direction. In layman's terms, if one would picture the observation direction or plane at infinity, the difference in the phases of EM propagations from each antenna element is due to the path difference, which results from the coordinate locations of the individual elements with respect to the feed source and observation direction: this difference, when concluded at the farfield plane, is simply resulting from the coordinate locations of the array elements. With the scalar transform pair, we now arrive at a much simpler expression, which allows us to work explicitly with directional electric field profiles, $E(\theta, \phi)$.

10.2.2 Scalar Equation

Upon expansion of the scalar transform pair (10.8), with simplification and neglecting the normalization constants, we arrive at the simplified scalar transform pair, as described in (10.9). This will be the transform pair that we will be using in the modified GS algorithm.

In (10.9), m, n represent the indices m^{th} and n^{th} antenna element on the reflectarray surface. i, j represent the indices of farfield space: our farfield is defined as $\theta = 0 \to \pi/2$ and $\phi = 0 \to 2\pi$ and i, j runs through each quantized spatial fraction within these domains. Our reflectarray is a phase-only model, meaning that the pattern synthesis can only be achieved through the manipulation of reflection phases, while reflection magnitudes are kept constant. This means that the nearfield transform $\boldsymbol{E_N} = e^{i \arg\left(\boldsymbol{E}_N\right)} = e^{i\boldsymbol{\Phi_{mn}}}$, where $\boldsymbol{\Phi_{mn}}$ is the phases on the $(m, n)^{th}$ unit antenna element. The surface integral $\int_S$ is embedded within the dimensional coordinates x and y. It is important to note that the variables of transform (ones that are dependent on i, j and x, y) are stored in matrices in a meshgrid format, through MATLAB: this helps to expedite what would otherwise be a quadruple summation.

$$
\begin{aligned}
&\boldsymbol{E_N}(m,n) = \sum_i^I \sum_j^J \boldsymbol{E_F}(i,j) \exp\Big[ik_0 r_f(m,n) \\
&- ik_0\Big(x(m,n)\cos\phi(i,j) + y(m,n)\sin\phi(i,j)\Big)\sin\theta(i,j)\Big] \\
&\boldsymbol{E_F}(i,j) = \sum_m^M \sum_n^N \exp\Big[i\boldsymbol{\Phi}_{m,n} - ik_0 r_f(m,n) + \\
&ik_0\Big(x(m,n)\cos\phi(i,j) + y(m,n)\sin\phi(i,j)\Big)\sin\theta(i,j)\Big]
\end{aligned}
\tag{10.9}
$$

10.2.3 Plane to Plane

In the case where we would be utilising the developed GA algorithm for plane-to-plane applications (for instance, holographic scenarios, or situations where the precise location of a farfield point is needed to be focused on), then we may also utilise a plane-to-plane transformation that can facilitate the transforms.

$$x = 0.5\sqrt{2 + u^2 - v^2 + 2u\sqrt{2}} - 0.5\sqrt{2 + u^2 - v^2 - 2u\sqrt{2}} \tag{10.10}$$
$$y = 0.5\sqrt{2 - u^2 + v^2 + 2v\sqrt{2}} - 0.5\sqrt{2 - u^2 + v^2 - 2v\sqrt{2}} \tag{10.11}$$

In equation-10.11, we have the mapping equations that will bring the farfields from the spherical frame to the flat Cartesian frame. This can be convenient for applications that are intended to be mapping two planes: for instance, if we are dealing with situations where we intend to project (with specific strengths) at precise locations on a plane.

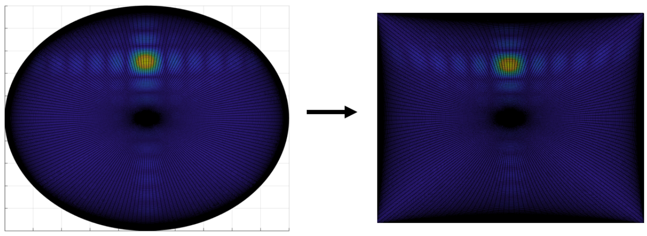

Figure 10.6: The beam-steering Farfield that is mapped into the planar form.

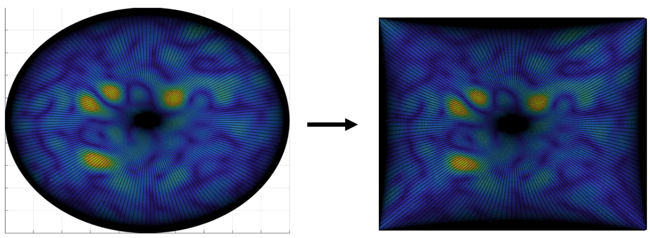

Figure 10.7: The multi-steering Farfield that is mapped into the planar form.

In fig. 10.6 and fig. 10.7, we illustrate the mapping between $\sin(\theta)\cos(\phi)$ in the x-axis and $\sin(\theta)\sin(\phi)$ in the y-axis, and θ in the x-axis and ϕ in the y-axis.

10.2.4 Results

In this section, we present the results of synthesized beam patterns. These beams are modelled to be reflecting off from a 20x20 (in Fig. 10.8 a), b), c), and d)), 60x60 (in Fig. 10.8 e)) and a 100x100 (in Fig. 10.8 f)) element LC-based reflectarray metasurface, with an omnidirectionally radiating feed source that is located at 10λ above the centre of the device. The specifics and theoretical modelling of the LC reflectarray metasurface can be found in our previous publication[51].

Firstly, there are three sets of variable-magnitude four-beam multibeam results, as presented in Fig. 10.8 a), b) and c). Here we demonstrate the ability to control not only the exact locations of the four beams, but also the magnitudes. In Fig. 10.8 a), we have a four-beam profile with equal magnitudes. In Fig. 10.8 b), we have a roughly two times stronger centre beam (at $\theta = 0°, \phi = 0°$). In Fig. 10.8 c), we have a roughly two times weaker centre beam. The four beams are located at $\theta = 0°, \phi = 0°$, $\theta = 25°, \phi = 45°$, $\theta = 15°, \phi = 180°$ and $\theta = 35°, \phi = 315°$. For these calculations, the GS took around five iterations (around twenty seconds of computation time) to arrive at the presented results.

In Fig. 10.8 e), we have increased the dimension of the device to achieve high multibeam counts while maintaining low beamwidths. Here we demonstrate a seven-beam profile that follows a vortex-like spatial progression, where the beam that extends the furthermost from the centre possesses the highest amplitude. This kind of pattern could be potentially applied to a scenario where a connection further away needs to be established with stronger signal gain (in order to overcome the high path-loss in THz waves), while the connections closer to the device may be maintained at a lower signal strength. For the seven-beam profile, the GS algorithm took around ten iterations (around one hundred seconds of computation time) to arrive at the presented result.

The circular beam profile, which is presented in Fig. 10.8 f), is a demonstration of the flexibility of the modified GS. Traditionally, if one were to synthesize more complex beam patterns with GA or PSO, an intricate cost function must be established. With the modified GS algorithm, we can simply "draw" the desired electric field profile and insert it as the initializing farfield amplitude matrix. For the circular beam profile, it took fifty iterations (around ten minutes of computation time due to the large number of reflectarray elements) to arrive at the presented result.

As a verification process, we performed a full-wave simulation with the phase configuration presented in Fig. 10.8 c). This result is presented in Fig. 10.8 d). For the full-wave simulation, since we have used a binary phase (either 0° or 180°) control surface[51], we have thus transformed the phase obtained into binary phases. Notice here that the mainlobe strengths are roughly 4 dBi weaker than that is shown in the analytical results, in Fig. 10.8

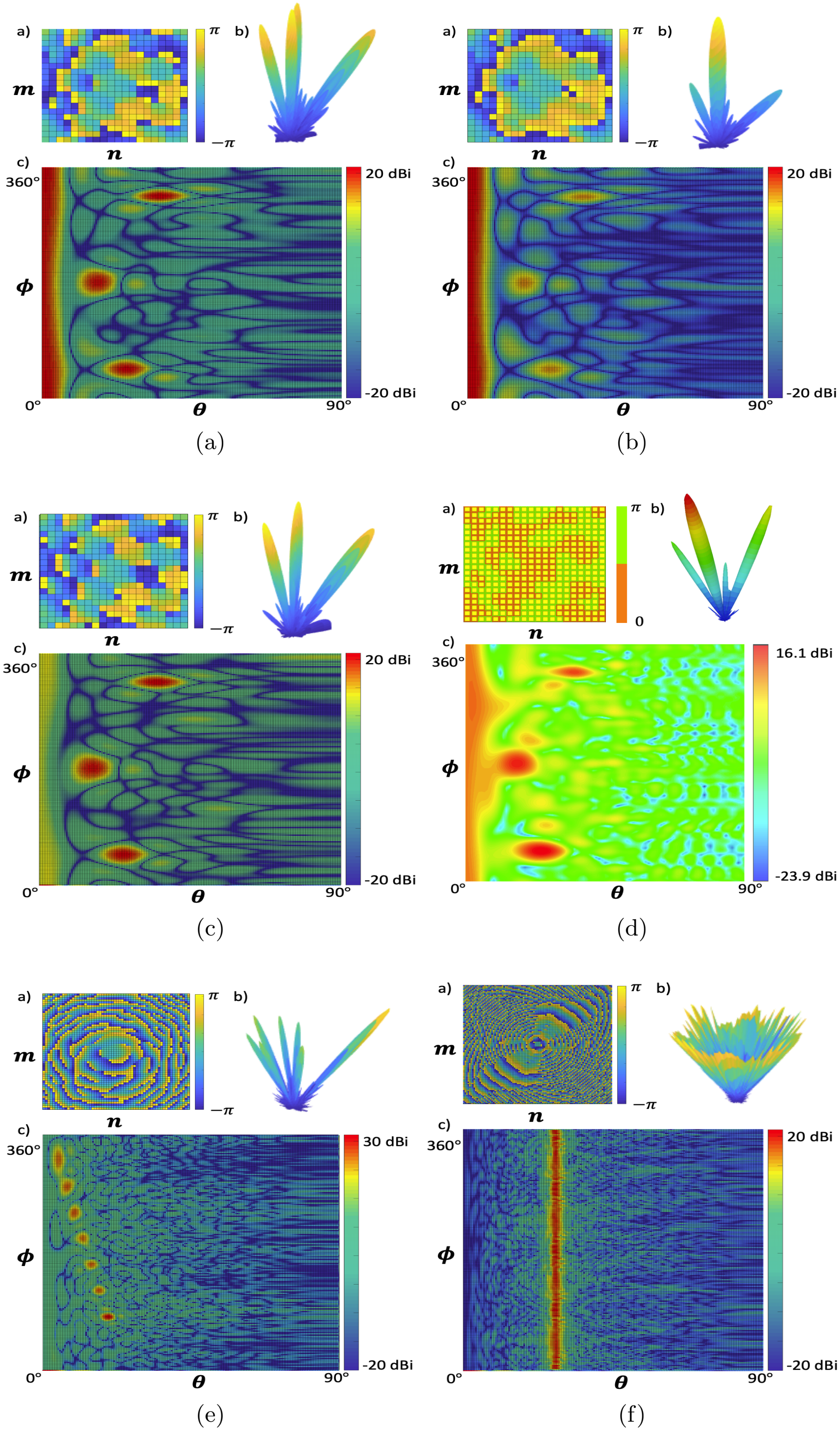

Figure 10.8: a) 20x20, four-beam profile, equal beam magnitudes, b) 20x20, four-beam strong mainlobe, c) 20x20, four-beam weak mainlobe, d) 20x20, four-beam weak mainlobe full-wave simulation e) 60x60 seven-beam vortex profile and f) 100x100, circular beam profile. The subfigures within each plot are the retrieved surface phase configuration, the 3D illustration of the normalized linear electric farfield, and the 2D decibel electric farfield.

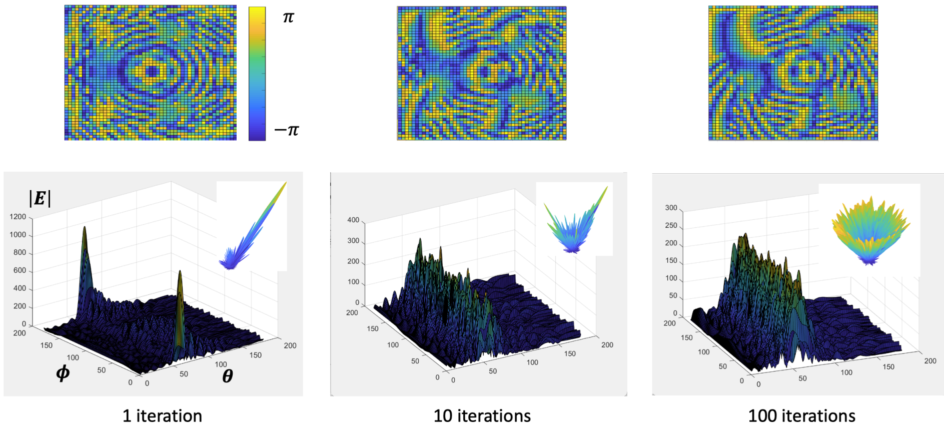

Figure 10.9: Spherical beam synthesis with GS iterative algorithm.

c). Two of the main contributing factors are: 1) quantization error, which results from the fact that we are lowering the "resolution" of each "pixel" from a continuous degree of phase variation ($0° - 360°$) to a binary degree of phase variation ($0°$ or $180°$), and 2), the full-wave simulation factors in material losses and intricate EM effects such as edge, surface and coupling effects.

In fig. 10.9, we show the pattern synthesis and phase retrieval process with a spherical beam pattern on a 100 x 100 element surface. In the top row sub-figures, we have the retrieved phase values, and in the bottom row sub-figures, we have the retrieved farfield that is formed with the corresponding surface phase profile. We see how the first iteration produced relatively poor results, but over 100 iterations, the spherical pattern became clear.

We must however, point out that, despite being a fast phase retrieval algorithm that allows us to quickly tackle array pattern synthesis, the modified GS algorithm has the drawback of tending to easily reach local minimums, and when such is the case, extending the search/optimization outside of the current region/path may be more restricted than traditional algorithms such as GA and PSO. Nonetheless, GS has shown great efficiencies in RIS pattern synthesis and thus, can always be used as a first-hand solution; if further fine-tuning optimizations are needed (such as side-lobe-level reduction), more suitable global optimizers can then be used, with the retrieved phases as input populations/swarms.

Chapter 11

All-Dielectric Metasurface

The traditional method of achieving polarisation conversion is by means of utilising birefringent materials. When an EM wave propagates in a birefringent material, the velocity of the different orthogonal components of the EM wave will be impeded differently by the different refractive indices of the birefringent material; this results in the phase difference between the two orthogonal components of the EM wave when it comes out from the birefringent material (as compared to before entering it). Through the designing of the birefringent material thickness, one can then precisely control the amount of phase shift that is acquired by the two orthogonal components, and then achieve the required polarisation.

For the THz regime, however, many traditional birefringent materials tend to have a rather high degree of absorption, which is especially significant given the thickness required to achieve phase shifts[12, 48]. Crystalline dielectrics[48], for instance, possess birefringent properties at the THz regime, but suffer from high absorption, narrow bandwidth, and significant reflection loss. More recent studies have demonstrated the feasibility of stacked crystalline devices, which improve the performance on operational bandwidth; however, the energy-efficiency, device thickness, as well as cost, are still not ideal.

Metasurfaces have been demonstrated to enforce an abrupt phase change at the surface; this means that if one could engineer the metasurface for specific polarisation conversion purposes, the thickness of the device can be greatly reduced (as compared to traditional propagation phase accumulation devices). The metal-based metasurface that utilises plasmonic resonances to achieve phase change tends to be less efficient at higher frequencies due to the ohmic losses, whereas dielectric resonators are free from this frequency restriction.

Another consideration is on the device type, which we will employ a reflection-based device, also known as a reflectarray metasurface. This is due to the higher efficiency and lower thickness level of reflection-type metasurfaces. The reduction of material thickness, coupled with a reflection-based metasurface (reflectarray metasurface) and the fundamental advantages of dielectric materials at THz regimes, can greatly improve the efficiency of polarisation conversion devices.

11.1 Polarisation Conversion

The principle ideas for the polarization-converting unit cell's design come from the resonance offset between two different frequencies and the electric field component's decomposition. In a circularly polarised light, the orthogonal components of the electric are offset by 90 degrees phase shift, whereas in a linearly polarised light, the electric field is confined to oscillate in one direction only. In order to convert a linearly polarised light into a circularly polarised light, one must be able to decompose linear polarisation into the two orthogonal components, while delaying/advancing the phase of one of the components by 90 degrees, depending on the chariality of the circular polarisation.

In order to achieve the decomposition/separation of electric field components from a linearly polarised light source, a unit cell consisting of two orthogonal arms is developed, as depicted in fig. 11.1 a). The principal axes of the cross-arm dielectric resonator are positioned at an angle of 45° to the polarisation direction of the incident light. In this way, the electric field of the linearly-polarised light will be exciting the resonator along the direction of its principal axes, which are orthogonal to each other.

In order to achieve a circular polarisation, further phase adjustments need to be performed: this is done through the design of the dielectric resonator's arms lengths. The length of the arms along the resonator's principal axes dictates the resonance frequency of the electric field polarised along that direction. When the incident frequency is invariant, the difference in the resonant frequency will give rise to a difference in the phase response of the two polarisations along the two principal axes.

Jones calculus would allow us to more easily understand what is needed to achieve the desired outcome. As we recall, the relation between the input and output electric field is $\mathbf{E^{out}} = \mathbf{JE^{in}}$, and the Jones vector can be decomposed into its eigenvectors and eigenvalues, and for unit cells with rotational symmetries, the above relation becomes:

$$\mathbf{E_{out}} = \mathbf{R}(\theta)\begin{bmatrix} R_x & 0 \\ 0 & R_y \end{bmatrix}\mathbf{R}(-\theta)\mathbf{E_{in}} \tag{11.1}$$

where $\mathbf{R}(-\theta) = \begin{bmatrix} \cos\theta & \sin\theta \\ -\sin\theta & \cos\theta \end{bmatrix}$ is the rotational matrix that rotates the resonator with respect to the reference axis, while $R_x = e^{i\phi_x}$ and $R_y = e^{i\phi_y}$ are the reflection coefficients for the two orthogonal components, which are resulted from the resonator's dimensions (long and short-axis lengths, as well as height) and assumed to be phase-only in this case. The rotation causes a complex operation which would result in either the change in the polarisation or the addition of a geometric phase. If we use a linearly polarised EM wave, then $\mathbf{E_{in}} = \begin{bmatrix} 1 \\ 1 \end{bmatrix}$, and the resulting electric field becomes:

$$\mathbf{E_{out}} = \begin{bmatrix} e^{i\phi_x}(\cos^2\theta - \sin\theta\cos\theta) + e^{i\phi_y}(\sin^2\theta + \sin\theta\cos\theta) \\ e^{i\phi_x}(\sin^2\theta - \sin\theta\cos\theta) + e^{i\phi_y}(\cos^2\theta + \sin\theta\cos\theta) \end{bmatrix} \tag{11.2}$$

for which we notice that if either the cosine or the sine becomes zero, e.g. $\theta = 0°$, then we are left with:

$$\mathbf{E_{out}} = \begin{bmatrix} e^{i\phi_x} \\ e^{i\phi_y} \end{bmatrix} \tag{11.3}$$

which is just the reflection phases resulting from the resonator structure. Thus, in order to have the output wave in circular polarisation, we must design the resonator such that $\phi_x = 0$ and $\phi_y = \pi/2$, so that $\mathbf{E_{out}} = \begin{bmatrix} 1 \\ i \end{bmatrix}$. Or having $\phi_x - \phi_y = \pi/2$. This is the reasoning behind the 45° rotation of the resonator. The reflection parameter and the making sure of the phase condition are then established by varying the resonator's physical dimensions.

The unit cell is designed in such a way that a 90 degrees phase delay is introduced to form a right-hand-circularly-polarised light, which is illustrated in fig. 11.1 d). In fig. 11.1 c) and d), we have the electric field's reflection amplitude and reflection phase. These results are retrieved through full-wave simulations, in CST Studio Suite, with the frequency solver, under periodic boundary conditions (repeating unit cells). The ground plane has the perfect-electric-conduction boundary condition. The incident EM wave is polarized along the y-axis. We can see that the reflected waves possess both amplitudes of x-polarised and y-polarised waves, which is an indication that the reflected wave can be circularly polarised. The circular polarisation is confirmed by further looking at fig. 11.1 d), where we see the reflection phase difference between the two polarisations are exactly 90 degrees at the operational spectrum of 2.9 THz to 3.25 THz. The reflection amplitudes of the two polarisations, shown in fig. 11.1 c), are roughly equal (less than 20% difference) in the designed operational range of 2.9 THz to 3.25 THz (outlined by the dashed line). This gives the device an 11.23% 3 dB bandwidth.

The polarisation conversion rate is defined here. First, we define the co-polarisation coefficient $R_{xx} = E_x/E_r$, and the cross-polarisation coefficient $R_{xy} = E_y/E_r$, where E_r is the reference electric field, and E_x, E_y are the x and y components of the reflected electric field. The polarisation conversion rate is defined as:

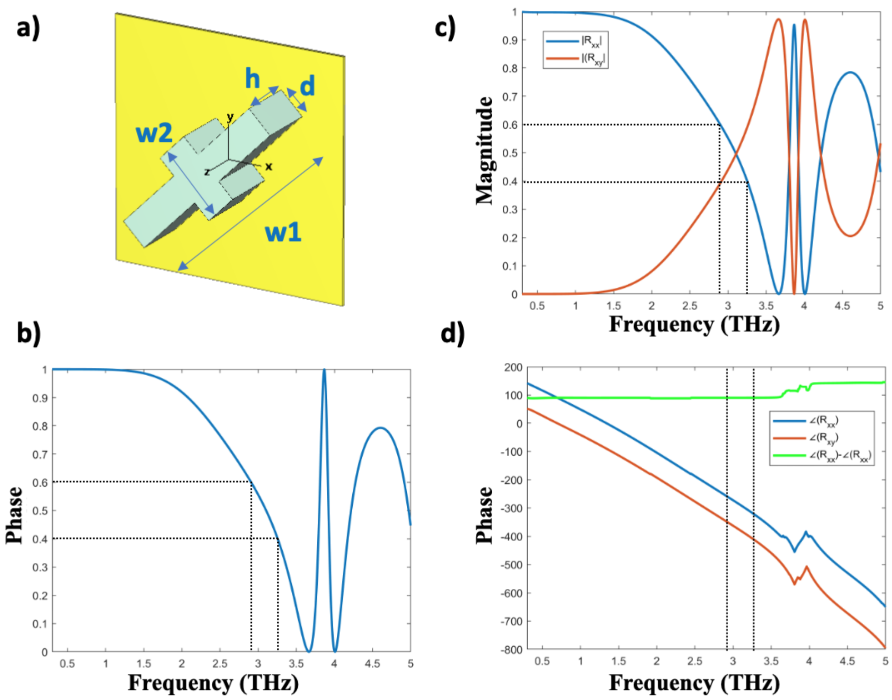

Figure 11.1: a) The unit cell schematics: $w1 = 32.79um$, $w2 = 12.66um$, $h = 28um$, $d = 5.81um$. The principal axes are along the major arms, in the direction of $w1$ and $w2$, whereas the polarisation of the incident light is along the direction of the y-axis. b) The polarisation conversion rate. c) and d), the reflection magnitude and reflection phase of the unit cell.

$$PCR = \frac{R_{xx}^2}{R_{xx}^2 + R_{xy}^2} \tag{11.4}$$

It is essentially a measure of the efficiency of polarisation conversion. When the reflection amplitudes of the electric field along the decomposed linear polarisations x and y are equal, the polarisation conversion rate is at the optimal value of 0.5. This is indicated by fig. 11.1 b), where we see the optimal PCR occurs in the operational frequency spectrum. In fact, the PCR is exactly 0.5 at 3.1153 THz, which is the optimal operational frequency.

In fig. 11.2, we are presented with the electric field vectors of the reflected light at an observation plane, which is roughly 5λ away from the device's surface. We can see that the electric field vectors are rotating clockwise, and at each quarter period segment, the vectors are pointing 90 degrees greater when compared to the last quarter segment, which indicates a good precision of the degree of phase separation. The magnitudes of the electric field vectors

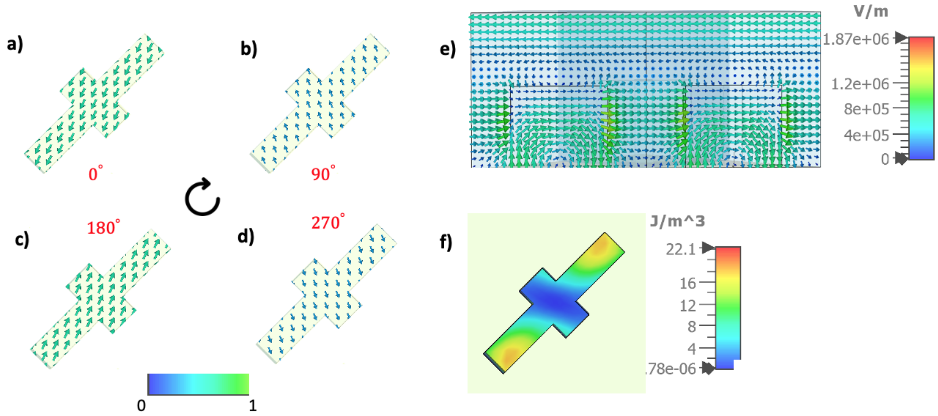

Figure 11.2: a)-d) The electric field vectors above the resonators, at four different phases: 0°, 90°, 180°, and 270°. e) The electric field vector within the dielectric resonators, excited at 3.1153 THz, with a y-polarised wave. f) The electric field energy density within the resonator under the same excitation source.

are not perfectly uniform along the revolution; this could have to do with the imperfections in the precision of the phase variation, and in the reflected magnitudes of the two different orthogonal electric field components. In fig. 11.2 e), we have the electric field vectors inside the dielectric resonators under full-wave simulation at 3.1153 THz. We can observe the circulating electric field looping within the resonator. This indicates the presence of a magnetic dipole, which is giving rise to the 90° phase difference for the orthogonal components of the reflected wave. In fig. 11.2 f), we have the electric field energy density plot, under a y-polarised plane wave incidence, which indicates the strongest field at the long principal axes of the resonator.

In fig. 11.3, we present the unit cell reflection phase and amplitude analysis for oblique incidence angles. For $\phi = 0°$, this is the case where the scanning in θ is along the y-axis; For $\phi = 90°$, this is the case where the scanning in θ is along the x-axis. We notice that the reflection amplitudes are almost identical for both extremes of the ϕ values. However, the amplitude difference between the two polarisations differs beyond acceptable levels at an incidence of $\theta > 55°$. The reflection phases show more complex phenomenons; for both ϕ values, the reflection phases differ beyond an acceptable level for values of $\theta > 35°$. However, the sign of the phase difference is the opposite, comparing the two values of ϕ, which means that the chirality is the opposite for these values. The information that we acquired from fig. 11.3 will have to be considered when designing the feed source, which, in a reflectarray set-up, is often at an angle to the device, in order to improve efficiency. The oblique incidence reflection phase and amplitude

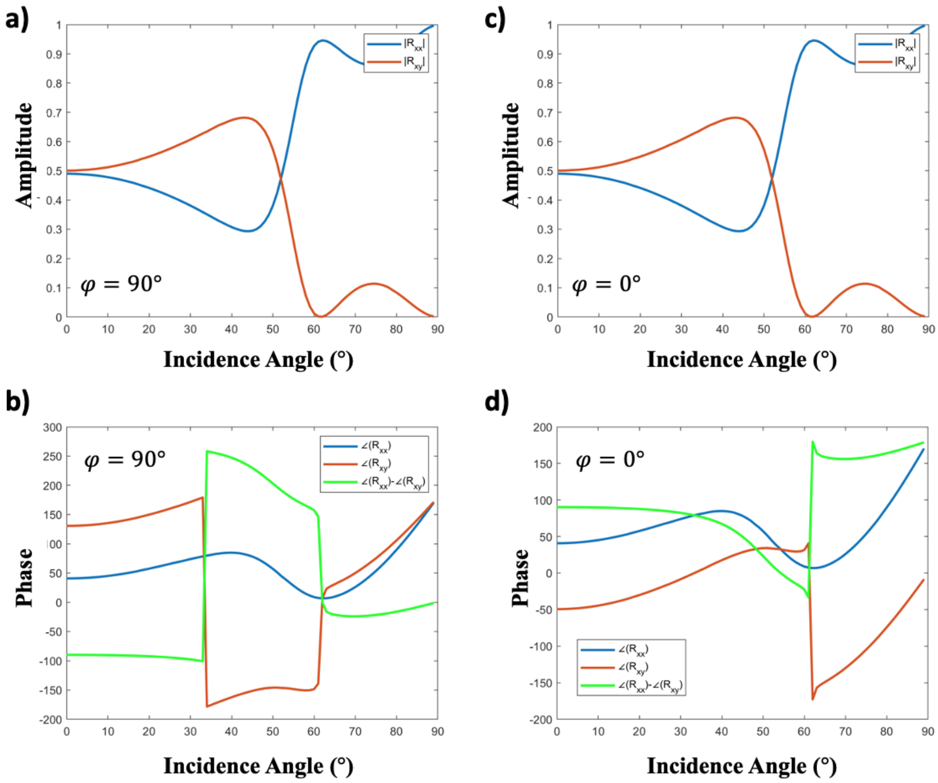

Figure 11.3: a) And b) the oblique incidence reflection amplitude and phase, for $\phi = 90°$, c) and d), similarly, but for $\phi = 0°$.

differences may also explain for the accuracies of the farfield beamsteering.

11.2 Reflectarray Metasurface

In order to design a reflectarray metasurface, one must be able to achieve the control of phase variations for a specific input frequency. For the frequency, we have chosen 3.1153 THz, as it offered the optimal PCR. For the phase response, we performed a parametric sweep of the height h of the dielectric resonators. This is chosen as it retains the axial ratio of the resonator's principal axes (the ratio of the two arms), which accounts for the precise phase difference between S_{xx} and S_{xy}. The height would therefore preserve the phase difference, while changing the overall resonant frequency that causes the response of the reflection phase from both orthogonal polarisation directions to vary equally. This effect is confirmed in fig. 11.4 d), where we see that the variation in resonator height changes the reflection phase of both R_{xx} and R_{xy}, while maintaining the difference between them to be $90°$. The phase response demonstrates a full $360°$ range of control.

Although the reflection phase under height variations has demonstrated over $360°$ of control, the reflection amplitude response, which is shown in fig. 11.4 c), shows that the device can only maintain roughly $180°$ of phase control, if the amplitudes of R_{xx} and R_{xy} were to be kept equal. This is further illustrated in fig. 11.4 e), which shows that the PCR is greater than 0.4 for resonator values of 18 um to 40 um, which corresponds to roughly a $180°$ reflection phase range. This has a few implications: it means that we could either set up the device with $180°$ of phase control, which maintains the equal reflection amplitudes of S_{xx} and S_{xy}, thus making a good quality polarisation converter, but lesser-quality reflectarray, due to the diminished quantization freedom; or we could sacrifice some quality in the polarisation conversion efficiency, while improving the reflectarray performance, by including the full $360°$ range of phase control. In our full device set-up, we have decided to use the latter option of having a full $360°$ range of phase control.

In fig. 11.4 a) and b), we show the reflection amplitude difference and the reflection phase difference between S_{xx} and S_{xy} as a 3-D surface plot, with varying parameters of frequency and resonator height. We observe that in the amplitude plot, the device is only stable (low amplitude difference) near the designed operating spectrum, near 3 THz. Prior to 3 THz, the device has not the capability to convert polarisation, as the magnitude difference nears 1. In the higher frequency regime, the amplitude difference variation is too frequent and too great, when the resonator height changes. For the reflection phase difference surface plot, we see that the phase difference is $90°$ everywhere in the operational spectrum and below; however, in the higher frequency regimes, the reflection phase difference differs significantly from $90°$.

With the resonator reflection phase and amplitude versus height relations established, we may proceed to design the appropriate reflectarray

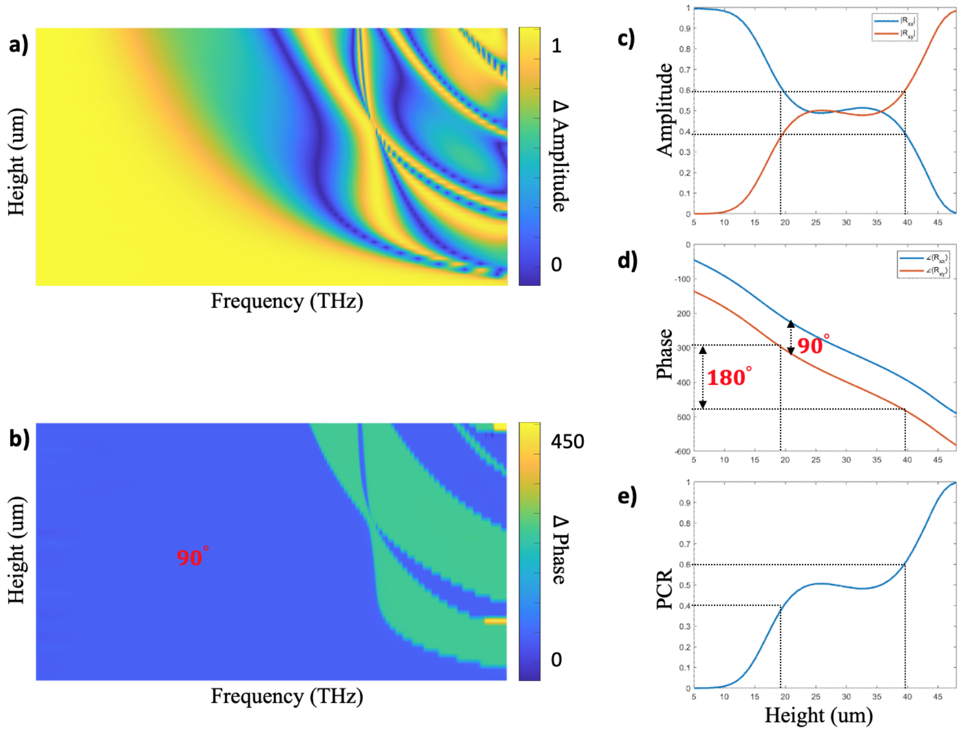

Figure 11.4: a) And b), the reflection amplitude difference and reflection phase difference between S_{xx} and S_{xy}, with varying frequency and resonator height. c), d) and e), the reflection amplitude, phase, and PCR at 3.1153 THz.

metasurface. To design the required phase shift for the surface, we make use of the array pattern theory:

$$\phi_R(x_i, y_i) = k_0(d_i - (x_i \cos\phi_s + y_i \sin\phi_s)\sin\theta_s) \tag{11.5}$$

where k_0 is the free space wave vector, d_i is the distance from the feed source to the ith antenna element, ϕ_s and θ_s are the angles of intended beam-steering.

In fig. 11.5 a), we show the full reflectarray metasurface with the resonator height adjusted to fit a reflection phase profile calculated by eq. 11.5. The intended beamsteering angle is at $\theta_s = 25°$ and $\phi_s = 45°$. The feed source is positioned 10 wavelengths above the device. In fig. 11.5 b), the reflection phase distribution is calculated by eq. 11.5 is presented. In fig. 11.5 c), we have the farfield electric field strength retrieved from CST's full-wave simulation. The farfield shows the mainlobe to be precisely positioned at the beamsteering angle of $\theta_s = 25°$ and $\phi_s = 45°$. However, the SLL is relatively high (around -3 dB), and there is significant specular reflection around the broadside direction. The high SLL can also be seen in fig. 11.5

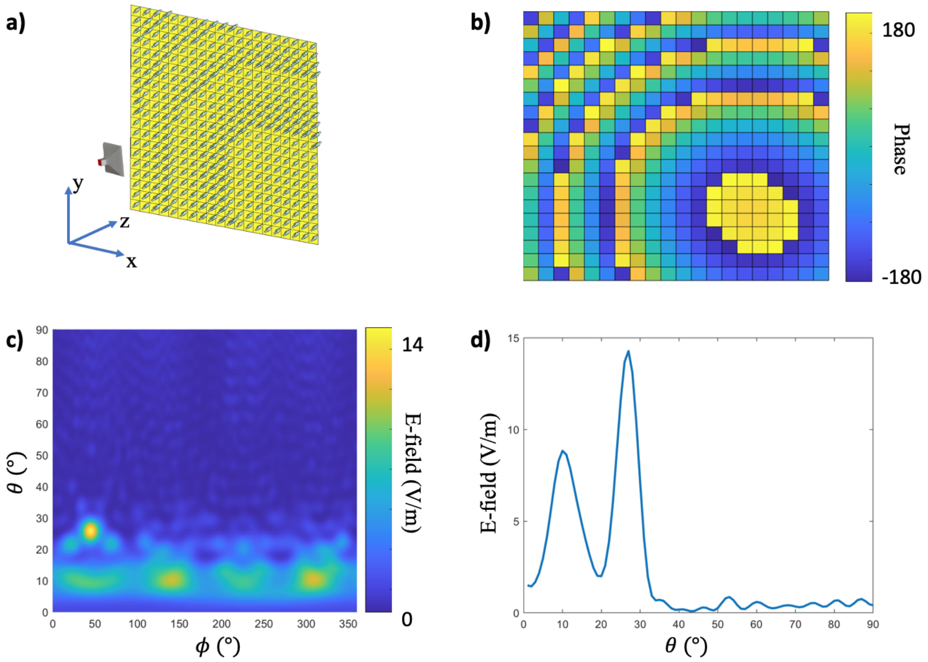

Figure 11.5: a) The full device, including the feed horn, is designed to be steering the beam towards $\theta_s = 25°$ and $\phi_s = 45°$. b) The phase profile calculated by eq. 11.5. c) The farfield electric field from full-wave simulation. d) The same farfield electric field plot, but chosen at a constant $\phi = 45°$ angle.

d), the scanning plot for $\phi = 45°$. We suspect that the specular reflection and the high SLL may be the results of the reflection amplitude difference exhibited at phase ranges over the 180° limit. Another possible factor could be the oblique incidence optical properties of the resonators; as the incident source is a point source near the device, the angle of incidence for elements around the edges may have significant values, such that the reflection properties (amplitude/phase) could be significantly different than the unit cell simulation suggested.

Chapter 12

Summary

In part-IV, there are four chapters: "LC Reconfigurable Reflectarray", "Scalability Analysis", "Phase Retrieval", and "All-Dielectric Metasurface".

In the first chapter on "LC reconfigurable reflectarray", there are four sections: "LC", "Problem Setup and Formulations", "Numerical Simulations", and "Super Cell Structure". The author presented the design and simulation of an LC-based 1-bit reconfigurable reflectarray that is operating at 108 GHz. The reflectarray utilises LC as a tunable substrate, which allows the control of reflected waves' phase, hence achieving reconfigurability. In "LC", the author introduced the principle ideas behind how LC is used in the reflectarray to achieve reconfigurability, as well as stating the simulation methods and parameters for LC. In "Problem Setup and Formulations", the author detailed the theoretical formulation for farfield calculations, as well as the semi-analytical approach that incorporates full-wave results. In "Numerical Simulations", the author presented the results retrieved from CST's full-wave simulations. In "Super cell Structure", the author showed the VBA scripting method that facilitates the model automation.

In the second chapter on "Scalability Analysis", the author presented the results of the effects on varied KPIs (HPBW, directivity, tangent deviation, and sidelobe level) from the variations of aperture size and phase quantisation degree. The author showed that, in general, a higher degree of phase quantisation freedom leads to better overall performances of the reflectarray, especially in terms of resolution/tangent deviation. The increase in aperture size leads to greater directivity values. However, the relation between other KPIs and the aperture size/phase quantisation freedom is non-linear and deserves one's consideration on the trade-offs in the design stage.

In the third chapter on "Phase Retrieval", the author presented, in two sections, two types of optimisation algorithms for reflectarray pattern synthesis and phase retrieval: GA and modified GS iterative algorithm. For the GA in section one, the author detailed the procedures for an adaptive GA and showcased its improvement in terms of convergence over the non-adaptive version. For the modified GS iterative algorithm in section two, the author detailed the entire development procedures that led us to the reflectarray-tailored phase-retrieval and pattern synthesis GS algorithm, which includes the introduction of a Fresnel-like transform integral and their modification into scalar forms. Exotic beam patterns and retrieved surface phase configurations are also shown in this section.

In the fourth chapter on "all-dielectric metasurface", the author presented a dielectric resonator-based metasurface that is designed to perform as a quarter-wave plate, delaying the orthogonal components of the electric fields and converting between spherical and linear polarisations. This design has the advantage of a much thinner profile when compared to traditional quartz-based quarter-wave plates. There are two sections in this chapter: "Polarisation Conversion" and "Reflectarray Metasurface". In "Polarisation Conversion", the principal mechanism of dielectric-based polarisation conversion, unit cell design, and unit cell's simulated optical properties are shown here. In "Reflectarray Metasurface", the full reflectarray structure's design procedures and reflection results are shown here.

Part V

Conclusion

12.1 Summary

In this thesis, there are three main chapters: 1) theoretical background, 2) a review of the state-of-the-art, and 3) research results.

In 1), a thorough overview of the theoretical background is given in order to support the understanding and analysis of metasurfaces presented in the following sections. Specifically, this chapter focuses on antenna and array theories, scattering theories, and optimisation algorithms.

In 2), a review of the state-of-the-art metasurfaces is conducted, with a focus on EM wave manipulation through surface phase change mechanisms, which antenna substrate resonance-based (LC), antenna metal resonance-based (diode), dielectric resonance-based (Mie resonance), plasmonic resonance-based (v-resonators), geometric resonance-based (circular polarisation dielectric resonators), and photosensitive-based (FZP).

In 3), the main work of the author is presented here, which can be split into two sections, 3)-a) where the primary focus and majority of contents have been dedicated to the work on LC-based reconfigurable reflectarray metasurface; 3)-b) phase-retrieval/optimisation algorithms applied to reflectarray pattern synthesis, and 3)-c), a side study of the dielectric-based polarisation converting reflectarray metasurface and preliminary results on reconfigurable graphene-based unit cell.

In 3)-a), an introduction to the LC, and its physical and electric properties are given, with specific simulation parameters noted in this section. Firstly, the unit cell design, which went through a first and a second stage improvement-development, is shown in detail, with the design formulae, optimisation routine/pseudo-codes, and unit cell optical characteristics. Secondly, the theoretical farfield model is constructed and presented. This includes the derivation for the surface phase distribution for specific beam-steering angle and input source location, and the implementation of a full-wave-derived nearfield model, which is incorporated into the analytical model. Thirdly, numerical simulation results on the farfield electric field are presented here. For the LC-based reflectarray, there are beamforming, beam-splitting, and multi-beam functionalities, which are presented in 2-D surface plots to precisely compare with the semi-analytical models. A table of KPI that contrasts the full-wave results with the semi-analytical values is presented here. Lastly, a detailed section on the scalability analysis is given. In this section, we explored the performance variations with varying device parameters; specifically, we analysed the KPIs' (SLL, mainlobe gain, HPBW, TD) changes when the device's degree of quantisation freedom, unit cell dimension, and aperture dimension varied.

In 3)-b), the phase-retrieval section, two topics are presented: GA-based optimisation and GS-based phase-retrieval. The GA is developed first, as a means of obtaining the device's surface phase distribution for a given non-trivial farfield beam pattern (multi-beam, for instance). Specifically, an adaptive version of the GA is utilised, and its performance is contrasted with the non-adaptive GA. The GA has been shown to be robust and effective at arriving at good global solutions. However, GA usually takes a long time (anywhere from four to ten hours) to converge to an acceptable level. The GS-based phase-retrieval is developed to tackle this challenge. The GS showed incredible performance improvements, at least on the level of arriving at local solutions. Although the GS algorithm that we developed is not capable of overcoming local valleys, so despite the fast convergence, solutions often remained local.

In 3)-c), the alternative metasurfaces section, we present a study on a dielectric-based reflectarray metasurface that is able to act as a reflection-based quarter wave-plate, converting the polarisation of reflected waves from linear to circular, or from circular to linear. The dielectric-based unit cell is then studied and optimised to achieve a non-reconfigurable reflection pattern, which aims to focus the reflected polarised beam in the direction of $\theta = 25°$ and $\phi = 45°$.

12.2 Future Works

Since the original idea for this PhD is to develop a PoC for the computationally studied reflectarray, this will remain to be the priority for possible future works. Preliminary simulation results have already been obtained for a down-scaled 28 GHz prototype reconfigurable LC-based binary reflectarray, and the following steps would lead to the fabrication procedures (circuit design, printing out PCB boards, enclosing the LC in micro-compartments, installing a control circuit for all the 20x20 elements, and finally testing the scanning pattern). The non-reconfigurable dielectric-based reflectarray is another good candidate to be fabricated for testing, as this does not require any electrical components (except for the feed source, of course).

In terms of the computational studies, there is much to follow up on: the GS optimisation has the tendency to be stuck at local minimas; the dielectric-based reflectarray has the limitation of 0-180 degrees phase control, as a result of the amplitude limitations extending beyond that phase range. Further work is needed to improve the global optimisation capabilities of the GS algorithm, and extend the phase control range and amplitude range of the dielectric resonators to achieve a full 360 degrees of control, which will offer optimal reflection performance. The LC-based reflectarray can be further designed to include amplitude control, either through a different unit cell design, or through an intrinsic physical design (pre-printed antenna patches with varying sizes). This will greatly improve the energy-efficiency by the reduction of spillover from the feed source; currently, the feed source has a wide 3 dB beamwidth. Some ideas on the introduction of a reconfigurable polarisation conversion to the LC-based device have also been formed, but not yet tested.

On the phase-retrieval and optimisation algorithms, there is also much space to explore: if global search capabilities can be enhanced in the GS algorithm, then it will be a great candidate to replace the GA completely since the convergence rate advantage is so great. Otherwise, some sort of combined GA-GS algorithm can be developed to achieve an optimal balance between the convergence rate and global solutions.

Bibliography

[1] S. A. A. Karim, H. Yadav. Design and simulation of lc based patch antenna at 20 ghz frequency. *AIP Conference Proceedings*, 2014.

[2] W. Aerts, P. Delmotte, and G. A. E. Vandenbosch. Conceptual study of analog baseband beam forming: Design and measurement of an eight-by-eight phased array. *IEEE Transactions on Antennas and Propagation*, 57(6):1667–1672, 2009.

[3] Arbabi, A., Horie, Y., Bagheri, and M. et al. Dielectric metasurfaces for complete control of phase and polarization with subwavelength spatial resolution and high transmission. *Nature Nanotechnology*, 10:937–943, 2105.

[4] A. Arbabi, Y. Horie, M. Bagheri, and A. Faraon. Dielectric metasurfaces for complete control of phase and polarization with subwavelength spatial resolution and high transmission. *Nature Nanotechnology*, 2015.

[5] C. A. Balanis. *Antenna Theory - Analysis and Design.* Wiley, 2005.

[6] P. J. Bevelacqua. http://antenna-theory.com.

[7] S. Bildik, S. Dieter, C. Fritzsch, M. Frei, C. Fischer, W. Menzel, and R. Jakoby. Reconfigurable liquid crystal reflectarray with extended tunable phase range. *Proc. of the 41st European Microwave Conference*, 2011.

[8] L. Burrows. Seas research named among discoveries of the year, 09 2017.

[9] T. Cameron. Bits to beams: Rf technology evolution for 5g milimeter wave radios. *Analog Devices*, 2018.

[10] Chen, K., Feng, Y., Yang, and Z. et al. Geometric phase coded metasurface: from polarization dependent directive electromagnetic wave scattering to diffusion-like scattering. *Sci. Rep.*, 6, 2016.

[11] W. T. Chen, A. Y. Zhu, V. Sanjeev, M. Khorasaninejad, Z. Shi, E. Lee, and F. Capasso. A broadband achromatic metalens for focusing and imaging in the visible. *Nature Nanotechnology*, 2018.

[12] Z. Chen, Y. Gong, H. Dong, T. Notake, and H. Minamide. Terahertz achromatic quarter wave plate: Design, fabrication, and characterization. *Opti. Commun.*, 311, 2013.

[13] A. Clemente, L. Dussopt, R. Sauleau, P. Potier, and P. Pouliguen. 1-bit reconfigurable unit cell based on pin diodes for transmit-array applications in x-band. *IEEE TRANSACTIONS ON ANTENNAS AND PROPAGATION*, 60(5), 2012.

[14] E. Collett. *Field Guide to Polarization.* SPIE, 2005.

[15] W. contributors. Gerchberg–saxton algorithm. Wikipedia, The Free Encyclopedia., 2021.

[16] W. contributors. Huygens–fresnel principle. Wikipedia, The Free Encyclopedia., 2022.

[17] W. contributors. Polarizing filter (photography). Wikipedia, The Free Encyclopedia., 2022.

[18] T. Cui, M. Qi, X. Wan, J. Zhao, and Q. Cheng. Coding metamaterials, digital metamaterials and programmable metamaterials. *Light: Science and Applications*, 3(218), 2014.

[19] R. Deng, F. Yang, S. Xu, and M. Li. A low-cost metal-only reflectarray using modified slot-type phoenix element with 360° phase coverage. *EEE Transactions on Antennas and Propagation*, 64(4):1556–1560, April 2016.

[20] R. Dickie, P. Baine, R. Cahill, E. Doumanis, G. Goussetis, S. Christie, N. Mitchell, V. Fusco, D. Linton, J. Encinar, R. Dudley, D. Hindley, M. Naftaly, M. Arrebola, and G. Toso. Electrical characterisation of liquid crystals at millimetre wavelengths using frequency selective surfaces. *Electronic Letters*, 2012.

[21] A. F. M. et al. Hybrid beamforming for massive mimo: A survey. *IEEE Communications Magazine*, 55(9):134–141, 2017.

[22] I. A. et al. A survey on hybrid beamforming techniques in 5g: Architecture and system model perspectives. *IEEE Communications Surveys and Tutorials*, 20(4), 2018.

[23] S. I. M. S. et al. Analog/digital ferrite phase shifter for phased array antennas. *IEEE Antennas and Wireless Propagation Letters*, 9:319–321, 2010.

[24] D. Ferreira, R. Caldeirinha, I. Cuinas, and T. Fernandes. Square loop and slot frequency selective surfaces study for equivalent circuit model optimization. *IEEE Trans Antennas Propagation*, 63(9):3947–3955, September 2015.

[25] R. W. Gerchberg and W. O. Saxton. A practical algorithm for the determination of phase from image and diffraction plane pictures. *OPTIK*, 35(2):237–246, 1972.

[26] S. Han, C. I, Z. Xu, and C. Rowell. Large-scale antenna systems with hybrid analog and digital beamforming for millimeter wave 5g. *IEEE Communications Magazine*, 53(1):186–194, 2015.

[27] J.-W. Hao, F. Wei, X.-B. Zhao, and X. W. Shi. Linear-to-circular polarization conversion based on all-dielectric 3d-printed metasurface for the application of broadband circularly polarized reflectarray antenna. *Journal of Physics D: Applied Physics*, 53, 2020.

[28] W. Hu, M. Ismail, R. Cahill, J. Encinar, V. Fusco, H. Gamble, R. Dickie, D. Linton, and N. G. S. Rea. Electronically reconfigurable monopulse reflectarray antenna with liquid crystal substrate. In *The Second European Conference on Antennas and Propagation, EuCAP*, pages 1–6, 2007.

[29] Y. Hu, X. Wang, X. Luo, X. Ou, L. Li, Y. Chen, P. Yang, S. Wang, and H. Duan. All-dielectric metasurfaces for polarization manipulation: principles and emerging applications. *Nanophotonics*, 9(12):3755–3780, 2020.

[30] C. Huang, B. Sun, W. Pan, J. Cui, X. Wu, and X. Luo. Dynamical beam manipulation based on 2-bit digitally-controlled coding metasurface. *Scientific Reports*, 7(42302), 2017.

[31] J. Huang and J. A. Encinar. *Antenna Analysis Techniques*. John Wiley and Sons, Inc., 2007.

[32] P. A. Huidobro, M. Kraft, R. Kun, S. A. Maier, and J. B. Pendry. Graphene, plasmons and transformation optics. *Journal of Optics*, 2016.

[33] R. Jakoby, A. Gaebler, and C. Weickhmann. Microwave liquid crystal enabling technology for electronically steerable antennas in satcom and 5g millimeter-wave systems. *Crystals*, 10(514), June 2020.

[34] J. A. E. John Huang. *Reflectarray Antennas*. Wiley-Interscience, 2007.

[35] Y. Jun, W. Pengjun, S. Shuangyuan, L. Ying, Y. Zhiping, and D. Guangsheng. A novel electronically controlled two-dimensional terahertz beam-scanning reflectarray antenna based on liquid crystals. *Frontiers in Physics*, 8, 2020.

[36] Y. Jun, W. Pengjun, S. Shuangyuan, L. Ying, Y. Zhiping, and D. Guangsheng. A novel electronically controlled two-dimensional terahertz beam-scanning reflectarray antenna based on liquid crystals. *Frontiers in Physics*, 8, 2020.

[37] M. Khorasaninejad, W. T. Chen, R. C. Devlin, J. Oh, A. Y. Zhu, , and F. Capasso. Metalenses at visible wavelengths: Diffraction-limited focusing and subwavelength resolution imaging. *Science*, 2016.

[38] R. Kraemer. Wireless 100 gb/s and beyond: Actual research approaches within a dfg special priority program (spp1655). In *IEEE*, 2017.

[39] K.-W. L. Kwai-Man Luk. *Dielectric Resonator Antennas*. Research Studies Press LTD., 2002.

[40] H. Legay, G. Caille, E. Girard, P. Pons, H. Aubert, E. Perret, P. Calmon, J. Polizzi, J.-P. Ghesquiers, D. Cadoret, and R. Gillard. Mems controlled linearly polarised reflectarray elements. In *2006 12th International Symposium on Antenna Technology and Applied Electromagnetics and Canadian Radio Sciences Conference*, 2006.

[41] X. Li, Z. Li, C. Wan, and S. Song. Design and analysis of terahertz transmitarray using 1-bit liquid crystal phase shifter. *IEEE Asia-Pacific Conference on Antennas and Propagation (APCAP)*, 2020.

[42] B. Liu and C. Song. High gain transmitarray antenna based on ultra-thin metasurface. *International Journal of RF and Microwave Computer-Aided Engineering*, 2019.

[43] Y. Liu, A. Zhang, Z. Xu, S. Xia, and H. Shi. Wideband and low-profile transmitarray antenna using transmissive metasurface. *Journal of Applied Physics*, 2019.

[44] Z. Ma, S. M. Hanham, P. Albella, B. Ng, H. T. Lu, Y. Gong, S. A. Maier, and M. Hong. Terahertz all-dielectric magnetic mirror metasurfaces. *ACS Photonics*, 2016.

[45] Z. Ma, Y. Li, Y. Li, Y. Gong, S. A. Maier, and M. Hong. All-dielectric planar chiral metasurface with gradient geometric phase. *Optics Express*, 2018.

[46] Maguid, E., Yulevich, I., Yannai, and M. et al. Multifunctional interleaved geometric-phase dielectric metasurfaces. *Light Sci Appl*, 6, 2017.

[47] F. F. Manzillo, M. Smierzchalski, J. Reverdy, and A. Clemente. A ka-band beam-steering transmitarray achieving dual-circular polarization. *European Conference on Antennas and Propagation, EuCAP*, 2021.

[48] J. B. Masson and G. Gallot. Terahertz achromatic quarter-wave plate. *Opt. Lett.*, 31, 2006.

[49] H. Maune, M. Jost, R. Reese, E. Polat, M. Nickel, and R. Jakoby. Microwave liquid crystal technology. *Crystals*, 8(355), September 2018.

[50] X. Meng, M. Nekovee, and D. Wu. Reconfigurable liquid crystal reflectarray metasurface for thz communications. In *Proceedings of the IET Antenna and Propagation Conference*, November 2020.

[51] X. Meng, M. Nekovee, and D. Wu. The design and analysis of electronically reconfigurable liquid crystal-based reflectarray metasurface for 6g beamforming, beamsteering, and beamsplitting. *IEEE Access*, 9:155564–155575, 2021.

[52] X. Meng, M. Nekovee, D. Wu, and R. Rudd. Electronically reconfigurable binary phase liquid crystal reflectarray metasurface at 108 ghz. In *2019 IEEE Globecom Workshops (GC Wkshps)*, pages 1–6, 2019.

[53] A. Moessinger, R. Marin, J. Freese, S. Mueller, A. Manabe, and R. Jakoby. Investigation on 77ghz tunable reflectarray unit cells with liquid crystal. *Pro. EuCAP*, 2006.

[54] S. Montori, E. Chiuppesi, P. Farinelli, L. Marcaccioli, R. V. Gatti, and R. Sorrentino. W-band beam-steerable mems-based reflectarray. *International Journal of Microwave and Wireless Technologies*, 3(5), 2011.

[55] J. P. B. Mueller, N. A. Rubin, R. C. Devlin, B. Groever, and F. Capasso. Metasurface polarization optics: Independent phase control of arbitrary orthogonal states of polarization. *Physical Review Letters*, 118, 2017.

[56] B. A. Munk. *Frequency Selective Surfaces: Theory and Design.* Wiley, Hoboken, NJ, USA, 2005.

[57] A. H. C. Neto, F. Guinea, N. M. R. Peres, K. S. Novoselov, and A. K. Geim. The electronic properties of graphene. *Review of Modern Physics*, 81, 2009.

[58] Ojaroudiparchin, M. Shen, and G. F. Pedersen. Design of vivaldi antenna array with end-fire beam steering function for 5g mobile terminals. In *In Proceedings of the 2015 23rd Telecommunications Forum Telfor (TELFOR)*, 2015.

[59] C. Pan, H. Ren, K. Wang, J. F. Kolb, M. Elkashlan, M. Chen, M. D. Renzo, Y. Hao, J. Wang, A. L. Swindlehurst, X. You, and L. Hanzo. Reconfigurable intelligent surfaces for 6g systems: Principles, applications, and research directions. *arXiv*, 2011.

[60] S. Payami, M. Ghoraishi, and M. Dianati. Hybrid beamforming for large antenna arrays with phase shifter selection. *IEEE Transactions on Wireless Communications*, 15(11):7258–7271, 2016.

[61] J. B. Pendry, A. Aubry, D. R. Smith, and S. A. Maier. Transformation optics and subwavelength control of light. *Science*, 337, 2012.

[62] G. Perez-Palomino, P. Baine, R. Dickie, M. Bain, J. A. Encinar, R. Cahill, MarianoBarba, and G. Toso. Design and experimental validation of liquid crystal-based reconfigurable reflectarray elements with improved bandwidth in f-band. *IEEE Transactions on Antennas and Propagation*, 61(4), 2013.

[63] G. Perez-Palomino, M. Barba, J. Encinar, R. Cahill, R. Dickie, and P. Baine. Liquid crystal based beam scanning reflectarrays and their potential in satcom antennas. *Proc. of EuCAP 2017*, 2017.

[64] G. Perez-Palomino, M. Barba, J. A. Encinar, R. Cahill, R. Dickie, P. Baine, and M. Bain. Design and demonstration of an electronically scanned reflectarray antenna at 100 ghz using multiresonant cells based on liquid crystals. *IEEE TRANSACTIONS ON ANTENNAS AND PROPAGATION*, 63(8):3722–3727, August 2015.

[65] G. Perez-Palomino, R. Florencio, J. A. Encinar, MarianoBarba, R. Dickie, R. Cahill, P. Baine, M. Bain, and R. R. Boix. Accurate and efficient modeling to calculate the voltage dependence of liquid crystal-based reflectarray cells. *IEEE TRANSACTIONS ON ANTENNAS AND PROPAGATION*, 62(5), 2014.

[66] PouriaYaghmaee. *Reconfigurable Tunable Microwave Devices Using Liquid Crystal*. PhD thesis, Babol Noshirvani University of Technology, 2011.

[67] J. R. Reis, R. F. S. Caldeirinha, A. Hammoudeh, and N. Copner. Electronically reconfigurable fss-inspired transmitarray for 2-d beamsteering. *IEEE TRANSACTIONS ON ANTENNAS AND PROPAGATION*, 65(9):4880–4885, September 2017.

[68] F. Shu, G. Yang, and Y. C. Liang. Reconfigurable intelligent surface enhanced symbiotic radio over multicasting signals. In *2021 IEEE 93rd Vehicular Technology Conference (VTC2021-Spring)*, 2021.

[69] C. Song, L. Pan, Y. Jiao, and J. Jia. A high-performance transmitarray antenna with thin metasurface for 5g communication based on pso (particle swarm optimization). *Sensors*, 2020.

[70] H. Steyskal. Digital beamforming. In *1988 18th European Microwave Conference*, 1988.

[71] E. G. Strinati, G. C. Alexandropoulos, V. Sciancalepore, M. d. Renzo, H. Wymeersch, D. T. Phan-huy, M. Crozzoli, R. D'Errico, E. D. Carvalho, P. Popovski, P. D. Lorenzo, L. Bastianelli, M. Belouar, J. E. Mascolo, G. Gradoni, S. Phang, G. Lerosey, and B. Denis. Wireless environment as a service enabled by reconfigurable intelligent surfaces: The rise-6g perspective. *arXiv*, 2021.

[72] F. T. Ulaby. *Fundamentals of Applied Electromagnetics.* Pearson Prentice Hall, 2006.

[73] S. University. 1g-2g-5g-the-evolution-of-the-gs. https://mse238blog.stanford.edu/.

[74] J. C. Vardaxoglou. *Frequency Selective Surfaces: Analysis and Design.* Research Studies Press, 1997.

[75] X. Wan, M. Q. Qi, T. Y. Chen, and T. J. Cui. Field-programmable beam reconfiguring based on digitally controlled coding metasurface. *Nature*, 6(20663), 2016.

[76] M. Wang, K. Shan, W. Luo, and Z. Chen. Design of a 2-bit dual linearly polarized reconfigurable reflectarray element. *IEEE International Symposium on Antennas and Propagation*, 2021.

[77] S. Wang, Z.-L. Deng, Y. Wang, Q. Zhou, X. Wang, Y. Cao, B.-O. Guan, S. Xiao, and X. Li. Arbitrary polarization conversion dichroism metasurfaces for all-in-one full poincare sphere polarizers. *Light: Science and Applications*, 2021.

[78] M. N. Xiaomin Meng, Rupert Young. Modified gerchberg-saxton iterative algorithm for reflectarray metasurface multibeam pattern synthesis. In *VTC2022-Spring*, 2022.

[79] P. Yagmaee, W. Withayachumnajul, A. K. Horestani, and A. Ebrahimi. Tunable electric-lc resonators using liquid crystal. *IEEE*, 2013.

[80] H. Yang, X. Cao, F. Yang, J. Gao, S. Xu, M. Li, X. Chen, Y. Zhao, Y. Zheng, and S. Li. A programmable metasurface with dynamic polarization, scattering and focusing control. *Nature*, 2016.

[81] R. L. e. a. YC. Liang, J. Chen. Reconfigurable intelligent surfaces for smart wireless environments: channel estimation, system design and applications in 6g networks. *Sci. China Inf. Sci.*, 2021.

[82] M. Younis, C. Fischer, and W. Wiesbeck. Digital beamforming in sar systems. *IEEE Transactions on Geoscience and Remote Sensing*, 41(7):1735–1739, 2003.

[83] N. Yu, P. Genevet, M. A. Kats, F. Aieta, J.-P. Tetienne, F. Capasso, and Z. Geburro. Light propagation with phase discontinuities: Generalized laws of reflection and refraction. *Science*, 2011.

[84] Y. Yusuf and X. Gong. A low-cost patch antenna phased array with analog beam steering using mutual coupling and reactive loading. *IEEE Antennas and Wireless Propagation Letters*, 7:81–84, 2008.

[85] A. Zaidi, N. A. Rubin, A. H. Dorrah, J.-S. Park, and F. Capasso. Generalized polarization transformations with metasurfaces. *Optics Express*, 29(24), 2021.

[86] G. Zhou, C. Pan, H. Ren, P. Popovski, and A. L. Swindlehurst. Channel estimation for ris-aided multiuser millimeter-wave systems. *arXiv*, 2016.

[87] S.-G. Zhou, G. Zhao, H. Xu, C.-W. Luo, J.-Q. Sun, G.-T. Chen, and Y.-C. Jiao. A wideband 1-bit reconfigurable reflectarray antenna at ku-band. *IEEE Antennas and Wireless Propagation Letters*, 21(3), March 2022.